3D Turning Analysis Of A Bipedal Robot

Dean Dionne Pretorius

Thesis presented in partial fulfilment of the requirements for the degree of Master of Engineering (Electronic) in the Faculty of Engineering at Stellenbosch University.

Supervisor: Dr Callen Fisher
Department of Electrical and Electronic Engineering

April 2022

Stellenbosch University https://scholar.sun.ac.za

Acknowledgements

The success of this project would not have been achieved without the guidance of Dr. Callen Fisher. Watching you grow and being forced to grow with you inspires me to try my best. Working with you has been special, and I am eternally grateful for how you inspired my future. If it wasn't for your guidance, I would have probably forgotten about this thesis while chasing penguins on Marion Island.

All my friends within the ESL. We were really well cast in our roles in the Big Bang Theory of the ESL. Even through a pandemic and working from home we managed to network, grow, and share memes with each other. I will always appreciate and take pride in the safe space we created for all of us to comfortably express our nerd.

The bedrock of my support network has always been my family. Thanks to Ivan, Lynne, Chesna and Byron Pretorius for all the love, food, and care I needed while doing this project. You kept my heart warm, and my tummy full on this journey. I love you!

Markus Van Der Westhuizen. Jy is werklik my broer, en ons is omtrent tuis met mekaar. Its inspiring that you were so influential in this journey even after spending half of it on the other side of the world. It has been a pleasure growing and learning with you!

Many thanks go to the CSIR (Center for Scientific and Industrial Research) for funding my academic career. You held my hand and supported me through my undergraduate, and postgraduate journey. I am excited to do my part and continue my life with you.

Stella and Jacques. . . We have walked a 6 year journey together. After all this time, its scary to think that our clique will be separating. But I smile at the prospects of our future. I accept the challenge of not making that Bohos beer our last.

Ilze Van Den Berg, Rome In A Bite, Ute Hermanus, Gideon Stephan and all the other anecdotes. Thanks for contributing to my journey in your own special ways.

This journey went through lots of ups, some downs. It succeeded through a pandemic, lockdowns, without electricity, failed startups, full-time internships, all-round construction, and the emotional Bitcoin market. Through it all, the Stellenbosch community supported my growth, and nurtured my confidence. It really does take a village to raise a child.

Stellenbosch University https://scholar.sun.ac.za

UNIVERSITEIT•STELLENBOSCH•UNIVERSITY
jou kennisvennoot • your knowledge partner

Plagiaatverklaring / *Plagiarism Declaration*

1. Plagiaat is die oorneem en gebruik van die idees, materiaal en ander intellektuele eiendom van ander persone asof dit jou eie werk is.
   Plagiarism is the use of ideas, material and other intellectual property of another's work and to present is as my own.

2. Ek erken dat die pleeg van plagiaat 'n strafbare oortreding is aangesien dit 'n vorm van diefstal is.
   I agree that plagiarism is a punishable offence because it constitutes theft.

3. Ek verstaan ook dat direkte vertalings plagiaat is.
   I also understand that direct translations are plagiarism.

4. Dienooreenkomstig is alle aanhalings en bydraes vanuit enige bron (ingesluit die internet) volledig verwys (erken). Ek erken dat die woordelikse aanhaal van teks sonder aanhalingstekens (selfs al word die bron volledig erken) plagiaat is.
   Accordingly all quotations and contributions from any source whatsoever (including the internet) have been cited fully. I understand that the reproduction of text without quotation marks (even when the source is cited) is plagiarism

5. Ek verklaar dat die werk in hierdie skryfstuk vervat, behalwe waar anders aangedui, my eie oorspronklike werk is en dat ek dit nie vantevore in die geheel of gedeeltelik ingehandig het vir bepunting in hierdie module/werkstuk of 'n ander module/werkstuk nie.
   I declare that the work contained in this assignment, except where otherwise stated, is my original work and that I have not previously (in its entirety or in part) submitted it for grading in this module/assignment or another module/assignment.

Copyright © 2022 Stellenbosch University
All rights reserved

Stellenbosch University https://scholar.sun.ac.za

Abstract

English

There is stark contrast between the abilities of legged locomotion found in nature, and locomotion found in lab environments. This performance gap is indicative of a large knowledge gap. Roboticists are required to bridge these gaps to truly invite robots to detach from their support rigs, and actuate within the real world. In this thesis, non-planar contact and discontinuous locomotive dynamics were modeled as a trajectory optimization problem. Consequently, this made understanding the complexities of legged locomotion more tractable.

Understanding, and being able to leverage, contact is crucial to successful legged locomotion. Therefore, a comprehensive investigation was conducted into non-planar contact dynamics using a monopod robot. Here, methods of modeling the Coulomb friction cone in contact implicit trajectory optimization were implemented. Literature suggests replacing the friction cone with a polyhedral approximation thereof. However, this method is known to underestimate the resultant friction in non-planar environments. This thesis presents a novel method of modeling the 3D friction cone and compares it to an implementation of the polyhedral approximation. Results from this comparison show that the novel method was significantly more computationally efficient than the polyhedral approximation, without underestimating the friction cone.

Dynamic bipedal locomotion remains a struggle for most robotic platforms. Robotics literature provides few examples of robots achieving agile, dynamic locomotion. Therefore, trajectories realizing non-planar dynamic bipedal motion were generated. Experiments were conducted into acceleration, steady-state, deceleration, and rapid turning off the sagittal plane. Optimal trajectories displayed the robot walking at speeds resulting in a Froude number less than 0.5, and running at speeds resulting in a higher Froude number. This is consistent with dynamic gaits found in nature. A sliding-mass velocity profile emerged when conducting long-time-horizon trajectories where the robot accelerated from a rest position and decelerated back to rest after completing multiple steps in a periodic steady-state gait. Additionally, when turning off the sagittal plane, slip occurred at least 93.32% of the duration of contact, and turn overshoot is present in all turn trajectories.

Stellenbosch University https://scholar.sun.ac.za

Afrikaans

Daar is skerp kontras tussen die vermoëns van voortbeweging wat in die natuur voorkom, en diè wat in laboratoriumomgewings voorkom. Hierdie prestasiegaping is aanduidend van 'n groot kennisgaping. Robotiste is verwag om hierdie gapings te oorbrug om robotte uit van hul ondersteuningplatforms uit te kom en in die werklike wêreld te aandryf. In hierdie tesis word 3D kontak en diskontinue lokomotiefdinamika gemodelleer as 'n trajekoptimeringsprobleem. Gevolglik maak dit die verstandhouding van robotik gebeendebeweging makliker.

Die verstaan van kontak, en hoe om dit te gebruik, is noodsaaklik vir suksesvolle voortbeweging. Daarom is 'n omvattende ondersoek uitgevoer, met behulp van 'n monopodrobot, om kontakdinamika beter te verstaan. Hier word metodes van modellering van die Coulomb wrywings-keel in kontak-implisiete-trajek-optimering geïmplementeer. Literatuur stel voor dat die wrywingskegel vervang word met 'n veelvlakkige benadering daarvan. Dit is bekend dat hierdie metode die gevolglike wrywing in 3D omgewings onderskat. Hierdie tesis bied 'n nuwe metode om die 3D-wrywingskegel te modelleer, en vergelyk dit met 'n implementering van die veelvlakkige benadering daarvan. Uitslae van hierdie vergelyking toon dat die nuwe metode meer berekeningsdoeltreffend was as die veelvlakkige benadering, sonder om die wrywingskegel te onderskat.

Dinamiese tweevoetige voortbeweging bly 'n stryd vir die meeste robotplatforms. Robotikaliteratuur verskaf min voorbeelde van robotte wat dinamiese voortbeweging bereik. Daarom is trajekte gegenereer wat 3D dinamika van tweevoetbeweging realiseer. Eksperimente word uitgevoer na accelerasie, bestendige toestand, verlangsaming en draaie van die sagittale vlak af. Optimale trajekte het die robot laat stap teen 'n spoed wat 'n Froude-getal minder as 0.5 laat kom, en hardloop teen spoed wat 'n hoër Froude-getal gehad het. Dit stem ooreens met dinamiese voetvalpatrone wat in die natuur voorkom. 'n Glymassa-spoedprofiel het voor gekom toe die lang-tyd-horison trajekte uitgevoer word: waar die robot van 'n rusposisie versnel het en terug versnel is na rus nadat hy verskeie stappe in periodieke bestendige-toestand voltooi het. Wanneer die robot van die sagittale vlak afdraai, gly hy ten minste 93.32% van die tyd wat kontak plaasgevind, en beurtoorskiet is teenwoordig in alle draaie.

Stellenbosch University https://scholar.sun.ac.za

Contents

Declaration ii

Abstract iii

List of Figures ix

List of Tables xiii

Nomenclature xiv

1. Introduction 1

1.1. Motivation Of Study 2

1.2. Problem Statement 3

1.3. Objectives Of The Research 3

1.4. Scope And Limitations Of Research 3

1.5. Structure Of Thesis 4

1.6. Publications 6

2. Literature Review And Theory Development 7

2.1. Dynamic Locomotion In Nature 8

2.1.1. How Many Legs Are Best? 8

2.1.2. Gait Selection: What To Do With My Feet? 10

2.1.3. Implementations At Speed 12

Stellenbosch University https://scholar.sun.ac.za

2.1.4. Maneuverability: How To Achieve Speed, And What To Do At Speed? 13

2.2. Traction And Slip Modeling 18

2.3. Trajectory Optimization 20

2.3.1. Objective Function 20

2.3.2. Formulating The Problem - Direct Methods 21

2.3.3. Contact Implicit Optimization 21

3. Methodology **25**

3.1. Dynamics 26

3.1.1. 3D Dynamics 27

3.1.2. Kinetic And Potential Energy 29

3.1.3. Lagrange Dynamics - Manipulator Equation 30

3.2. Trajectory Optimization 32

3.2.1. Long-Time-Horizon Optimizations 32

3.2.2. Collocation And Discretization 33

3.2.3. Cost Function 35

3.2.4. Initial And Final Conditions 35

3.2.5. Constraints 36

3.2.6. Solver Setup 40

3.2.7. Bounds 41

3.2.8. Variable Initialization 42

3.2.9. Decision Variables 42

4. Methods Of Modeling 3D Friction Using MPCCs **44**

4.1. Methods Of Modeling Friction 45

Stellenbosch University https://scholar.sun.ac.za

4.1.1. Polyhedral Approximation Of The Friction Cone 46
4.1.2. Novel Method Of Modeling 3D Friction Cone 47
4.2. Experiments 49
4.3. Results 51
4.3.1. Computational Complexity 51
4.3.2. Optimal Results 51
4.3.3. Epsilon Reduction Analysis 53
4.4. Discussion 55

5. Realizing Dynamic Bipedal Motion **56**
5.1. Bipedal Motion 57
5.1.1. Steady-State Motion 57
5.1.2. Acceleration And Deceleration 60
5.2. Results 61
5.2.1. Steady-State Results 61
5.2.2. Acceleration And Deceleration 65
5.3. Discussion 65

6. Bipedal Turning: To Slip Or Not To Slip? **68**
6.1. Turning 68
6.2. Experiments 70
6.3. Results 72
6.3.1. Turning At Varying Speeds 72
6.3.2. Turning At Varying Degrees 74
6.3.3. Turning The Other Direction 75

Stellenbosch University https://scholar.sun.ac.za

6.4. Discussion 75

7. Summary, Conclusion and Future Work **78**

7.1. Summary and Conclusion 78

7.2. Future Work 81

Bibliography **82**

Stellenbosch University https://scholar.sun.ac.za

List of Figures

1.1. This figure provides an overview of the research methodology used in this thesis. 1

1.2. This image displays the structure of the thesis. 5

2.1. This image displays new-born zebra locomotion, and robotic locomotion of the Atlas robot. 8

2.2. This image displays the differences between the human run and walk gaits. 11

2.3. This image displays the fasted implementation of robotic bipedal and quadrupedal locomotion. 13

2.4. This image displays the affect that transient motions have on forward velocity compared to steady-state. 14

2.5. This image displays the rapid deceleration of a cheetah, greyhound dog, and horse. 15

2.6. This image displays a cheetah conducting a rapid turn. 17

2.7. This image displays top-down views of the isotropic, and an-isotropic, friction cones. 19

3.1. This image displays both 3D robots used in this investigation. Two robots were modeled: a monopedal robot, and a bipedal robot with splayed hips. . 25

3.2. This image provides a graphic representation of how the generalized coordinates described the robots in this thesis. Absolute angles were used to describe the orientation of each link. 27

3.3. This figure displays how the long-time-horizon trajectory was split into multiple smaller trajectories, and then stitched together. 33

Stellenbosch University https://scholar.sun.ac.za

3.4. This image shows the rest position of the bipedal robot. All links were vertically stacked, and at rest. 36

3.5. This image displays the difference between directly solving the MPCCs, compared to relaxing them using ϵ-relaxation schemes. 37

3.6. This image displays how the inelasstic hard contact MPCC works. On the left, where the robot has not made contact with the surface, the MPCC is satisfied by setting $\lambda_z = 0$. When contact is made, as seen on the right, the MPCC is satisfied by setting $\rho = 0$. 39

3.7. Flow diagram of the iterative process used to find feasible solutions to the trajectory optimization. ϵ-relaxation schemes resulted in the 8 iterative solve processes, each time decreasing ϵ by a factor of 10. Any seed resulting in an infeasible, or corrupt, solution was discarded. 41

4.1. This figure displays the four-sided friction pyramid implemented in this experiment. 46

4.2. This figure displays the proposed method of modeling the 3D friction cone. 48

4.3. This image provides a top-down view of the four-sided friction pyramid from the z-axis. 49

4.4. This image displays how contact was forced on the monopod robot. 50

4.5. This image displays optimal trajectories that implement both the novel method (blue), and the polyhedral approximation (red), of modeling the 3D friction cone. 52

4.6. This image displays the slack variables from the slip trajectories that implemented the novel method of modeling the friction cone, scaled to base 10. The slack variable trajectories are displayed for different ϵ values. . . . 53

4.7. This image displays the slack variables from the slip trajectories that implemented the novel method of modeling the friction cone, scaled to a log scale. The slack variable trajectories are displayed for different ϵ values. 54

4.8. This image displays the effective coefficient of friction, $\mu_{effective} = \frac{\lambda_z}{\mu|\lambda_{\|}|}$. Slip occurred with the effective coefficient clipped at 1.0. These trajectories were seen to converge when $\epsilon \leq 1E-2$. 55

Stellenbosch University https://scholar.sun.ac.za

5.1. The figure displays the expected motion of the non-planar robot conducting a long-time-horizon dynamic trajectory along the x-axis. 57

5.2. This figure displays how a prescribed contact order was encouraged in the steady-state trajectories. The left contact was was constrained to occur in the first half of the optimization. Whereas, the right contact was constrained to occur in the second. Additionally, the right foot was constrained 5cm above ground for the first half of the optimization, and the left foot for the second half. 59

5.3. These images display how the steady-state trajectories are achieved from rest, and how the robot returns back to rest from the apex of the steady-state trajectory. 60

5.4. This image displays the foot-height seen during steady-state trajectories at different speeds. 62

5.5. This image displays the phase plots of all the state variables during steady-state trajectories at all the speeds investigated. 64

5.6. These images display the forward velocity of the robot accelerating too, and decelerating from, the apex of steady-state gaits. 65

5.7. This image displays long-time-horizon trajectories at different speeds. Here, the acceleration, and deceleration, trajectories stitched onto periodic steady-state trajectories steady-state trajectories. 66

5.8. This image displays the correlation between the velocity profile of a sliding mass, and the $2.0m/s$ long-time-horizon trajectory. 67

6.1. This image displays the phases of the long-time-horizon trajectory, including a rapid turn off the sagittal plane. Here, the robot accelerated from a rest position, to the apex of a steady-state gait, maintained the steady-state gait along the x axis, and conducted a rapid turn from the apex of the steady-state gait. The rapid turn ended in the apex of the steady-state gait, offset by the turn angle, maintained the steady-state gait, and decelerated back to rest. 69

6.2. A graphical description of the robot heading, shown in view of the bipedal robot z-axis. The system heading is described by ψ_{body} angle in $\boldsymbol{q}$, and the path heading is described by the Cartesian sum of the $\dot{x}$ and $\dot{y}$ elements of $\dot{\boldsymbol{q}}$. 70

Stellenbosch University https://scholar.sun.ac.za

6.3. This image displays how the rapid turn trajectories start, and ends, in apex pose of the steady-state trajectories. 71

6.4. The image displays optimal trajectories of the change in heading angle of the robot conducting rapid turns at varying speeds. 73

6.5. This image displays optimal trajectories of the change in heading angle of the robot conducting rapid turns at varying degrees. 74

6.6. This image displays optimal trajectories of the change in heading angle of the robot conducting rapid turns towards the inside leg, the left. 75

6.7. This image displays the velocity, and system heading, profile of a 2m/s long-time-horizon trajectory including a 45° rapid turn. 77

Stellenbosch University https://scholar.sun.ac.za

List of Tables

4.1. A tally of equations, variables, and constraints passed to the IPOPT Solver for the trajectory optimization method implementing the respective method 51

6.1. Statistical characteristics of rapid turns conducted at varying speeds. These characteristics were developed using a sample set of 5 trajectories per speed investigated. 73

6.2. Statistical characteristics of turns conducted to varying turn angles. These characteristics were developed using a set of 5 trajectories per turn angle investigated. 74

Stellenbosch University https://scholar.sun.ac.za

Nomenclature

EOM	Equations of motion
COM	Center of mass
DOF	Degree(s) of freedom
MPCC	Mathematical program(s) with complimentarity constriants
3D	three-dimenstions
SLIP	Spring loaded inverted pendulum
IP-OPT	Interior point optimizer

Stellenbosch University https://scholar.sun.ac.za

Chapter 1

Introduction

Research into legged locomotion has been a growing interest in recent years, and its impact in modern life is ever-increasing. However, the bulk of this literature has been focused on reducing energy consumption in periodic steady-state gaits. Little insight has been shown into transient non-planar motion [1].

Rapid locomotion is essential for survival in nature. This need has resulted in the the most successful displays of rapid, and transient, legged locomotion being found in nature [2,3]. It also highlights stark contrast between the capabilities of locomotion found in nature, and robotic locomotion. This performance gap is indicative of a wide knowledge gap [4].

Truly inviting legged robots into our lives requires roboticists to better understand rapid locomotion. Therefore, this thesis aims to bridge the gaps in performance, and knowledge, between robotic locomotion and biological locomotion. Here, trajectory optimization models were used to investigate the effects of contact and friction to better understand complex dynamic bipedal locomotion as shown in Figure 1.1.

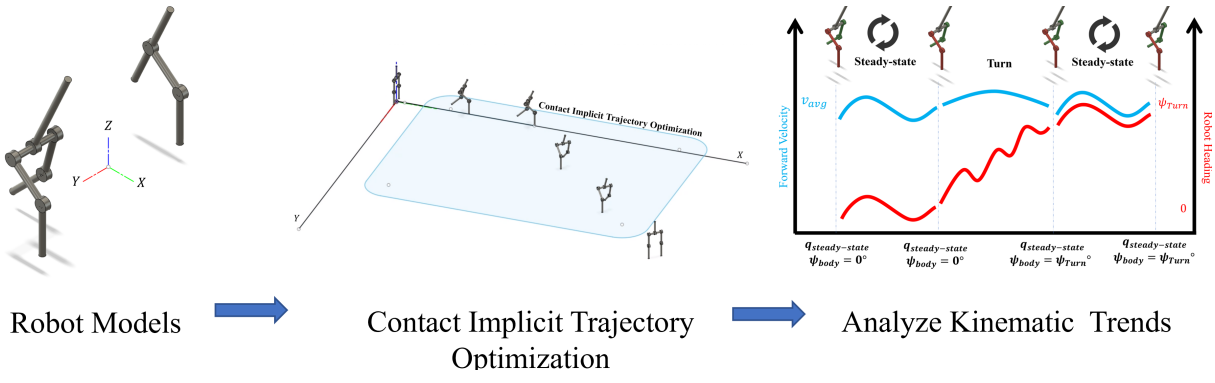

Figure 1.1: This figure provides an overview of the research methodology used in this thesis. Mathematical models of the robots used in this research were implemented in contact-implicit trajectory optimization environments. Thereafter, these resulting trajectories were used to identify emerging trends and heuristics.

Stellenbosch University https://scholar.sun.ac.za

1.1. Motivation Of Study

This study is motivated by the dream of inviting legged robots into our lives. This would allow legged robots to do work unsafe for, or unwanted by, humans. However, employing legged robots in these fields requires the performance gap between legged locomotion in nature and in the lab to reduce: legged robots need to be *at least* as agile as animals.

Most of state-of-the-art robotic literature focuses on achieving robust and periodic steady-state locomotion. Periodicity allows this motion to be described using limiting assumptions of its dynamics: ranging from neglecting the effects of friction [5], massless legs [6], to reduced-order dynamics [7]. These assumptions make robust legged locomotion achievable for simplified periodic motions. Many robotic platforms make use of these simplifications to achieve locomotion at speed. However, they do not hold for rapid and transient motions.

The largest gap between robotic and biological locomotion lies in the ability to control transient motions. This ability is essential in allowing robots to actuate outside of the lab. Unfortunately, assumptions made to achieve robust steady-state motion become relevant when studying rapid transient motions. On slippery surfaces, the effects of friction are essential to maintaining traction. Similarly, understanding how the mass of the robot legs affects the inertia is vital when the robot changes velocity. Additionally, foot-fall patterns (*gaits*) are unknown for transient motions [1, 8]; reduced-order models can not accurately describe the dynamics when the gait is unknown.

Recent literature has employed contact-implicit trajectory optimization methods to model transient motions of rigid bodied robots [4, 8–11]. This research is effective for studying transient motions. However, these studies have often been limited to studying planar motion [1, 4, 10, 12]. Non-planar methods of contact-implicit trajectory optimization remains an intractable task, with inaccurate models [13, 14].

Therefore, research presented in this thesis aims to bridge the knowledge gap between biological locomotion and robotic locomotion by investigating 3D contact implicit trajectory optimization models. This is done to develop methods of accurately understanding the effects of contact on legged robotic platforms, and to investigate optimal transient dynamics.

Stellenbosch University https://scholar.sun.ac.za

1.2. Problem Statement

The bulk of the literature describing robotic legged locomotion is focused on steady-state locomotion. Often, this focus is narrowed further into reducing energy efficiency, or increasing the speed of the locomotion. Insight into transient motions is a recent field of interest, and has been restricted to planar models. To the author's knowledge, no investigations has yet been conducted into how robots can accelerate from, or decelerate too, rest to achieve these gaits in a non-planar environment. 3D dynamic motion also allows for the direction of velocity to change. There has also been limited insight into rapid turning of legged robots.

1.3. Objectives Of The Research

Studying transient motion in non-planar environments is a problem yet to be solved and is fundamental to inviting legged robots into our lives. Therefore, this research aims to use trajectory optimization as a tool to model robotic platforms negotiating contact events in non-planar environments and find dynamically feasible, and torque optimal, trajectories. These trajectories will then be surveyed for any emerging templates, or trends. This research will add to the literature of studying the discontinuous mechanics inherent to legged locomotion by answering the following questions:

1. Is there a better way of understanding of modeling the effects of friction in Mathematical Programs with Complimentarity Constraints (MPCCs)? Chapter 4 aims to adequately answer this question.
2. How to realize dynamic bipedal motion? This is investigated in Chapter 5.
3. How do bipedal robots conduct rapid turns? This is investigated in Chapter 6.

1.4. Scope And Limitations Of Research

The scope of this research involved studying methods of modeling non-planar contact, on a monopedal robot, in a trajectory optimization environment. Thereafter, a bipedal robot model was implemented in this environment, and constrained to conduct complex dynamic tasks.

Stellenbosch University https://scholar.sun.ac.za

In this study, the four-sided polyhedral approximation of the friction cone was compared to a novel method of modeling the friction cone. The contact model implementing the novel method of modeling the isotropic friction cone was applied to a bipedal robot in a trajectory optimization environment. The robot was constrained to complete complex, dynamic tasks at different speeds. Steady-state trajectories were generated along the sagittal plane at speeds ranging from 0.5m/s, to 4.0m/s. Thereafter, acceleration trajectories were generated to bring the robot to the apex of these steady-state gaits from a rest position. Similarly, deceleration trajectories were generated to return the robot back to rest from the apex of these steady-state gaits. Finally, the scope of this thesis concluded with an investigation into rapid turning off the sagittal plane from the apex of these steady-state gaits.

The resulting dynamic trajectories were complex, and computationally intractable. Therefore, certain limitations were implemented on the trajectory optimization models to restrict the solution search space, without removing non-intuitive transient solutions of the dynamic locomotion. The most notable limitation was the amount of discrete elements used to describe the trajectory optimizations. The optimization problems were transcribed into N discrete elements, where N ranged between 50 to 150 elements depending on the task. All contact surfaces were assumed to be hard, inhibiting penetration between the point of contact and the contact surface. Friction was modeled using a uniformed coefficient of friction. This allowed for the 3D friction cone to have isotropic properties to reduce the complexity of modeling it. Additionally, this research did not include a changing coefficient of friction between static friction, and kinetic friction, during slip events. The coefficient of friction remained constant during static, and kinetic, friction events.

1.5. Structure Of Thesis

Figure 1.2 displays how the thesis was structured. Further detail is provided:

- **Chapter 2 - Literature Review And Theory Development**

  This chapter provides a survey of relevant literature relating to legged locomotion. In this chapter, examples of dynamic legged locomotion found in nature is compared to state-of-the-art robotic locomotion. This chapter describes how friction is modeled, and implemented in trajectory optimization programs. Special attention is given to trajectory optimization methods, and how they have been used to model transient contact dynamics.

Stellenbosch University https://scholar.sun.ac.za

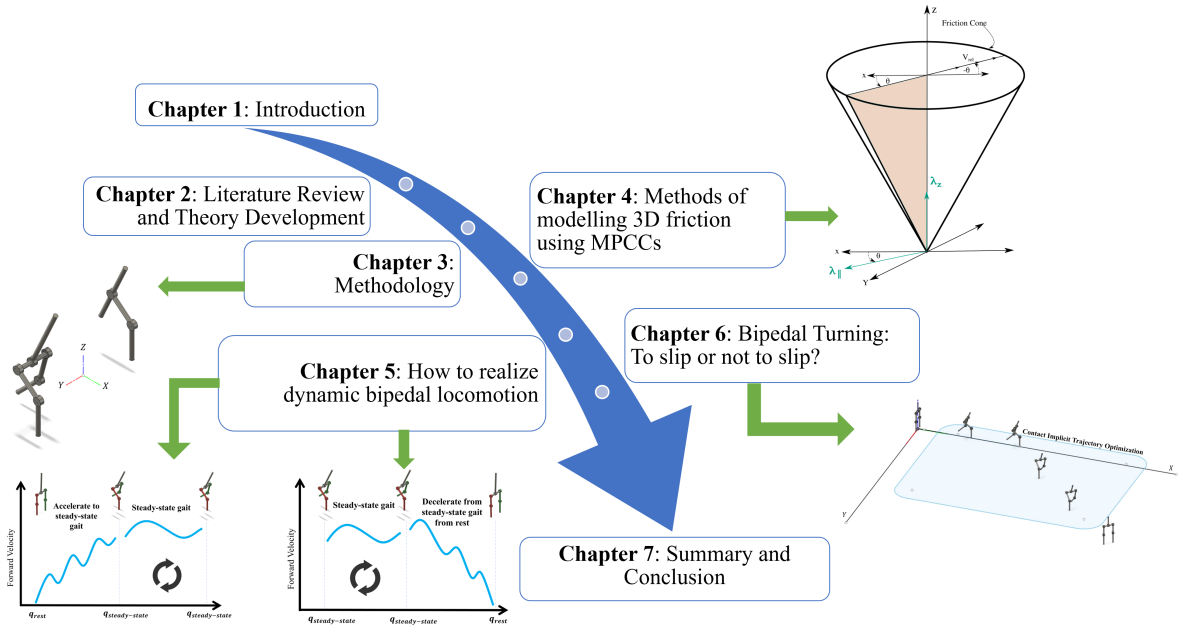

Figure 1.2: This image displays the structure of the thesis. It starts with a brief introduction, followed by a literature review and theory development. Thereafter, a methodology is provided in Chapter 3. Methods of modeling friction using MPCCs are investigated in Chapter 4. Chapter 5 investigates dynamic bipedal motion, and Chapter 6 introduces rapid turning. Finally, Chapter 7 concludes the thesis with a summary, and recommendations for future work.

- **Chapter 3 - Methodology**

  Chapter 3 provides a detailed description of how the trajectory optimization model was implemented. Here, detail is provided of how the dynamics were described and discretized in the trajectory optimization. Additionally, this chapter details how contact implicit trajectory optimization methods were implemented, and solved using relaxation techniques.

- **Chapter 4 - Methods Of Modeling 3D Friction Using MPCCs**

  Chapter 4 investigate methods of modeling the effects of friction and the resultant slip of a monopedal robot in a non-planar environment. It further describes an experiment that compares a novel method for computing the 3D friction cone using a set of complimentarity constraints with the traditional four-sided friction pyramid.

- **Chapter 5 - Realizing Dynamic Bipedal Motion**

  Thereafter Chapter 5 applies the novel method for modeling friction and resultant slip on a larger trajectory optimization model of a bipedal robot in a non-planar environment. Multiple periodic steady-state running gaits were generated at different speeds. Acceleration, and deceleration, trajectories were generated to prove the realizability of the steady-state gaits: that we can accelerate from rest to, and decelerate to rest from, the apex of each steady-state gait. These trajectories were

Stellenbosch University https://scholar.sun.ac.za

then stitched together to generate a long-time-horizon trajectory along the sagittal plane.

- **Chapter 6 - Bipedal Turning: To Slip Or Not To Slip?**

  Chapter 6 presents a series of rapid turns from the apex of the steady-state trajectories. This is done to investigate the prevalence of slip during, and to comment on kinematic trends emerging from, rapid turns. Additionally, a 2m/s rapid turn trajectory 45° off the sagittal plane is stitched onto the acceleration, deceleration, and steady-state trajectories generated in Chaper 5. Including the rapid turn trajectory produces a long-time-horizon trajectory that turns off the sagittal plane.

- **Chapter 7 - Summary, Conclusion and Future Work**

  Chapter 7 concludes the thesis by presenting a summary of the work done in this thesis. A discussion of the main findings is presented, along with recommendations for future-research.

1.6. Publications

Two publications resulted from this study. The first one listed below was published, and the second one is currently under review:

1. D. Pretorius and C. Fisher, "A novel method for computing the 3D friction cone using complimentary constraints," in *2021 International Conference on Robotics and Automation (ICRA)*, 2021.

2. D. Pretorius and C. Fisher, "Bipedal turning: To slip or not," *IEEE Robotics and Automation Letters, Under Review,* 2022.

Stellenbosch University https://scholar.sun.ac.za

Chapter 2

Literature Review And Theory Development

Maneuverability is defined as the ability to control the change in magnitude and direction of velocity to achieve a goal [15, 16]. It is used to negotiate and overcome obstacles in the unpredictable environment in which we live. However, with the bulk of legged robotic literature focusing on steady-state movements [8], maneuverability is one of the largest shortcomings of legged robotics literature [17].

Nature provides examples of the the most successful implementation of maneuverable legged locomotion. As shown in Figure 2.1a animals are known to walk and run within hours from birth [8, 18]. Whereas, 40 years after the development of Raibert's dynamic bipedal robot [19–21], only a few robots have displayed maneuverable dynamic locomotion in real world environments, such as Boston Dynamic's Atlas in Figure 2.1b [22]. Recently, Atlas has been shown dancing in [23], and performing parkour in [24]. However, these are exceptions to the robotics norm, with most legged robots struggling to obtain dynamic locomotion without additional support [8]. This exposes stark contrast between the agility of animal locomotion, and bipedal robotic locomotion. Truly inviting robots into our world requires roboticists to understand how agile tasks are conducted in nature, and replicating these abilities on robotic platforms.

This chapter aims to survey current literature relating to the development of legged robotics, and develop the theory necessary for the rest of the thesis. First, this chapter investigates implementations of dynamic locomotion in nature. Here, we investigate the optimal number of legs needed for legged locomotion, gait selection as a function of the speed, and examples of maneuverability in nature. Thereafter, a brief overview of inelastic contact, and non-planar friction will be provided. Finally, this chapter will conclude by exploring how trajectory optimization has aided in controlling robotic locomotion.

Stellenbosch University https://scholar.sun.ac.za

(a) Image of a zebra walking 30 minutes after birth. This image was presented in [25].

(b) Image of Atlas Robot walking outside the lab. This image was presented in [22].

Figure 2.1: This image displays new-born zebra locomotion, and robotic locomotion of the Atlas robot.

2.1. Dynamic Locomotion In Nature

Since its inception, robotics literature has been motivated to achieve the level of locomotion found in nature. Animals have evolved to leverage legged locomotion to overcome practical challenges and to survive the onslaught of natural selection [2, 3]. Faster, more agile, predators catch slower prey continuing the lineage of the predatory species. Similarly, faster prey escape slower predators, surviving to continue the survival of the species [3, 17]. Multiple implementations of legged locomotion with varying amount of legs are evident in nature.

2.1.1. How Many Legs Are Best?

General consensus has not yet been reached on the optimal number of legs necessary for dynamic locomotion. Nature provides many examples of animals leveraging multi-legged form-factors surviving in their environments; with each example equally compelling for their intended environment.

Monopedal animals are not found in nature. However, kangaroos, some birds, and rodents exhibit monopedal characteristics when they move, using both feet in phase to hop [3, 5]. Although these animals are technically bipedal animals they display monopedal characteristics. Monopedal control suffers from a lack of balance as a result of using one contact point for both balance, and translation - making foot placement, and body orientation vital in solving the control problem. This adds to the notoriety of free-bodied

Stellenbosch University https://scholar.sun.ac.za

monopedal control being one of the toughest control problems in locomotive literature [2,5]. Supporting monopod robots with a boom, constraining its motion to the sagittal plan, solves this problem [8]. Ironically, robotic literature often introduces locomotion and presents proof on concepts, using monopedal robots [5, 8, 26].

In bipedal motion, the provision of an extra leg acts as a inertial counter-balance and reduces the dependence on foot placement; making the platform more dynamically stable, without addressing the static instability [5]. Typically, robots are developed without ankles, modeling contact using point feet to reduce weight and actuation complexity [5,8,19]. This allows biped robots to maintain stability while moving (walking or running). However, it makes bipedal robots unstable at rest. A simple solution to this static instability is the inclusion of feet (contact surfaces replacing contact points). Examples of bipedal animals exist in many natural environments: penguins use a bipedal form factor for underwater agility, and ostriches and humans leverage a bipedal form factor for overland agility [2, 3]. Robotic literature is often biased towards bipedal locomotion as it can be applied to the humanoid form-factor and directly integrates into our lives [7]. Examples of dynamic bipedal robots include Boston Dynamic's Atlas Robot, Raibbert's bipedal robot, and ATRIAS [19, 22, 27].

Quadrupedal locomotion solves the static stability problems faced by bipedal locomotion. With one leg in the air, the availability of three additional contact points allow for static stability. However, coordination problems between legs arise when translating quadrupedal platforms [5]. Additionally, footfall patterns (gaits) are often aided by back flexibility - raising additional dynamic complications [2]. Nature tends to favor quadrupedal locomotion for dynamic motion and provides multiple examples of medium-sized quadruped animals thriving in multiple settings, ranging from nimble dogs, slow tortoises, fast cheetahs, heavy-set elephants, to lanky giraffes [3]. Multiple examples of dynamic quadruped robots are also available: Boston Dynamic's Big Dog, MIT's Cheetah 3, and ETH's ANYmal [28–30].

Additionally, animals leveraging more legs for locomotion are found in smaller form-factors. Most insects leverage hexapedal locomotion to move: including ants, beetles, and cockroaches. Additionally, spiders, and octopuses leverage octapedal locomotion. These form-factors are not prevalent in the mammal community, and are beneficial for rapid static movements - amplifying the dynamic coordination problem [2, 3, 5].

The question relating to the optimal amount of legs for legged locomotion remains unanswered. However, there is general consensus about using monopedal robots as introductory examples to robotic literature, and to prove concepts [4, 5, 8]. Additionally, the parallels between the bipedal and humanoid form factor provide promise for integrating bipedal robots into our human lives [7]. However, this does not limit the promise and

Stellenbosch University https://scholar.sun.ac.za

growth of quadrupedal robots. Although quadrupedal robots provide larger coordination and control problems, the prevalence of the quadrupedal form-factor for dynamic motion in nature is indicative of nature's bias towards this form factor. Additionally, with limited resources, higher order robotic locomotion has not yet sufficiently been explored [13].

In this thesis, two robot form factors will be used with point feet, as opposed to flat feet. Chapter 4 presents a novel method of modeling friction events. Therefore, a monopedal robot will be used to introduce the novel method of contact modeling. Once contact dynamics have been sufficiently explored, Chapters 5 and 6 investigate forms of dynamic bipedal motion.

2.1.2. Gait Selection: What To Do With My Feet?

Humans walk to achieve slow locomotion, and run to move fast [3]. These are two distinct footfall patterns (*gaits*) and indicate the need to change how we move at different speeds. Gaits refer to the pattern of steps of an animal at a particular speeds. Alexander et. al attributes the change in gait to the optimizing of energy expenditure at different speeds [2]. It is more metabolically efficient to run at higher speeds, than it is to walk [3, 5].

Hoyt et. al. released a study comparing the metabolic efficiency of horses conducting various gaits on a treadmill [31]. These horses were commanded to walk, trot, or gallop at various speeds, and their oxygen consumption was measured while completing these tasks. This research concluded that walking was the most economic gait at speeds below 1.7m/s. Whereas, trotting was the most economic gait between 1.7m/s, and 4.6m/s. At higher speeds, galloping was the most economic gait. Thereafter, the horses were allowed to move freely within a marked grid. It was seen that the horses chose to move at metabolically optimal speeds for each gait.

Similarly, [32] revealed the optimal speed for humans to change between running and walking occurred at 2.2m/s. Wirtz et. al noted that walking commuters within urban areas walk an average of 1.5m/s, a speed known to minimize the metabolic cost per unit distance [33].

Alexander et. al. studied videos of animals of various species, and form-factors, moving at different speeds and noticed a trend in gait transitions [3]. This study revealed that a shift from walking-to-running, on bipedal animals, and walking-to-trotting on quadrupedal animals occurred at a Froude Number around 0.5 ($F_r = 0.5$). Here, $F_r = v^2/Lg$, where v is the forward velocity of the animal, L is the leg length, and g is the gravitational constant. For humans, on earth, this transition was seen at forward velocities at 2m/s,

Stellenbosch University https://scholar.sun.ac.za

matching observations made by [5]. For the bipedal robot described in this thesis, the F_r dictates an optimal walk-run transition speed of 1.42m/s. Additional constraints were applied to force running gaits at lower speeds as described in Chapter 5.

Walking is a dynamically stable gait, maintaining at least one leg on the ground at all times. Consequently, the length of the leg limits the length of the stride. Faster walking gaits are dependent on longer legs, or increasing the swing speed of the leg above its natural swing speed (if it behaved as a simple pendulum). However, increasing the swing speed of the leg above its natural swing speed dramatically increases the metabolic cost. The switch from walking to running occurs when additional energy is added to increase the swing speed of the leg above its natural swing frequency. At this point, it becomes more metabolically efficient to introduce a flight period and start running. This allows the swing leg more time, and greater swing distance, to swing forward. Running is defined as a bipedal gait with an observable flight period, where both feet are off the ground for a period of time [3, 5]. Figure 2.2 displays the mechanical difference between the human running and walking gaits [34, 35].

Running is a vague term, with different interpretations ranging from jogging, to sprinting. Where jogging includes a full forefoot-to-heel strike, and sprinting only including a forefoot-strike. Perkins et. al. [5] attributes the motion of jogging to modern shoes spreading the contact force across the foot. The use of point contacts in this thesis drew parallels between the running trajectories presented and sprinting.

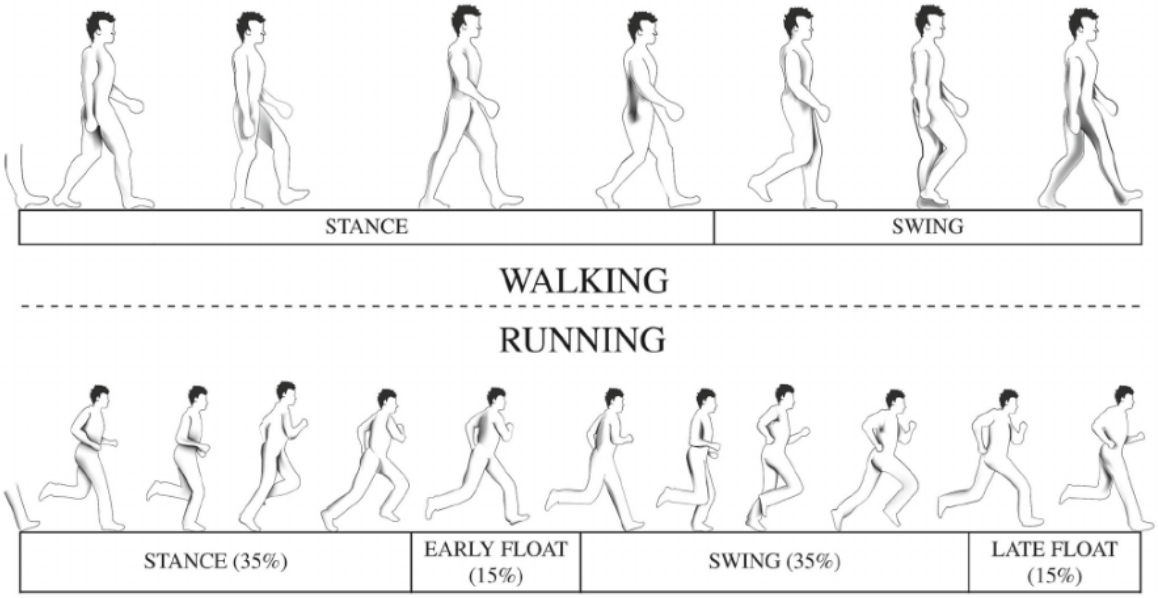

Figure 2.2: This image displays the differences between the human run and walk gaits. This image was presented in [34].

Stellenbosch University https://scholar.sun.ac.za

2.1.3. Implementations At Speed

Intermittent contact events poses the largest problem according to robotics literature [8]. Contact events are highly discontinuous and result in sharp impulsive forces affecting the dynamics of the system. The identification of periodic gait patterns allowed for the planning and control of predictable contact events. Knowing when and where contact occures, allows you to respond accordingly [7].

Predictable contact events allows for heuristics, hybrid dynamics, and dynamic assumptions to be implemented. These assumptions neglect the effects of slip, and the inertial effects of the mass of limbs [8]. Many robotic platforms including Cassie, ATRIAS, and the Cheetah 3, have achieved stable gaits through the implementation of hybrid dynamics [27, 36, 37]. Here, two sets of continuous Equations Of Motion (EOM) were generated for contact and flight phases, with impulsive contact-initiation and lift-off events separating them.

Similarly, predictable gaits allow for the generation of reduced order templates. The Spring-Loaded Linear Inverted Pendulum (SLIP) simplifies the dynamics of the Center Of Mass (COM), capturing the contact and flight phases during dynamic running motions. Describing these phases allow roboticists to infer foot-fall patterns and generate stable steady-state motions. After [38] implemented the SLIP model on a planar bipedal platform, Wensing et. al. applied it in in a non-planar environment, on a humanoid platform [7].

To date, multiple gaits on all forms of legged platforms has been reported in robotics literature. Monopedal hopping is a common gait found in both fast and slow monopedal motions. Bipedal walking has been achieved for slower motions, and different forms of running has been achieved for faster bipedal motions [1, 5, 7, 8]. Park et. al. [39] presented the fastest bipedal running gait on the Raptor robot, shown in Figure 2.3a.

Quadrupedal walking has been achieved for slower motions, while pronking and trotting have been achieved for intermediary quadrupedal speeds. Bounding, and galloping has also been achieved for faster quadrupedal motions [14, 36, 40]. Boston Dynamics presented the fastest quadrupedal gallop on the MIT Cheetah robot, shown in Figure 2.3b. However, literature provides few examples of robotic platforms implementing galloping gaits. This is due to few quadrupedal robotic platforms making it past the transition speed where galloping becomes the optimal gait. Spine flexibility necessary for roll, and yaw, actuation while galloping adds to the complexities of achieving this gait on robotic platforms [8, 36]. Additionally, high speed hexapedal tripod gaits [13, 41] have been achieved on robotic platforms.

Stellenbosch University https://scholar.sun.ac.za

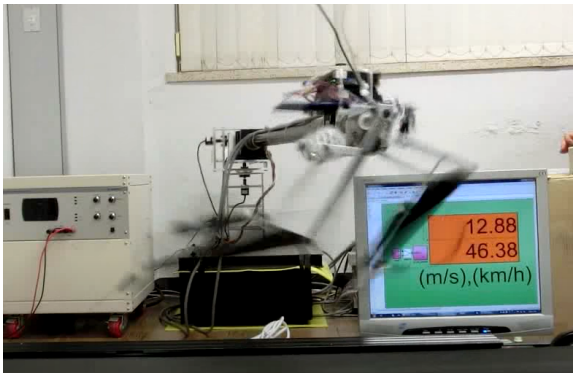

(a) Image of the KAIST Raptor recording the fastest bipedal robotic run [39]. This image is from [42].

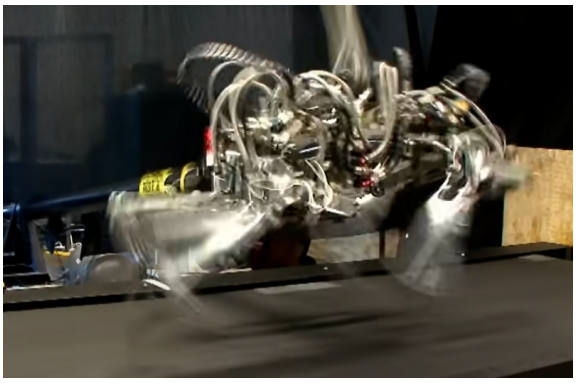

(b) Image of the MIT Cheetah achieving the fastest quadruped robotic gallop. This image is from [43].

Figure 2.3: This image displays the fasted implementation of robotic bipedal and quadrupedal locomotion.

Implementing these high speed gaits has been much of the focus in the legged robotics community. However, during implementation transient disturbances, which may be unstable, are often noticed moments after initiating the system [44]. Perkins et. al. developed a controller for generating steady-state running gaits on a simulated bipedal robot, and transient effects were noticed during the first 2 seconds of the simulation. Even after 300s, the system had not converged to a true limit cycle, however was deemed to be stable. It was noted that the magnitude of these transient disturbances scaled in magnitude, and time duration, proportionally to the speed of the steady-state gait [5].

These reduced order templates, heuristics, and hybrid dynamics allowed for the development of reliable and robust running gaits at high speeds. They accurately describe steady-state motion, maintaining a desired forward velocity shown in Figure 2.4. However, research into agile transient motions has been limited [1, 3, 9].

2.1.4. Maneuverability: How To Achieve Speed, And What To Do At Speed?

Studies have shown that animals spend very little of their time maintaining a speed. Rather, much of the life of both predator and prey is spent remaining at rest. Predators spend most of their days idle, and rely rather in their ability to change speed when capturing prey. Similarly, species of prey spend most of their days grazing and walking slowly. While, their survival relies rather on their ability to quickly evade predators using transient motion [3, 8, 17].

Wilson et. al. published research describing the the hunting patterns of a group of

Stellenbosch University https://scholar.sun.ac.za

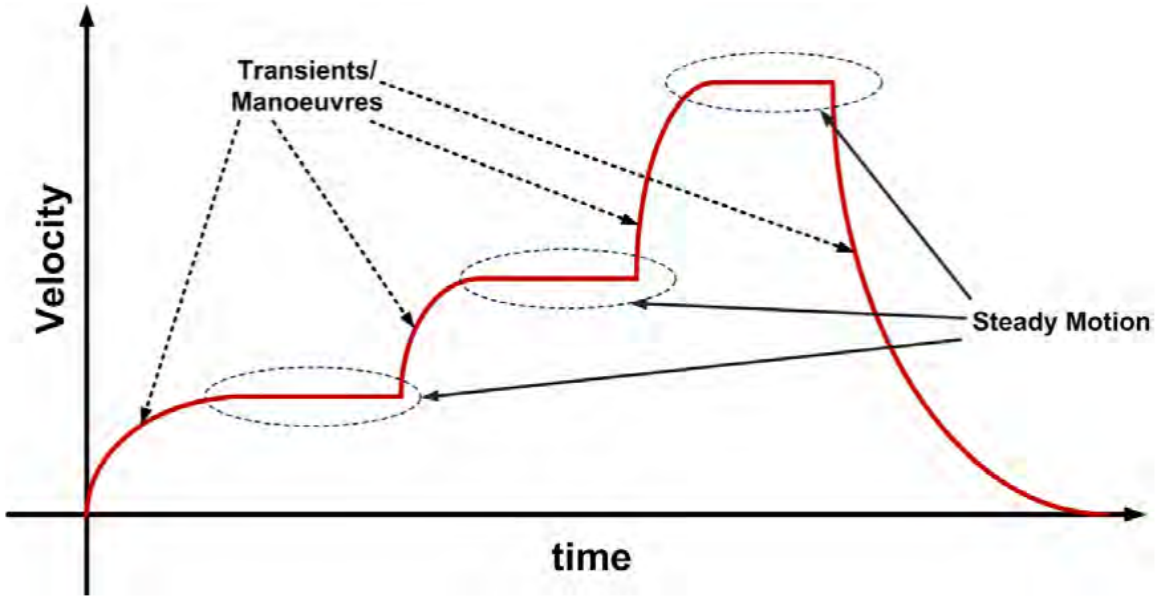

Figure 2.4: This image, from [15], displays the affect that transient motions have on forward velocity compared to steady-state. Here, steady-state motions maintain a desired velocity and transient motions change the velocity.

wild cheetahs in Botswana [45]. Over a period of 17 months, the cheetahs were tracked using collars equipped with Inertial Measurement Units (IMU) and Global Positioning Systems (GPS). This research revealed that cheetahs seldom run at their top speeds. The fastest speed tracked in this research was 25.8m/s[1]. Rather, accelerations of up to 18m/s^2 was observed, indicating that the success of hunts rely heavily on this ability to rapidly accelerate [45].

Williams et. al. studied polo ponies, and greyhound dogs, noting that at lower speeds rapid acceleration and deceleration were limited by the animal controlling its pitch: tail up during acceleration, and nose up during deceleration. Whereas, at higher speeds, the rate of rapid acceleration or deceleration was limited by available muscle power [47]. This motivated the use of a linear motor model to replicate these limitations on the trajectories presented in this thesis [8, 48, 49].

Similarly, studies have investigated the rapid transient abilities of other animals: domestication of dogs allowed for wide studies into their acceleration abilities [50–52], while rapid turning investigations have been conducted using goats, horses, ostriches, and chipmunks [53–55].

Transient robotic locomotion is a part of robotic literature yet to be mastered. The ability to conduct rapid motions are key to survival in nature, and integrating robots into our lives [8]. Therefore, roboticists need to recreate these abilities on robotics platforms [57].

[1]The fastest recorded speed of a cheetah running was 29m/s [46]

Stellenbosch University https://scholar.sun.ac.za

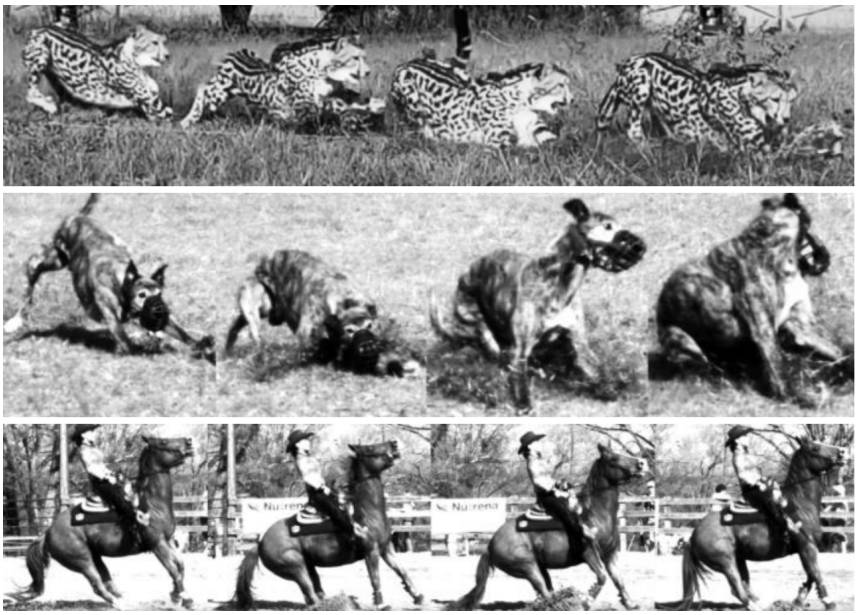

Figure 2.5: This image, from [56], displays the rapid deceleration of a cheetah, greyhound dog, and horse. Slip is evident in these examples of rapid deceleration.

Bar the exception of the Atlas Robot conducting parkour [24] and dancing [23], much of current robotic platforms are not known for being agile or conducting rapid motions. Therefore, understanding how these events occur are vital to the goal of inviting robots into our lives.

It involves complex systems described by highly discontinuous mechanics [3]. These discontinuous mechanics are largely related to the aperiodic foot contact sequences, and the additional effects of ground contact (friction and slip) [8], as seen in Figure 2.5. Figure 2.5 displays footage of a cheetah, greyhound dog, and horse conducting rapid deceleration [56]. Finding solutions to models describing these systems are notorious for being computationally intractable - constraining the development of literature relating to transient locomotion.

Changing Magnitude Of velocity

In [4, 26], Hubicki et. al. generated multiple long-time-horizon trajectories of a planar monopod hopper with a spring leg starting at rest, and ending at rest 20 steps later. It was noticed that these trajectories quickly accelerated towards a limit cycle, maintained the limit cycle (in a steady-state gait), and then abruptly decelerated to rest. Thereafter, direct correlation was noticed in the forward velocity profile compared to that of a minimum time control of a sliding mass. This study revealed that the forward velocity profile of a long-time-horizon (including rapid acceleration and deceleration phases) could be accurately described by that of a 1 degree of freedom (DOF) sliding mass. Further, Hubicki

Stellenbosch University https://scholar.sun.ac.za

hypothesised that this template would hold for more complex models [4, 26].

Thereafter, Fisher et. al. confirmed this hypothesis in [1]. Here, the long-time-horizon trajectory of bipedal and quadrupedal robots were split into separate tasks (acceleration, periodic steady-state, and deceleration) to be optimized separately, and later stitched together. This increased the resolution, and reduced the computational complexity of the optimization. Thereafter, a 30m long-time-horizon trajectory was generated and correlated directly with the split, and then stitched, trajectories. Slip effects were noticed during the transient acceleration and deceleration trajectories, similar to that seen in Figure 2.5. Additionally, the sliding mass template emerged when analyzing the forward velocity profiles of both the biped, and quadruped models; confirming Hubicki's hypothesis of the template holding for more complex models [4, 26].

Similar stitching techniques were implemented in this thesis when generating long-time-horizon trajectories. Here, trajectories were split into acceleration, deceleration, periodic steady-state phases. In Chapter 5 the stitching method was implemented to generate a long-time-horizon trajectories on a non-planar bipedal robot; again, confirming Hubicki's hypothesis holding for more complex models [4, 26]. Further, in Chapter 6 an additional rapid turn trajectory is added to the long-time-horizon trajectory.

Changing Direction Of velocity

In recreational sporting events, human agility is shown when athletes rapidly change their heading angle. This is seen in rugby's *side-step*, soccer's *side-fake*, and basketball's *lay-up*. Similar motions are seen in the survival of animals in predatory avoidance, or in pursuit of prey. The cheetah is known to whip its tails in pursuit of prey, buck are built light and nimble to rapidly change its heading direction in evading predators. Changing the heading direction of both the body, and its velocity is crucial in animal and robotic agility.

Many robots are known to complete static turns in planned and sanitized laboratory environments [5], these robots include ASIMO [58], HRP-4C [59], and SDR-4X [60]. The prospect of robots having to slow down while conducting rapid turns, or engaging with unpredictable real world through a support rig is impractical and motivates this investigation.

Brilliant work has been conducted in achieving this dynamic robotic turns. Carlo et. al. [36] reported 180°/s turn rates on the MIT Cheetah 3. Agile rapid turn motions were presented by Boston Dynamic's Atlas robot. Similarly, Degrave et. al. [40] investigated turning strategies on the Oncilla robot. However, these examples prove to be exceptions from the norm. Robotics literature does not provide many other examples of successful

Stellenbosch University https://scholar.sun.ac.za

Figure 2.6: This image, from [61], displays a cheetah conducting a rapid turn. Note the extrusion of its claws, and the flexing of its paw, to increase its traction and control the effects of friction.

rapid, and dynamic, turns under irregular conditions.

Wensing et. al. generated high speed turn trajectories using 3D SLIP techniques on a 26 DOF huamnoid robot [7]. This model used known COM dynamics of a bipedal robot, and inferred a periodic contact order from the COM trajectory. Additionally, these trajectories inspired controllers to transition from periodic running to a turn.

Perkin's et. al. [5] developed a set of heuristics needed for different stages of dynamic motion: acceleration, deceleration, steady-state motion, and turning. Thereafter, these heuristics were used to develop controllers and applied to the different stages. Simulated turns, to both the inside and outside direction, were generated at rates of $45°/s$.

In 2020, Knemeyer et. al. presented a trajectory of a quadruped conducting a turn $60°$ off the coronal plane. This trajectory was initialized using three periodic gaits as the starting point [14]. Seeding trajectories with known periodic gaits aid the solver to find feasible solutions to the optimization problem. However, it biases the solution towards local minima close to these known periodic gaits.

Within nature, it is often noted that dynamics describing transient motion are often different from dynamics related to periodic motion. Therefore, this thesis presents experiments in which rapid turn trajectories were generated from randomized seed points. This allowed for non-intuitive solutions to rapid tasks.

Stellenbosch University https://scholar.sun.ac.za

2.2. Traction And Slip Modeling

Traction plays a pivotal role in conducting rapid transient motions. Williams et. al. [47] commented on how traction could limit the rate of acceleration and deceleration. However, this was not quantified, as slip events did not occur in their study. In nature, animals are often observed to slip while conducting rapid transient motions [8, 62]. Slip was seen to occur in all rapid trajectories presented in this thesis. Similarly, Fisher et. al. noticed slip occur in long-time-horizon trajectories presented in [1, 8]. Therefore, a comprehensive understanding how slip occurs and the role it plays in legged locomotion is prudent.

Slip is a byproduct of friction. Friction is a non-conservative force, removing energy from the system, and is described using discontinuous dynamics [63]. Slip occurs once Coulomb's Law is satisfied, further altering the dynamics of the system [11]. With simplifying assumptions regarding the nature of the contact surface, roboticists and tribologists can better understand the mechanics of slip.

Rigid-bodied contact occurs when two bodies collide without changing form [11, 64]. This simplifies the dynamics of the contact event allowing Newton's third law [65, 66] to describe the normal contact force, perpendicular to the contact surface. This normal contact force produces reactive friction forces acting tangentially to the contact surface at the point of contact [63]. Da Vinci, Coulomb, and Amontons et. al. [67–69] noted the following characteristics of the reactive force:

- The tangential friction force is proportionally to the Normal Contact Force.
- The friction force is independent of the area of contact.
- The friction force is independent to the magnitude of velocity during slip [70], such that:

$$|\boldsymbol{\lambda}_{\parallel}| \leq \mu \lambda_z. \tag{2.1}$$

These observations were summarized into Coulomb's Law of Dry Friction [64], which states that on a surface with a coefficient of friction, μ, the magnitude of the friction, $|\boldsymbol{\lambda}_{\parallel}|$, is bound by the normal contact force, λ_z, scaled by the coefficient of friction [57]. The discontinuities of slip lies in the satisfaction of Coulomb's Law - slip only occurs once the magnitude of friction equals the normal contact force scaled by the coefficient of friction [70]. This bounds the friction force by the normal contact force scaled by the coefficient of friction [64].

Stellenbosch University https://scholar.sun.ac.za

Additionally, the direction of the applied friction is determined by the Maximum Dissipation Principle [11, 63]. This states that the direction of applied friction maximizes the rate of kinetic energy dissipation. On a surface with a uniformed coefficient of friction, these laws and principles are applied equally around the normal contact force. Therefore, in 3D environments, the effects of friction are visualized as an isotropic cone centered on the normal contact force, bound by (2.1), as shown in Figure 2.7a. However, on surfaces with a varying coefficient of friction, where $\boldsymbol{\mu} = [\mu_1 \ \mu_2]^T$, friction forces are not applied equally, and asymmetric friction forces are applied. This results in an an-isotropic friction cone describing the effects of the friction, as shown in Figure 2.7b.

Here, T is magnitude of the friction force, and $\mathcal{C}$ is the friction cone, λ_T represents the friction force, and γ_T represents the relative velocity at contact [70]. Note that in the isotropic friction cone, shown in Figure 2.7a, the friction force, λ_T, and velocity at contact, γ_T, are collinear. However, λ_T is negatively scaled by T, satisfying the Maximum Dissipation Principle.

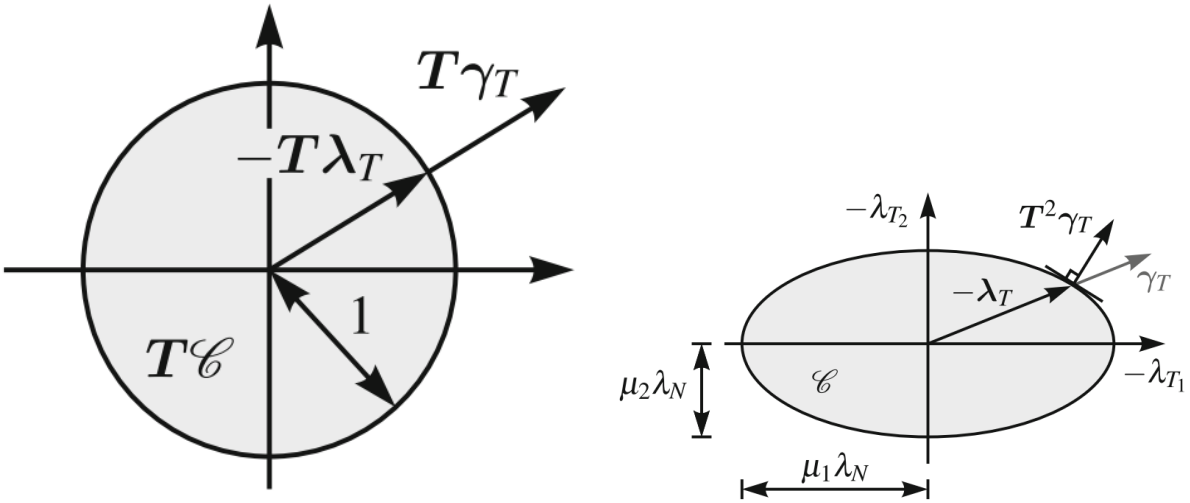

(a) Image of the isotropic friction cone

(b) Image of the an-isotropic friction cone.

Figure 2.7: This image, from [70], displays top-down views of the isotropic, and an-isotropic, friction cones.

Often, robotics literature tends to neglect or approximate the effects of friction [5, 7]. Traditional methods of modeling non-planar contact in robotic literature either underestimate the effects of friction by implementing the 3D friction polyhedral, or completely neglect the effects of friction [6, 11, 71]. However, accurate modeling of friction and the resultant slip is vital to the development of legged locomotion.

In this thesis, rigid-bodied contact is modeled on a surface with a uniformed coefficient of friction. Therefore, a isotropic friction cone is implemented in Chapter 4. Additionally, Chapter 4 contributes to literature by presenting a novel method of modeling the 3D

Stellenbosch University https://scholar.sun.ac.za

friction cone in trajectory optimization methods [57].

2.3. Trajectory Optimization

Trajectory optimization is a mathematical tool for computing multi-dimensional trajectories that satisfy a set of constraints, while minimizing an objective function. Solutions are found by varying a set of decision variables between variable bounds until it converges to a locally optimal solution that satisfies all constraints described in the model [72]. Once all constraints and bounds are satisfied, the solution is considered feasible. It is regarded optimal once it is feasible, and minimizes a defined objective function [8].

Often it is used as a tool to find a path that minimizes some form of energy consumption. It has been applied to minimize battery power usage during drone flight, and fuel consumption during space flight [4, 73]. Minimizing battery power usage is essential for drone flight, and minimizing fuel usage is essential for space flight. Alexander et. al. [2,3] suggested using trajectory optimization as a tool to aid the development of robotic locomotion. Recently, many of the developments in legged robotics literature has been inspired by optimization techniques [1, 4, 8, 10, 12, 14, 26, 61, 74, 75].

2.3.1. Objective Function

Rigid-bodied legged locomotion problems are often characterized by nonlinear dynamics. Non-linear problems are described using piece-wise functions, and solved using gradient descent methods to iteratively minimize the objective. Piece-wise problems result in non-convex solution spaces. Only local minima may be found within non-convex solution spaces [72].

Local minima minimizes the objective function within a small region in the solution space [65, 72]. This region in the solution space may change depending on where the problem is initialized. Experiments conducted in this thesis employ direct methods of trajectory optimization, with the starting point randomized to investigate non-intuitive areas of the solution space [76].

With the bulk of research in legged robotics focused on energy-efficient periodic motions, most available cost functions aim to minimize some form of energy consumption [4, 8]. However, general consensus has not yet been reached on intuitive cost functions for transient tasks [8]. Alexander et. al. notes that most animal locomotion aims at minimizing a metabolic cost of transport [2, 3]. Therefore, a combination of a minimum time objective

Stellenbosch University https://scholar.sun.ac.za

and a minimum work objectives are used in this research. This is further described in Chapter 3.

2.3.2. Formulating The Problem - Direct Methods

Direct methods of optimizing trajectories are generally implemented by discretizing the decision variables using shooting methods or collocation methods [4, 8]. These methods of discretization are known as transcription methods [72].

In shooting methods, the optimizer only varies a disctretized control input, initial conditions, and final conditions to simulate a continuous trajectory. Here, the simulated trajectories are transcribed using a pre-determined discretization frequency. The control inputs get integrated throughout the trajectory, and the optimizer aims to find the correct set of control inputs to guide the continuous trajectory from the initial conditions to the final conditions. These methods are often used for simple optimization problems with continuous dynamics, and simple control laws [4,72]. Additionally, since the trajectory is not a decision variable and is simulated, shooting methods do not support the implementation of path constraints.

Initially, Stewart et. al. [11, 64] formulated contact-implicit trajectory optimization methods as a multiple-shooting optimization problem. However, it was determined that modeling contact dynamics of legged locomotion required more flexibility than fixed time-based integrators. Therefore, Posa et. al. [10, 75] proposed modeling the contact dynamics with variable timestep integrators as a collocation based optimization problem.

Collocation methods integrate the system dynamics as a set of equality constraint [4, 8, 72]. This allows both the optimized trajectory, and control inputs, to be discretized using equality constraints; forcing the trajectory to find optimal solutions while maintaining a feasible set of dynamics. Additionally, the trajectory could be initialized, and constrained within a specific region, since all values in the trajectory are considered optimizer decision variables. In this thesis, direct methods of optimization is implemented and discretized using third-order orthogonal collocation methods [9]. A description of this implementation is provided in Section 3.1.

2.3.3. Contact Implicit Optimization

Experiments conducted in this thesis aimed to find non-intuitive methods of conducting transient dynamic locomotion. Contact implicit optimization allows for contact dynamics

Stellenbosch University https://scholar.sun.ac.za

to be modeled as decision variables to be optimized. This allows for an optimal contact sequence to be determined, without having to explicitly state a contact order or duration. Additionally, research into legged locomotion requires multiple contacts to be optimized: one contact for the monopod, and two for the biped.

Contact implicit trajectory optimizations frame contact dynamics as a set of Mathematical Programs with Complimentarity Constraints (MPCCs); where the product of two positively bound variables, α and β, are constrained to be zero $(\alpha \cdot \beta = 0)$[2]. This is achieved by using the law of non-interpenetration of rigid bodies to model inelastic contact events. Further, Coulomb's Law is satisfied by allowing the contact to slip, and altering the system dynamics, when the friction cone is violated [10, 11].

Collocation Methods In Contact Implicit Optimization

Stewart and Trickle et. al. [11] presented contact implicit trajectory optimization by simulating the dynamics of a rigid-bodied system in terms of impulses and velocities using multiple-shooting techniques. This allowed for the ground reaction forces (GRF) to be modeled as a set of impulses acting on a simulated trajectory. Both friction, and contact dynamics were described in this model. Here, the optimizer had no control of the trajectory, and could only find feasible GRF profiles that resulted in optimal simulated trajectories.

Posa et. al. [10,75] applied this method of contact modeling into orthogonal collocation methods of trajectory optimization. This allowed the optimizer to alter both the dynamics of the system, and the GRF applied to the system. The GRF was included in the set of decision variables, allowing the optimizer to toggle the GRF as needed to produce feasible, and locally optimal, trajectories inclusive of contact dynamics.

A variable time-step was used to apply the complimentarity constraint at the beginning of the discrete time-step, determing the state of contact. Thereafter, the splines could approximate the change in dynamics needed to satisfy the complimentarity constraint; giving the optimizer freedom to make or break the contact to produce dynamically feasible trajectories. Removing the need for prior knowledge of the characteristics of contact. Backwards-Euler integration schemes were used to transcribe the dynamics of the optimization using linear splines. However, it resulted in low accuracy optimization results within an order of $O(\frac{1}{N})$, and was infeasible for use on the 26 DOF FastRunner Robot. Sufficient accuracy could be achieved by increasing N to increase the amount of discrete elements defining the trajectory, or by employing higher-order integration tech-

[2] A comprehensive description of MPCCs, and their implementations, are provided in Chapter 3

Stellenbosch University https://scholar.sun.ac.za

niques. Contact-Implicit optimization techniques are notorious for being computationally intractable. Increasing the amount of discrete time-steps in a computationally intractable program further increases the computational complexity of the problem.

Therefore, instead of increasing the resolution of the contact dynamics, Patel and Manchester et. al. proposed methods of maintaining the amount of discrete points describing the trajectory, while using higher order splines to integrate the dynamics between node points. Manchester proposed the use of variational integrators to integrate the contact dynamics using second order splines [12]. Similarly, Patel et. al. proposed integrating the dynamics using cubic splines [9]. This maintains the resolution of the contact dynamics while smoothing out the state-vector trajectories, increasing its accuracy within an order of $O(\frac{1}{N}^{2K-1})$, where K is the order of the approximating spline. Trajectories implemented in this thesis employed Patel's third order dynamic integration methods, such that $K = 3$.

Methods Of Solving Contact Implicit Optimization Problems

Unfortunately, contact implicit trajectory optimization methods are notorious for being computationally complex. Therefore, methods are used to guide the optimizer towards feasible solutions [77]: penalty method [12, 14], and ϵ-relaxation methods [1, 10, 78]. These methods make MPCC optimization problems more computationally tractable.

The penalty method involves adding the sum of all the MPCCs as a scaled term in the objective function, removing it as a optimization constraint. Typically, the penalty applied to the complimentarity constraint is scaled at least two orders of magnitude above the the scalar value of the objective function [12, 14]. This makes the optimization problem appear more feasible to the optimizer.

To solve this MPCC problem, the optimizer has to find a locally optimal solution. The penalty method is applicable when solving an MPCC with a predictable solution. However, it introduces uncertainties when applied to less predictable problems describing transient dynamics. Adding additional terms to the objective function questions what is being optimized: is the resultant solution dynamically optimal, or is it solving the MPCCs accurately? Additionally, since these constraints are solved in the objective function, the optimizer does not need to satisfy them. This could result in the MPCCs not being feasibly solved [8].

ϵ-relaxation methods involve replacing the MPCC with an inequality constraint, and solving it below ϵ ($\alpha \cdot \beta = 0$ is replaced with $\alpha \cdot \beta \leq \epsilon$). In implementing this method, the problem is solved iteratively, with ϵ initialized high. After each feasible iteration,

Stellenbosch University https://scholar.sun.ac.za

the ϵ parameter is reduced by a factor of 10, relaxing the tolerance on the MPCC to a user-defined accuracy [8, 9, 78].

Manchester et. al. noted that ϵ-relaxation methods gives the optimizer freedom to apply a GRF at a non-zero distance from the contact surface, not truly satisfying the constraint. That was his motivation for employing the penalty method in his optimization problem. However, when ϵ is reduced to a sufficient accuracy, the MPCC is deemed feasibly solved. Fisher and Pretorius et. al. [8, 57] iteratively solve the MPCCs within an accuracy of $\epsilon \leq 1E-4$. This would apply a GRF when the distance between the foot and the contact surface is within the order of magnitude of 0.0001m. At this point the MPCC is deemed satisfied within the tolerance. Research presented in Chapter 4 suggests that this accuracy might be redundant, and that contact dynamics are accurately satisfied when $\epsilon \leq 1E-2$. In this thesis, the ϵ-relaxation methods were implemented as described in Chapter 3.

Stellenbosch University https://scholar.sun.ac.za

Chapter 3

Methodology

This thesis aimed to investigate how legged robots leverage contact events to translate their position in non-planar environments. Investigations were conducted by modeling legged robot systems in contact-implicit trajectory optimization environments. Thereafter, optimal trajectories resulting from these optimizations were analyzed.

Two robots were used as shown in Figure 3.1: a monopedal robot, and a bipedal robot with splayed hips. In this chapter, the development of both these models will be explained. However, in later chapters, the robot model relevant to the research will be stated.

This chapter aims to describe the dynamics of the system, and how they were integrated into the trajectory optimization environment. Section 3.1 will detail how the three-dimension (3D) Equations of Motion (EOM) were described using Euler-Lagrange Dynamics. Thereafter, Section 3.2 describes the development of the trajectory optimization models.

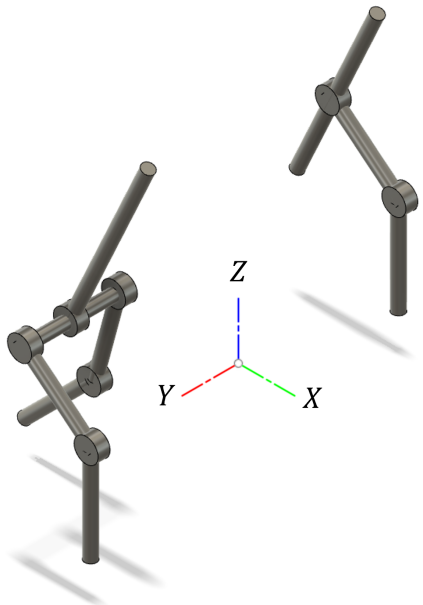

Figure 3.1: This image displays both 3D robots used in this investigation. Two robots were modeled: a monopedal robot, and a bipedal robot with splayed hips.

Stellenbosch University https://scholar.sun.ac.za

3.1. Dynamics

The robots described in this thesis were modeled as a set of rigid links. Each link had a unique mass, length, mass moment of inertia, and center of mass (COM). As shown in Figure 3.1, the monopod robot was modeled using a two-link leg joined at the center of a body link. Similarly, the bipedal robot was modeled using two two-link legs, separated by a hip link. The body of the biped robot protruded from the center of the hip link. Additionally, rotational torque actuators were used to model the joints between these links.

A set of generalized position, $\boldsymbol{q}$, velocity, $\dot{\boldsymbol{q}}$, and acceleration, $\ddot{\boldsymbol{q}}$, vectors were used to describe the minimal set of coordinates needed to define each respective robot. For the monopod robot, 8 DOFs were used to describe the generalized coordinates, such that $\boldsymbol{q} = \boldsymbol{q_{Monopod}}$. Similarly, the bipedal robot was described using 10 DOFs, such that $\boldsymbol{q} = \boldsymbol{q_{Biped}}$, with

$$\boldsymbol{q_{Monopod}} = \begin{bmatrix} x \\ y \\ z \\ \phi_{body} \\ \theta_{body} \\ \gamma_{body} \\ \boldsymbol{q}_{leg} \end{bmatrix}, \boldsymbol{q_{Biped}} = \begin{bmatrix} x \\ y \\ z \\ \phi_{body} \\ \theta_{body} \\ \gamma_{body} \\ \boldsymbol{q}_{leg_{left}} \\ \boldsymbol{q}_{leg_{right}} \end{bmatrix}, \tag{3.1}$$

where $\boldsymbol{q}_{leg}$ was,

$$\boldsymbol{q_{leg}} = \begin{bmatrix} \theta_{hip} \\ \theta_{knee} \end{bmatrix}. \tag{3.2}$$

Figure 3.2 provides a graphic representation of how these generalized coordinates described the respective robot. These generalized coordinates were used to compute the 3D Inertia Tensors, Potential Energy, and Kinetic Energy of each respective link. These energies and inertias were used to describe Euler-Lagrange Dynamics in the form of the Manipulator Equation, (3.21).

All angles referenced in this thesis were expressed relative to the inertial frame (absolute angles) [79]. Thus, reducing the computational complexity of the model by simplifying the equations of motion and improving the sparsity of the Coriolis term in (3.21) [14].

In this thesis, $\boldsymbol{\tau}$ represented single DOF motor torques applied to revolute joints, and $\boldsymbol{\lambda}$ represented the external ground reaction forces (GRF). For the monopod robot, motor torques were applied at the hip and the knee, and one GRF vector was modeled at the

Stellenbosch University https://scholar.sun.ac.za

foot:

$$\boldsymbol{\tau} = \begin{bmatrix} \tau_{hip} \\ \tau_{knee} \end{bmatrix}, \boldsymbol{\lambda} = \begin{bmatrix} \lambda_x \\ \lambda_y \\ \lambda_z \end{bmatrix}, \tag{3.3}$$

where τ_{hip} and τ_{knee} represented the applied motor torque at the hip and knee respectively. Whereas, λ_x and λ_y represented the horizontal component of the GRF, and λ_z represented the normal contact force. For the bipedal model motor torques were applied at the hip and knee; and a contact point was modeled for both legs of the robot:

$$\boldsymbol{\tau}_{Biped} = \begin{bmatrix} \boldsymbol{\tau}_{left} \\ \boldsymbol{\tau}_{right} \end{bmatrix}, \boldsymbol{\lambda}_{Biped} = \begin{bmatrix} \boldsymbol{\lambda}_{left} \\ \boldsymbol{\lambda}_{right} \end{bmatrix}. \tag{3.4}$$

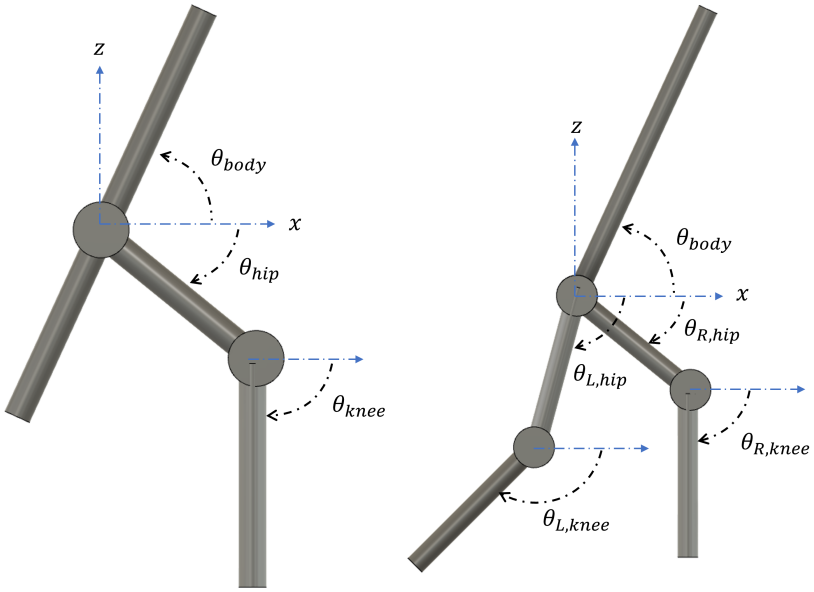

Figure 3.2: This image provides a graphic representation of how the generalized coordinates described the robots in this thesis. Absolute angles were used to describe the orientation of each link.

3.1.1. 3D Dynamics

Euler angles (roll around the x-axis, ϕ, pitch around the y-axis, θ, and yaw around the z-axis, ψ) were used to describe the attitude of the robots in 3D. These were used to calculate the position and velocities of each link's COM with respect to the global Cartesian axes. Thereafter, the kinetic and potential energy of the respective link was computed using these rotational coordinates. Additionally, these coordinates were appended to the generalized coordinates and used to describe the dynamics of the system.

Stellenbosch University https://scholar.sun.ac.za

Rotation Matrices

Rotation matrices were used to rotate the COM coordinates of each link around the Cartesian Axes and to define the attitude of the system. Euler's Rotation Theorem states that any rotation relative to an inertial plane can be described using three rotation angles [79]. Their respective rotations around the Cartesian Axes were described as:

$$\begin{aligned}
\mathbf{R}_x(\phi) &= \begin{bmatrix} 1 & 0 & 0 \\ 0 & cos(\phi) & -sin(\phi) \\ 0 & sin(\phi) & cos(\phi) \end{bmatrix}, \\
\mathbf{R}_y(\theta) &= \begin{bmatrix} cos(\theta) & 0 & sin(\theta) \\ 0 & 1 & 0 \\ -sin(\theta) & 0 & cos(\theta) \end{bmatrix}, \\
\mathbf{R}_y(\psi) &= \begin{bmatrix} cos(\psi) & -sin(\psi) & 0 \\ sin(\psi) & cos(\psi) & 0 \\ 0 & 0 & 1 \end{bmatrix}.
\end{aligned} \tag{3.5}$$

Here, $\mathbf{R}_x(\phi)$ represented the the roll rotation about the x axis, $\mathbf{R}_y(\theta)$, the pitch rotation about the y-axis, and $\mathbf{R}_z(\psi)$, the yaw rotation about the z-axis. The net rotation around the inertial plane was computed by multiplying of the rotation matrix for each respective Euler Angle, such that:

$$\mathbf{R}_{net}(\phi, \theta, \psi) = \mathbf{R}_y(\theta) \cdot \mathbf{R}_x(\phi) \cdot \mathbf{R}_z(\psi) \tag{3.6}$$

This specific rotation order was chosen to avoid the occurrence of gimbal lock [80]. Gimbal lock occurs when 2 sequential rotational DOFs align, ultimately, locking the system into a 2-DOF system. This occurs when the middle coordinate rotates 90° around its respective axis. In this implementation, the robot was constrained to roll within 45° to maintain an upright posture. Therefore, this specific rotation matrix order was chosen, with the roll coordinate in the middle, avoiding the occurrence of gimbal lock.

Center Of Mass

A vector was used to describe the position and attitude of the COM, $\mathbf{p}_{COM}$, of each link. Using the Jacobian (J) of the position of $\mathbf{p}_{COM}$, with respect to $\boldsymbol{q}$, the velocity of the COM, $\boldsymbol{v}_{COM}$ was computed,

$$\boldsymbol{v}_{COM} = \mathrm{J}(\mathbf{p}_{COM}, \boldsymbol{q}) \cdot \dot{\boldsymbol{q}}. \tag{3.7}$$

Stellenbosch University https://scholar.sun.ac.za

These vectors comprised of Cartesian elements and rotational elements to describe the position and attitude of the respective link:

$$\boldsymbol{p}_{linear} = \begin{bmatrix} x_{COM} \\ y_{COM} \\ z_{COM} \end{bmatrix}, \boldsymbol{p}_{rotational} = \begin{bmatrix} \phi_{COM} \\ \theta_{COM} \\ \psi_{COM} \end{bmatrix}, \tag{3.8}$$

$$\boldsymbol{v}_{linear} = \begin{bmatrix} v_{x_{COM}} \\ v_{y_{COM}} \\ v_{z_{COM}} \end{bmatrix}, \ \boldsymbol{v}_{rotational} = \begin{bmatrix} \omega_{\phi_{COM}} \\ \omega_{\theta_{COM}} \\ \omega_{\psi_{COM}} \end{bmatrix}, \tag{3.9}$$

$$\boldsymbol{p}_{COM} = \begin{bmatrix} \boldsymbol{p}_{linear} \\ \boldsymbol{p}_{rotational} \end{bmatrix}, \ \boldsymbol{v}_{COM} = \begin{bmatrix} \boldsymbol{v}_{linear} \\ \boldsymbol{v}_{rotational} \end{bmatrix}. \tag{3.10}$$

3.1.2. Kinetic And Potential Energy

The change in the energy of the system was used to describe the dynamics of the system. Therefore, the potential energy, V_{link}, and kinetic energy, T_{link}, of the each respective link was computed and summed together to compute the total energy of the system, such that:

$$V_{link} = m_{link} \cdot g \cdot \mathbf{p}_{COM_Z} \tag{3.11}$$

$$V_{Tot} = \sum_{link} V_{link} \tag{3.12}$$

where g represented the gravitational acceleration, m_{link} the mass, and $\mathbf{p}_{COM_Z}$ the vertical height, of the respective link's COM.

The kinetic energy, T_{link}, of each link was calculated and then summed to compute the kinetic energy of the system, T_{Total}. For each link the kinetic energy was split into two components T_{Linear} and $T_{Rotational}$, such that:

$$T_{link} = T_{Linear} + T_{Rotation} \tag{3.13}$$

$$T_{Tot} = \sum_{link} T_{link} \tag{3.14}$$

where, T_{Linear} described the translational energy decomposed into the Cartesian elements, as shown:

$$T_{Linear} = \frac{1}{2} \cdot \boldsymbol{m_{link}} \cdot \boldsymbol{v_{COM}} \cdot \boldsymbol{v_{COM}}^T \tag{3.15}$$

and $T_{Rotation}$ described the angular energy resulting from the rotation of the rigid body about the object's axis of rotation,

Stellenbosch University https://scholar.sun.ac.za

$$T_{Rotation} = \frac{1}{2} \cdot \boldsymbol{\omega_{COM}} \cdot \boldsymbol{I_{ToI}} \cdot \boldsymbol{\omega_{COM}}^{T}. \tag{3.16}$$

All links described in this research were modeled as 3D solid cylinders who's weight was evenly distributed between the Cartesian axes. This allowed a diagonal tensor of inertia to describe the distribution of the mass of the object, such that:

$$\boldsymbol{I_{ToI}} = \begin{bmatrix} I_{xx} & 0 & 0 \\ 0 & I_{yy} & 0 \\ 0 & 0 & I_{zz} \end{bmatrix}, \tag{3.17}$$

$$I_{xx} = \frac{1}{12} m_{link}(3r_{link}^2 + l_{link}^2), \tag{3.18}$$

$$I_{yy} = \frac{1}{12} m_{link}(3r_{link}^2 + l_{link}^2), \tag{3.19}$$

$$I_{zz} = \frac{1}{2} m_{link} r_{link}^2, \tag{3.20}$$

where I_{xx}, I_{yy}, and I_{zz}, where the moments of inertia around the x, y and z axis respectively. r_{link}, l_{link}, and m_{link} described the respective radius, length, and mass of each respective link.

All links had a radius of 2.5cm, mass of 0.75kg and a length of 0.2m. However, the parameters of the body links of both robots differed slightly. The body link of both robots had a radius of 2.5cm, an increased mass of 1.0kg and length of 0.4m.

3.1.3. Lagrange Dynamics - Manipulator Equation

Euler-Lagrange dynamics, in the form of the manipulator equation, were used to find the equations of motion of the robots described in this thesis:

$$\mathbf{M}(\boldsymbol{q})\ddot{\boldsymbol{q}} + \mathbf{C}(\boldsymbol{q}, \dot{\boldsymbol{q}})\dot{\boldsymbol{q}} + \mathbf{G}(\boldsymbol{q}) = \mathbf{B}\boldsymbol{\tau} + \mathbf{A}\boldsymbol{\lambda} \tag{3.21}$$

where $\mathbf{M}(\boldsymbol{q})$ was the inertia matrix for the whole system, $\mathbf{C}(\boldsymbol{q}, \dot{\boldsymbol{q}})$ described the Centrifugal Coriolis forces, and $\mathbf{G}(\boldsymbol{q})$ described the gravitational potentials. J described the jacobian matrix. Both $\mathbf{M}(\boldsymbol{q})$ and $\mathbf{C}(\boldsymbol{q}, \dot{\boldsymbol{q}})$ were functions of T_{Total}, and $\mathbf{G}(\boldsymbol{q})$ were dependent on V_{Total}. $\mathbf{M}(\boldsymbol{q})$ was computed as:

$$\mathbf{M}(\boldsymbol{q}) = J(J(T_{Tot}, \dot{\boldsymbol{q}}), \dot{\boldsymbol{q}}) \tag{3.22}$$

Stellenbosch University https://scholar.sun.ac.za

$\mathbf{C}(\boldsymbol{q}, \dot{\boldsymbol{q}})$ was computed element-wise to the i-th row and j-th column as:

$$C_{ij}(q, \dot{q}) = \frac{1}{2} \sum_{k=1}^{n} \left(\frac{\partial M_{ij}}{\partial q_k} + \frac{\partial M_{ik}}{\partial q_j} - \frac{\partial M_{kj}}{\partial q_i} \right) \tag{3.23}$$

Partial differentiation of the potential energy was used to populate the gravitational potential matrix,

$$\mathbf{G}(\boldsymbol{q}) = \frac{\partial}{\partial \boldsymbol{q}} (V_{Total}) \tag{3.24}$$

Algorithmically, this was implemented as:

Algorithm 3.1: Computing the Coriolis Matrix [8]

```
for i = 1 : length(q) do
    for j = 1 : length(q) do
        for m = 1 : length(q) do
            temp=0.5(diff(M(n,j),q(m)) + diff(M(n,m),q(j)) - diff(M(j,m),q(i)))q˙(m);
            C(n,j) = C(n,j)+ temp;
        end for
    end for
end for
```

Algorithm 3.2: Computing the Gravitational Potential Matrix [8]

```
for i = 1 : length(q) do
    G(i) = diff(Vtotal,q(i))
end for
```

Additionally, $\mathbf{A}$ and $\mathbf{B}$ mapped the external GRF, and internal motor torques, to the relevant generalized coordinates, $\boldsymbol{q}$. For the monopod, with only one contact point at the foot of the robot, $\mathbf{A}$ was calculated as the jacobian of the foot position with respect to the generalized coordinates:

$$\mathbf{A} = \sum_{foot} J(\mathbf{p}_{foot}(x, y, x), \boldsymbol{q}) \tag{3.25}$$

where $\mathbf{p}_{foot}$ represented the Cartesian position of the contact point. This method was duplicated for both contact points present in the bipedal model.

Since the joints were defined using absolute angles, relative to the inertial frame, applied torques had a positive effect on the lower link and a negative effect on the upper link. An auxiliary vector describing the coordinates that was affected by the applied torque was defined, $\mathbf{a}_{torque}$. The torque applied to knee joint of the monopod robot would rotate the lower leg link clockwise, increasing θ_{knee}, and the upper leg link anti-clockwise, decreasing θ_{hip}, such that $\mathbf{a}_{torque} = \begin{bmatrix} -\theta_{hip} \\ \theta_{knee} \end{bmatrix}$. Thereafter, $\mathbf{B}$ was calculated by taking the jacobian

Stellenbosch University https://scholar.sun.ac.za

of $\mathbf{a}_{torque}$ with respect to $\boldsymbol{q}$ and was summed across all applied torques present in the optimization.

$$\mathbf{B} = \sum_{torque} J(\mathbf{a}_{torque}, \boldsymbol{q}) \tag{3.26}$$

All linear algebra used to describe the dynamics were generated using Sympy [81]. These dynamics were interpreted as equality constraints to allow the trajectory optimization to find a feasible solution, satisfying all constraints.

3.2. Trajectory Optimization

The aim of this research was to gain insight into legged locomotion. This was achieved by analyzing feasible 3D trajectories that describe the dynamics of legged-robots conducting complex motions. These task were to be completed without having to explicitly plan for contact events and the related friction and slip phenomena. However, these motions are notorious for being computationally intractable, and inherently discontinuous.

Therefore, trajectory optimization methods were employed to plan new motions that interact with a contact rich environment with inelastic contact, friction, and slip, without having to specify contact conditions. This section describes how the trajectory optimization methods were implemented and used in this research.

3.2.1. Long-Time-Horizon Optimizations

Research on the monopedal robot was limited to smaller tasks and solved in a single optimization. However, long-time-horizon tasks were conducted using the bipedal robot. This required the robot start, and end, at rest after completing multiple steps. These motions are highly complex, and resulted in large and computationally intractable optimizations.

Fisher et. al. [1, 8] suggested that long-time-horizon trajectories could be split into multiple smaller tasks and later stitched together. Task specific, and more computationally tractable, trajectories were solved and later stitched, as shown in Figure 3.3. Chapter 5 presents the acceleration, deceleration, and steady-state trajectories. Whereas the rapid turn trajectories are presented in Chapter 6.

Additionally, contact was not enforced. Contact orders for rapid acceleration, deceleration, and turn motions are not yet fully understood. Therefore, contact-implicit trajectory

Stellenbosch University https://scholar.sun.ac.za

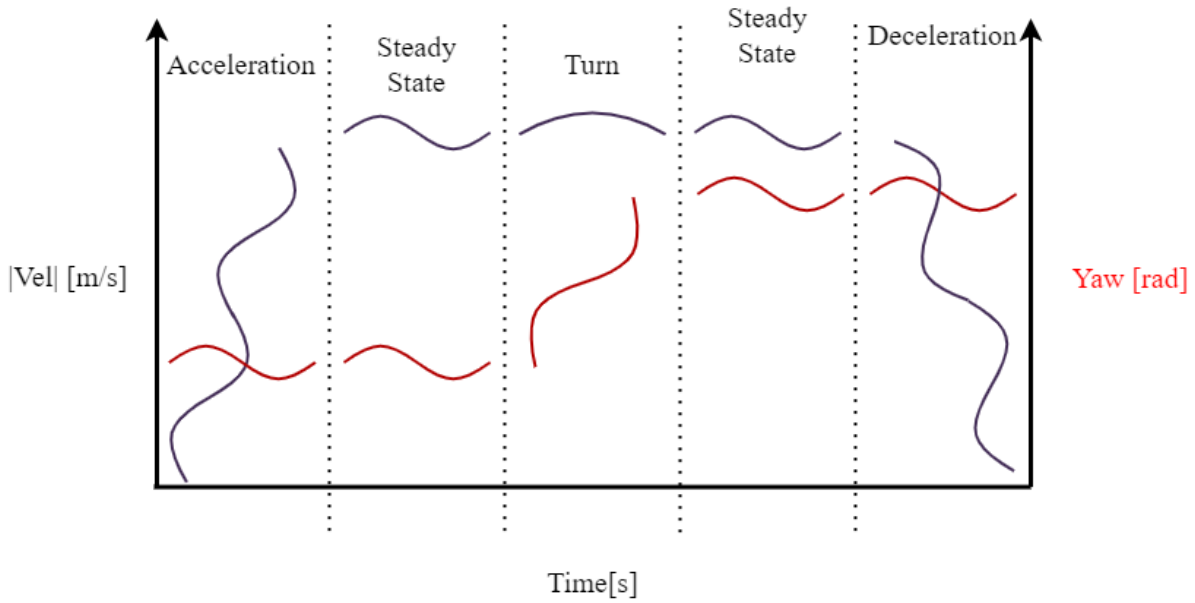

Figure 3.3: This figure displays how the long-time-horizon trajectory was split into multiple smaller trajectories, and then stitched together.

optimization methods were implemented to allow for optimal contact-orders to be found by the optimizer. However, for periodic steady-state trajectories, contact orders can be predicted. Contact events were only allowed for parts of the steady-state trajectories, and not enforced.

All trajectory optimizations presented in this thesis were completed using the Pyomo modeling package, in Python, using the IP-OPT solver [82–85]. Many trajectory optimization experiments were conducted in this research. Constraints and variable bounds were used to guide the trajectory towards feasible and optimal solutions. These constraints and bounds are further detailed in the subsequent chapters that describe the research conducted.

3.2.2. Collocation And Discretization

All trajectories presented in this research were discretized into N discrete time-steps, integrated using third order polynomials. This resulted in trajectories being divided into N node points ($n \in [1, N]$), with 3 collocation points separating each node ($j \in [1, 3]$). N ranged between 50 and 150 nodes depending on the task needed to complete. However, for all trajectories, three collocation points were used to join node points on a Runge-Kutta basis and three-point Radau techniques were used to solve the differential equations [9, 86]. This allowed for an accuracy of $O(h) = h^{2K-1}$, where h was the duration of the timestep, and K the order of the polynomials, $K = 3$.

Stellenbosch University https://scholar.sun.ac.za

Three-point Radau was implemented to integrate the equations of motion between the discrete node points using (3.27), (3.28) and a three-point collocation matrix $\mathbf{a}$, (3.31). Whereas, (3.29) and (3.30) locked the third collocation point of the state vector, $\boldsymbol{q}[n,3]$, and state velocities, $\dot{\boldsymbol{q}}[n,3]$, onto the beginning of the next time-step's position and velocity, $\boldsymbol{q}_0[(n+1)]$ and $\dot{\boldsymbol{q}}_0[(n+1)]$, to ensure continuous trajectories:

$$\boldsymbol{q}[n,j] = \boldsymbol{q}_0[n] + h[n]\sum_{k=1}^{3}\mathbf{a}_{kj}\dot{\boldsymbol{q}}[n,k], \tag{3.27}$$

$$\dot{\boldsymbol{q}}[n,j] = \dot{\boldsymbol{q}}_0[n] + h[n]\sum_{k=1}^{3}\mathbf{a}_{kj}\ddot{\boldsymbol{q}}[n,k], \tag{3.28}$$

$$\boldsymbol{q}_0[n] = \boldsymbol{q}[(n-1),3], \tag{3.29}$$

$$\dot{\boldsymbol{q}}_0[n] = \dot{\boldsymbol{q}}[(n-1),3], \tag{3.30}$$

$$\mathbf{a} = \begin{bmatrix} 0.19681547722366 & 0.39442431473909 & 0.37640306270047 \\ -0.06553542585020 & 0.29207341166523 & 0.51248582618842 \\ 0.02377097434822 & -0.04154875212600 & 0.11111111111111 \end{bmatrix}. \tag{3.31}$$

Orthogonal collocation required that contact occurred at the beginning of the discrete time-step, and not between discrete time-steps. Therefore, a variable time-step was employed to provide flexibility to the duration of the time-steps. The duration of each discrete element was constrained to vary according to (3.32). This allowed contact to occur at the beginning of each discrete time-step. Additionally, this increased the resolution during periods of high non-linearity, and decreased the resolution when the trajectory could easily be accurately described using the third-order integration splines:

$$\begin{aligned} 0.1h_M \leq h[n] &\leq 2h_M, \\ tt[n,j] &= tt_0[n] + h[n]\sum_{k=1}^{3}\mathbf{a}_{kj}, \\ tt_0[n] &= tt[(n-1),3]. \end{aligned} \tag{3.32}$$

Here, $h[n]$ was the duration of the n-th node, such that $n \in [1,N]$, and $h_M = \frac{T}{N}$ described a ratio between an estimated time needed for the optimizer to complete its tasks, T, and N. $tt[n,j]$ represented the duration of time from the start of the optimization to the n-th node, and j-th collocation point. Whereas, $tt_0[n]$ was used to lock the time value of the third collocation point of the previous node to the time value of the current node point.

Not all decision variables presented in this thesis were integrated using third-order collocation schemes. For ease of notation, variables described using third order integration

Stellenbosch University https://scholar.sun.ac.za

methods are displayed without an index. Unless otherwise stated, all references to un-indexed decision variables were discretized to the n-th node point, and j-th collocation point. For example, $\boldsymbol{q}[n,j] = \boldsymbol{q}$, referred to the set of state vectors discretized to both the node point, and collocation point. Whereas, $\boldsymbol{\tau}[n]$ referred to the motor torque discretized to the n-th discrete node only.

Unless otherwise stated, all decision variables were functions of $\boldsymbol{q}$, and $\dot{\boldsymbol{q}}$. For additional ease of notation, indications this dependence will be suppressed. As an example, the Manipulator Equation, (3.21), could be displayed as:

$$\mathbf{M} + \mathbf{C} + \mathbf{G} = \mathbf{B}\boldsymbol{\tau} + \mathbf{A}\boldsymbol{\lambda}. \tag{3.33}$$

3.2.3. Cost Function

As discussed in Chapter 2, general consensus has not yet been reached on accepted cost functions for transient motions. Therefore, energy and time based cost functions were used interchangeably throughout this research:

$$\begin{aligned} J_{time} &= \sum_{n=1}^{N} h[n], \\ J_{torque} &= \sum_{n=1}^{N} \tau[n]^2 h[n], \\ J_{initialize} &= 1.0, \end{aligned} \tag{3.34}$$

where J_{time} described a minimum time cost function, J_{torque} described a torque cost function scaled by the duration of the applied torque and a scalar cost function function, $J_{initialize}$.

$J_{initialize}$ was used to warm start the solver, allowing the solver to find a feasible, but not optimal starting point. Thereafter, the objective was set to J_{time}. This guided the optimization towards time-sensitive minima for the rapid tasks. J_{torque} was used to smooth out the time-sensitive trajectories[1].

3.2.4. Initial And Final Conditions

Initial and final conditions were chosen task dependently. These conditions are explicitly stated for each experiment conducted in this thesis. When specific initial conditions were

[1] This is further explained in Section 3.2.6.

Stellenbosch University https://scholar.sun.ac.za

chosen, they were set using bounds. Similarly, final conditions were forced to the desired value using equality constraints.

All trajectories were set to start at the apex of a hop, at the center of the Cartesian Plane (with the exception of the acceleration trajectories, which were set to start in the rest position). This was enforced by setting, $x_0[1] = 0.0, y_0[1] = 0.0$, $\dot{z}_0[1] = 0.0$, and $\ddot{z}[1,1] = -9.81$. However, the rest position of the biped, $\boldsymbol{q}_{rest}$, was defined such that all links were vertically stacked, and at rest, as shown in Figure 3.4.

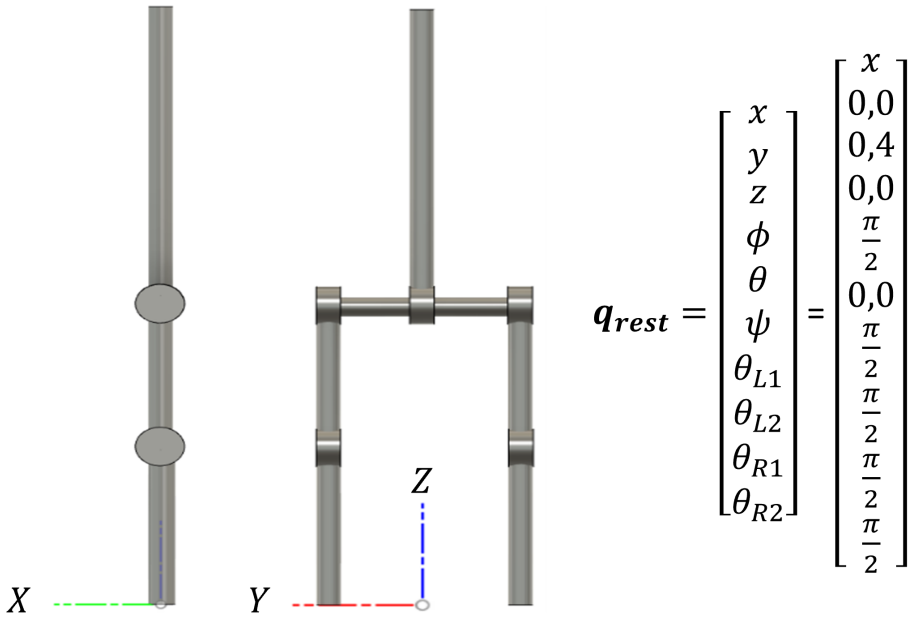

Figure 3.4: This image shows the rest position of the bipedal robot. All links were vertically stacked, and at rest.

3.2.5. Constraints

Complimentarity Constraints

MPCCs were used to apply the contact implicit optimization techniques ($\alpha\beta = 0$). However, finding feasible solutions to these problems are notorious for being computationally intractable. Therefore, ϵ-relaxation schemes were applied to improve the convergence rate of the experiments. These methods frame MPCCs as inequality constraints with an upper bound:

$$\alpha\beta \leq \epsilon, \tag{3.35}$$

Stellenbosch University https://scholar.sun.ac.za

where α and β were two positively bounded variables making up the MPCC, and ϵ was a relaxation parameter. Initially, ϵ was set to 1000, and the optimization was solved iteratively. ϵ was reduced with each iteration, until a desired accuracy was achieved. Each successful solve was used to seed the following optimization, with ϵ reducing by a factor of 10. After 8 feasible solutions were found, and ϵ was squeezed to $1E-4$, the MPCCs were deemed solved and the solution was saved[2]. Once successfully solved, the MPCC was squeezed sufficiently close to zero as shown in Figure 3.5 [1, 9, 12, 78].

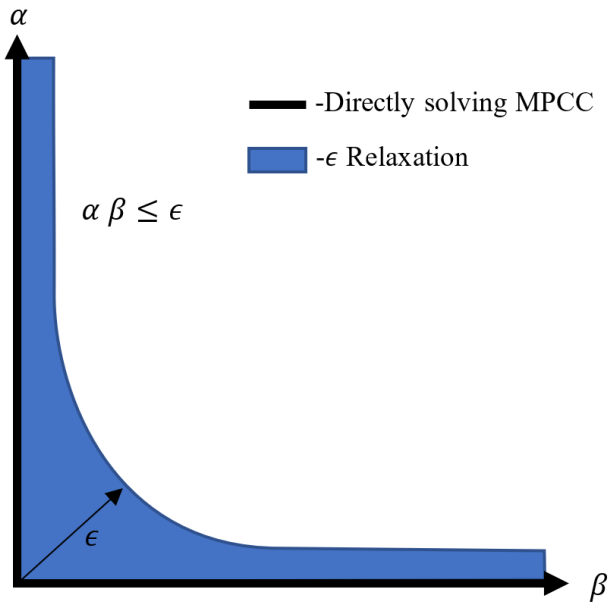

Figure 3.5: This image displays the difference between directly solving the MPCCs, compared to relaxing them using ϵ-relaxation schemes [12]. It is seen that as ϵ reduces, the relaxed solution of the MPCC gets solved closer to the direct solution.

To further aid the optimizer in finding feasible solutions, MPCCs were summed across collocation points and only computed at discrete time-steps. This kept contact modes constant throughout the discrete time-step, allowing higher order splines to describe the dynamics, while maintaining the amount of MPCCs in the problem [9, 87]. The following slack variables were introduced in implementing the MPCCs:

$$\begin{aligned} \alpha[n,j] \geq 0, \quad & \alpha'[n] = \sum_{j=0}^{K} \alpha[n,j], \\ \beta[n,j] \geq 0, \quad & \beta'[n] = \sum_{j=0}^{K} \beta[n,j], \\ & \alpha'[n]\beta'[n] \leq \epsilon. \end{aligned} \tag{3.36}$$

Here, $\alpha[n,j]$ and $\beta[n,j]$ described the MPCC variables at the n-th discrete time-step, and j-th collocation point. Slack variables, $\alpha'[n]$ and $\beta'[n]$, were the respective sum of $\alpha[n,j]$

[2]Section 3.2.6 provides a comprehensive description of how the ϵ-relaxation schemes were applied.

Stellenbosch University https://scholar.sun.ac.za

and $\beta[n, j]$ across the collocation points. And, the MPCC was applied to $\alpha'[n]$ and $\beta'[n]$. This ensured that the MPCC was only computed once per discrete time-step, and that the state of contact was constant throughout the duration of the time-step. Thus, increasing the resolution of the system dynamics while maintaining the amount of MPCCs in the problem.

Contact Implicit Trajectory Optimization

Contact-implicit trajectory optimization schemes allowed the optimizer freedom to make and break contact events, and find optimal gaits for the respective tasks. This was done by modeling inelastic contact events, the resultant friction, and slip, as a set of MPCCs. These techniques have shown to aid in the development of rapid locomotion.

Extenal GRFs were modeled as $\boldsymbol{\lambda}$, and comprised of a vertical, and horizonal component, $\boldsymbol{\lambda} = [\lambda_z, \boldsymbol{\lambda}_{\parallel}]$. An inelastic ground contact constraint was used to apply the vertical GRF, λ_z. Whereas, a set of friction constraints were used to apply the tangential GRFs, $\boldsymbol{\lambda}_{\parallel}$. In 3D environments, friction forces were made up of Cartesian components, such that $\boldsymbol{\lambda}_{\parallel} = [\lambda_x, \lambda_y]$. These constraints are described below:

- **Inelastic Hard Contact**

  A gap function, ρ, described the distance between the contact point and the contact surface [10–12, 64, 75][3]. Inelastic contact was modeled in this research, positively bounding the gap function, $\rho \geq 0$, and modeled as a MPCC, shown in (3.37). This MPCC allowed the optimizer to apply a GRF one discrete element prior to the foot making contact with the ground, shown in Figure 3.6. Thus, reducing the impulsive GRF, and smoothing out the discontinuous dynamics. This constraint, with additional friction constraints were applied to each contact point.

$$\begin{aligned} \rho[n] &\geq 0, \\ \lambda_z[n] &\geq 0, \\ \rho[n+1] \cdot \lambda_z[n] &\leq \epsilon. \end{aligned} \tag{3.37}$$

- **Modeling Friction**

  Contact models used to describe the frictional effects of ground contact are described in depth in Chapter 4. These contact models made use of the hard contact MPCC described above.

[3] In previous literature, this gap function is represented as ϕ [9, 10, 12]. However, this conflicts with the notation describing the roll attitude angle, ϕ_{body}, described in Section 3.21.

Stellenbosch University https://scholar.sun.ac.za

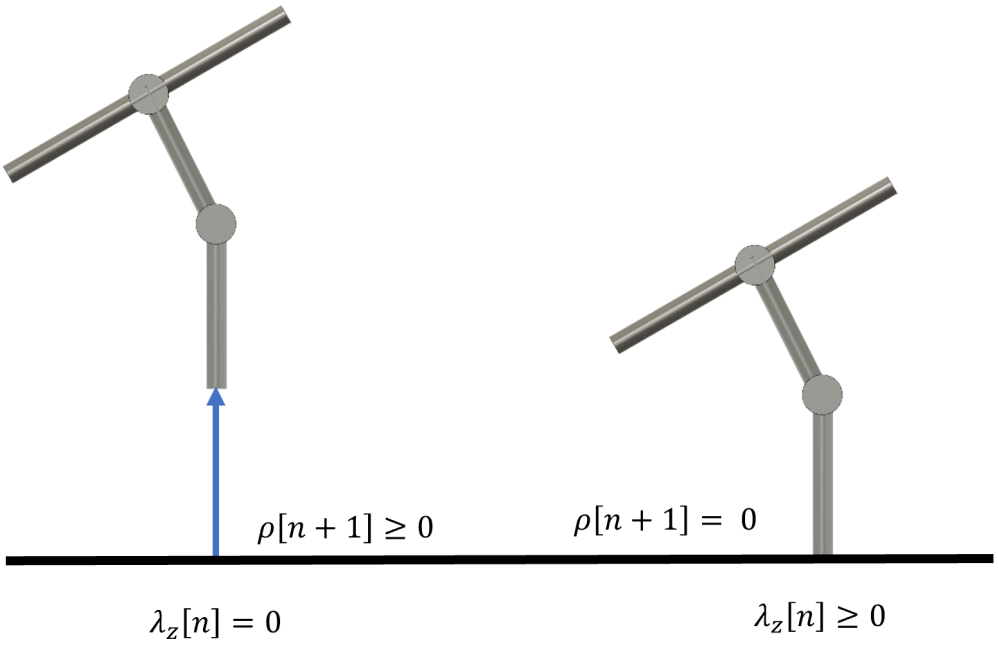

Figure 3.6: This image displays how the inelasstic hard contact MPCC works. On the left, where the robot has not made contact with the surface, the MPCC is satisfied by setting $\lambda_z = 0$. When contact is made, as seen on the right, the MPCC is satisfied by setting $\rho = 0$.

Motor Model

A linear speed-torque motor model was implemented to motivate the applicability of the trajectories on real world robots. Implementing a motor model makes the trajectory results physically realizable [8, 49]. The parameters used in this model were based on the T-Motor AK10-9 Motor [88]. This motor was chosen for its high torque limit, $\tau_{max} = 54\text{Nm}$, and angular speed limit, $\omega_{max} = 47.1\text{rad/s}$. The magnitude of these parameters were necessary to provide the actuators enough torque and angular speed to conduct the rapid motions investigated in this thesis.

Additionally, the torque actuators were integrated between the discrete node points using linear integrators. Therefore, they remained constant throughout the discrete time-step. This was implemented to avoid artificial oscillations in the motor torque signal which increases the sparcity of the optimization problem [9, 89, 90].

A set of constraints, as shown in (3.38), were used to implement the motor model in the optimization:

$$-\tau_{max} - \frac{\tau_{max}}{\omega_{max}}\omega[n] \leq \tau[n] \leq \tau_{max} - \frac{\tau_{max}}{\omega_{max}}\omega[n] \tag{3.38}$$

Stellenbosch University https://scholar.sun.ac.za

Here, τ_{max} and ω_{max} described the stall torque and no-load velocity of the motor. $\omega[n]$ and $\tau[n]$ described the relative angular speed of, and the torque applied to, the respective joint at the n-th discrete time-step [48, 49].

Time Upper Bound

When $\epsilon \leq 1.0$, the objective switched from a minimum time objective to a minimum torque objective[4]. To enforce this time-sensitivity in the trajectories while searching for torque based local minima, an upper bound constraint was used to describe the maximum time allowed for the robot to complete its task. This constraint was only activated when $\epsilon \leq 1.0$, and was implemeneted as:

$$\sum_{n=1}^{N} h[n] \leq 2.0 * T_{max}, \tag{3.39}$$

where T_{max} was the duration of the the previous iteration of the solve process. This allowed the optimizer to find torque based local minima, where the duration of the solved trajectory was less than double the duration of the previous iteration.

3.2.6. Solver Setup

All optimizations were solved iteratively using ϵ-relaxation techniques. Solutions to the previous optimizations were used to seed the next iteration of the solve process. Seeds that solved to infeasible local minima were discarded, and the optimization process was restarted. Employing this technique warm started the optimization using feasible initialization points to seed the optimizations and iteratevely solved the complimentarity constraints below ϵ [4, 8, 70].

For the first iteration ϵ was set to 1000, and the objective function set to J_{scalar}, allowing the optimizer to satisfy all constraints without having to optimize a cost function. This allowed for the solver to be seeded with a feasible set of initial decision variables. Thereafter, the objective was set to a minimum time cost function, J_{time}, and ϵ was reduced by a factor of 10 for each iteration of the solve process. However, it was noticed that the minimum time cost function guided the solution towards deep local minima producing erratic and jerky trajectories that violated the motor model. Therefore, once $\epsilon = 1.0$, the objective was changed to a minimum torque objective, J_{torque}, to smooth the trajectories and find more torque sensitive solutions. After 8 successful iterations, and $\epsilon = 1E-4$, all

[4]This is further described in Section 3.2.6.

Stellenbosch University https://scholar.sun.ac.za

complimentarity constraints were considered solved within acceptable tolerances.

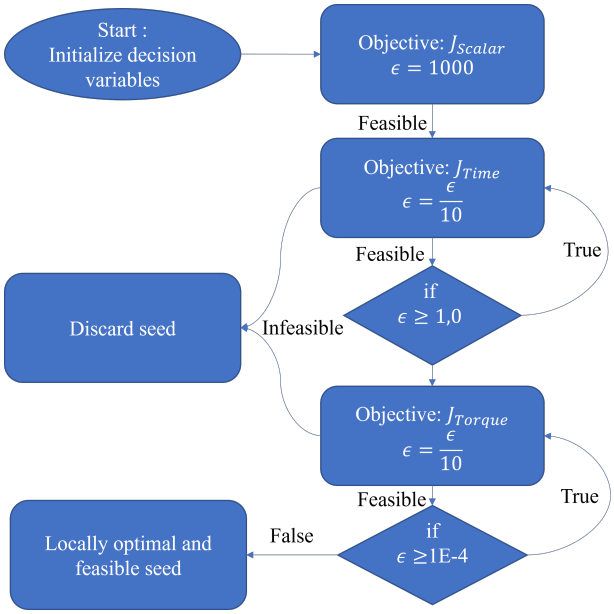

Figure 3.7: Flow diagram of the iterative process used to find feasible solutions to the trajectory optimization. ϵ-relaxation schemes resulted in the 8 iterative solve processes, each time decreasing ϵ by a factor of 10. Any seed resulting in an infeasible, or corrupt, solution was discarded.

3.2.7. Bounds

Variable bounds were chosen to restrict the search space, without ruling out non-intuitive solutions. Decision variables were varied between these bounds to find optimal trajectories.

All external GRFs were positively, and negatively, bound less than 10 times the weight of the robot, $\boldsymbol{\lambda} \in (-10mg, 10mg)$, where m was the mass of the robot, and $g = 9.81m/s^2$, the gravitational constant. Whereas, the vertical component of the GRF was positively bound, such that $\lambda_z \in (0.0, 10mg)$. This stopped the optimizer applying unrealistic GRFs onto the robot. Excessive external forces applied to the robot could lead to mechanical failure.

Complimentarity constraints were solved using positively bounded slack variables, $\mathbf{slack}[n] = \{\alpha'[n], \beta'[n]\}$. These slack variables were bound sufficiently high to not restrict the optmization search space, $\alpha'[n] \in (0.0, 1000.0)$ and $\beta'[n] \in (0.0, 1000.0)$.

Cartesian Coordinates were bound within 2m from the orgin, such that $x[n] \in (-2.0\text{m}, 2.0\text{m})$, $y[n] \in (-2.0\text{m}, 2.0\text{m})$, and $z[n] \in (0.0\text{m}, 2.0\text{m})$. Similarly, Euler angles were bound to ensure forward, and upright orientation of the robot, such that $\phi_{body}[n] \in (-45°, 45°), \theta_{body}[n] \in (0.0°, 180°), \psi_{body}[n] \in (-90°, 90°)$. Note that the bounds on the orientation exclude the occurrence of gimbal-lock in the rotation matrices [80].

Stellenbosch University https://scholar.sun.ac.za

Absolute angles, relative to the inertial axes, were used to describe all joints. This reduced the computational complexity of the model by improving the sparcity of the Coriolis term in the Manipulator Equation, (3.21), and simplified the EOMs [14]. Joint angles were bound using a set of constraints to restrict the motion of the respective joint. For the two-link leg, the following constraints were applied:

$$\begin{aligned} \text{lower bound} \leq \theta_{hip} \leq \text{upper bound}, \\ \text{lower bound} \leq \theta_{knee} - \theta_{hip} \leq \text{upper bound}, \end{aligned} \tag{3.40}$$

where, the lower bound of the joint angles was defined by the y-axis (0°), and the upper bound was 135° from the y-axis. On the bipedal robot, the constraints applied to the hip, and knee angle, $\boldsymbol{q}_{leg}$, were duplicated on both the left and right leg.

3.2.8. Variable Initialization

Highly discontinuous trajectories were used to describe the dynamics, contact events, resultant friction, and slip. This modeling complexity was computationally intractable, and the optimization often got stuck in deep local minima, making it tough for the optimization to find optimal and feasible solutions.

Therefore, the state variables and its derivatives were seeded with a random seed that varied between the bounds of the specific variable. Whereas all other variables were fixed to 0.01 [4, 26]. This warm started the optimizer, improving the rate of convergence and allowing the multiple optimizations done in this research to comprehensively search the solution space. Consequently, varying the optimizations conducted in the research with the random seeds allowed for wider searching of the solution space for unintuitive solutions.

3.2.9. Decision Variables

The methods described in this Chapter are dependent on a large amount of variables passed to the optimizer. Solutions to these optimization problems are found by varying a set of decision variables between their respective bounds until a set of decision variables are found which satisfies all the constraints applied to it. The decision variables used to model the optimization problem described in this Chapter are shown:

$$\boldsymbol{decVar} = [\boldsymbol{q}[n,j]; \dot{\boldsymbol{q}}[n,j]; \ddot{\boldsymbol{q}}[n,j]; tt[n,j]; \boldsymbol{q_0}[n]; \dot{\boldsymbol{q}}_{\boldsymbol{0}}[n]; tt_0[n]; \boldsymbol{\tau}[n]; \boldsymbol{\lambda}[n]; \mathbf{slack}[n]] \tag{3.41}$$

The decision variables consists of the higher order collocation position state vector,

Stellenbosch University https://scholar.sun.ac.za

$\boldsymbol{q}[n,j]$, its velocity, $\dot{\boldsymbol{q}}[n,j]$, acceleration derivatives, $\ddot{\boldsymbol{q}}[n,j]$ and time, $tt[n,j]$. These higher order state and time vectors described the dynamics to the n-th discrete time step, and j-th collocation point. Position, $\boldsymbol{q_0}[n]$ velocity, $\dot{\boldsymbol{q}}_{\mathbf{0}}[n]$, and time, $tt_0[n]$, vectors describing the mechanics at the discrete time-steps were also included. Input motor torques, $\boldsymbol{\tau}[n]$, external GRFs $\boldsymbol{\lambda}[n]$, and complimentarity slack variables, **slack**[n], completed the set of decision variables.

Stellenbosch University https://scholar.sun.ac.za

Chapter 4

Methods Of Modeling 3D Friction Using MPCCs

Capturing the nuances of bipedal locomotion is an intractable task [2, 3]. It involves multiple legs leveraging the effects of contact to translate a body in space. Additionally, roboticists are yet to fully understand how contact works, let alone how to leverage them. Therefore, this investigation was prefaced by studying directional monopod hopping with a singular contact point. This simplified the investigation, and provided relevant background understanding of how contact events are leveraged in legged locomotion.

These studies were conducted using contact implicit trajectory optimization schemes to study the discontinuous mechanics inherent to legged locomotion. However, previous attempts at modeling contact events using MPCCs were often limited to planar models due to the computational complexities of modeling the 3D friction cone [4, 8]. Additionally, current methods of modeling the 3D friction cone are notorious for being computationally inefficient, and inaccurate under slip conditions [13]. In this chapter, we aim to address these limitations and accurately model contact events in non-planar environments.

Modeling the friction cone using MPCCs require that it be linearized. Traditionally, the 3D friction cone is linearized by replacing it with an inner-polyhedral approximation, who's edges define the friction cone. Solutions are then found along the edges of this approximation. When the direction of motion of the contact point aligns with the edges of the this approximation, as in planar motion, this approximation is accurate. However, when the direction of motion lies between the axis that define the friction cone, a kinematically feasible under-approximation is made.

This chapter aims to present an alternative approach of sampling the 3D friction cone by efficiently finding solutions along the vector that satisfies the Maximum Dissipation Principle. On a surface with a uniformed coefficient of friction, solutions are found along the vector that opposes the relative velocity at contact. Thus, reducing the amount of MPCCs needed to model the 3D friction cone [57].

Stellenbosch University https://scholar.sun.ac.za

Additionally, within robotics literature contact implicit trajectory optimization experiments are typically solved within $\epsilon \leq 1E-4$ [1, 8]. The default tolerance for the IP-OPT solver is $10E-8$ [91]. In the following experiments, this tolerance was set to $1E-6$. We hypothesized that once a solution is found, with ϵ less than two orders magnitude of μ the friction cone is solved within 1% an acceptable tolerance. Additionally, the solutions for the following optimizations will converge deeper within the local minima. This makes solutions for smaller ϵ parameters redundant.

Trajectory optimization experiments were conducted implementing the proposed contact model, and the contact model implementing the polyhedral approximation, of the friction cone on a monopod robot. This experiment included a monopedal robot interacting with a non-planar environment trying to achieve the following aims:

- Conduct monopedal hops with clear contact dynamics, under slip pery ($\mu = 0.2$), and sticky conditions ($\mu = 1.0$). Additionally, during these experiments, the direction of motion was constrained between the Cartesian Axes.
- Analyze the feasible solutions for different ϵ values to identify emerging trends.

These results show significant improvements in accuracy of the novel method presented. Thus, motivating the use of the presented method to make studying non-planar legged locomotion in trajectory optimization more accessible.

4.1. Methods Of Modeling Friction

This section will describe the contact models used to implement each respective method of modeling friction used in this chapter. The hard contact complimentarity constraint accurately modeled the vertical GRF, λ_z. Whereas, the methods of modeling friction described below aimed to compute $\boldsymbol{\lambda}_{\|}$. These contact models formed part of the contact-implicit trajectory optimization methods described in Section 3.2.5, and followed after the hard contact complimentarity, (3.37), displayed again for convenience,

$$\rho[n+1] \cdot \lambda_z[n] \leq \epsilon. \tag{4.1}$$

Here, ρ described a positively bounded gap function describing the distance between the point of contact, and the contact surface, and λ_z described the vertical component of the GRF. As explained in Section 3.2.5, the hard contact MPCC allowed the optimizer to apply the GRF one discrete element prior to contact being made.

Stellenbosch University https://scholar.sun.ac.za

4.1.1. Polyhedral Approximation Of The Friction Cone

In this method, the friction cone was replaced with a polyhedral approximation of the friction cone, whose edges were defined by unit vectors $\mathbf{D}^k$, for $k \in [1, d]$. Thereafter, the applied friction force was summed across $\mathbf{D}$, such that: $|\boldsymbol{\lambda}_{\|}| = \sum_{k=0}^{d} \mathbf{D}^k \lambda^k$, where λ^k represented the magnitude of the applied friction in the k direction [10, 75]. MPCCs were applied along the edges of the polyhedral approximation, to satisfy Coulomb's law:

$$|\boldsymbol{\lambda}_{\|}| \leq \mu \lambda_z. \tag{4.2}$$

All references to the polyhedral approximation of the friction cone in this thesis was modeled as a four-sided friction pyramid, such that $d = 4$, shown in Figure 4.1. This implementation is commonly found in literature, and allows the edges of the pyramid to be defined by the Cartesian Axes [11–13, 71, 92].

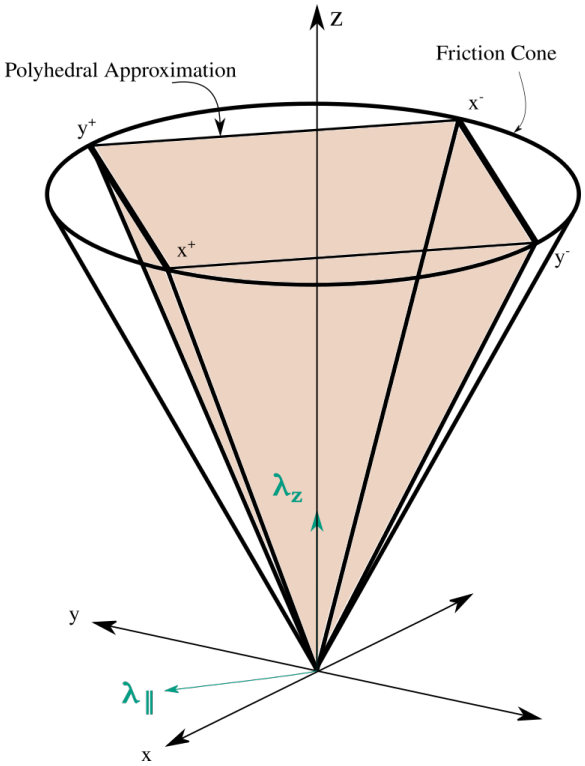

Figure 4.1: This figure displays the four-sided friction pyramid implemented in this experiment. Here, the positive and negative directions of the Cartesian Axes defined the edges of the pyramid.

Therefore, $\mathbf{D}$ described vectors along both the positive and negative components of the x and y axis, such that $\mathbf{D} = [x^+, x^-, y^+, y^-]^T$. The horizontal components of the GRF

Stellenbosch University https://scholar.sun.ac.za

were split into the positive and negative components and implemented as follows:

$$\lambda_x^+, \lambda_x^-, \lambda_y^+, \lambda_y^-, \text{ and } \lambda_z \geq 0 \tag{4.3}$$

$$\boldsymbol{\lambda} = \begin{bmatrix} \lambda_x^+ - \lambda_x^- \\ \lambda_y^+ - \lambda_y^- \\ \lambda_z \end{bmatrix}. \tag{4.4}$$

MPCCs applied to the edges of the pyramid satisfied Coulomb's Law:

$$\begin{aligned} \mu\lambda_z - \lambda_x^+ - \lambda_x^- - \lambda_y^+ - \lambda_y^- \geq 0, \text{ and } \gamma \geq 0, \\ (\mu\lambda_z - \lambda_x^+ - \lambda_x^- - \lambda_y^+ - \lambda_y^-) \cdot \gamma \leq \epsilon. \end{aligned} \tag{4.5}$$

Additional MPCCs, along the edges of the pyramid, were applied to compute the direction of slip [10–12, 64, 75]:

$$\begin{aligned} (\gamma + \boldsymbol{\psi}) \geq 0, \text{ and } (\gamma - \boldsymbol{\psi}) \geq 0, \\ (\gamma + \psi_x) \cdot \lambda_x^+ \leq \epsilon, \\ (\gamma - \psi_x) \cdot \lambda_x^- \leq \epsilon, \\ (\gamma + \psi_y) \cdot \lambda_y^+ \leq \epsilon, \\ (\gamma - \psi_y) \cdot \lambda_y^- \leq \epsilon. \end{aligned} \tag{4.6}$$

Here, γ was the magnitude of the tangential foot velocity at contact and ψ represented the tangential foot velocity vector (i.e. γ represented the speed, and ψ represented the velocity, of the relative velocity at contact). In (4.5), the optimizer was allowed to apply friction until the sum of the friction across the edges of the optimization equaled the vertical component of the GRF scaled by the coefficient of friction, μ. Thereafter, slip was allowed to occur in a direction direction satisfying (4.6).

4.1.2. Novel Method Of Modeling 3D Friction Cone

In this thesis, a novel method of linearizing the 3D friction cone as a set of complimentarity constraints is presented, which can be found at [57]. The proposed method uses the Maximum Dissipation Principle's dependence on relative velocity to determine the direction of the resultant friction, as shown in Figure 4.2. Therefore, the method is dependent on the tangential component of the GRF, $\boldsymbol{\lambda}_{\parallel} = [\lambda_x, \lambda_y]^T$, and relative tangential velocity at contact $\boldsymbol{v}_{rel} = [v_x, v_y]^T$. These Cartesian vectors were interpreted in polar form as:

$$\begin{aligned} \boldsymbol{\lambda}_{\parallel} &= |\boldsymbol{\lambda}_{\parallel}| \angle \Theta, \\ \boldsymbol{v}_{rel} &= |\boldsymbol{v}_{rel}| \angle (\Theta - 180^\circ), \end{aligned} \tag{4.7}$$

Stellenbosch University https://scholar.sun.ac.za

where the angle of the resultant friction taken from the x axis was represented by Θ. Consequently, Θ was locked to oppose the direction of $\boldsymbol{v_{rel}}$ [63, 64, 93].

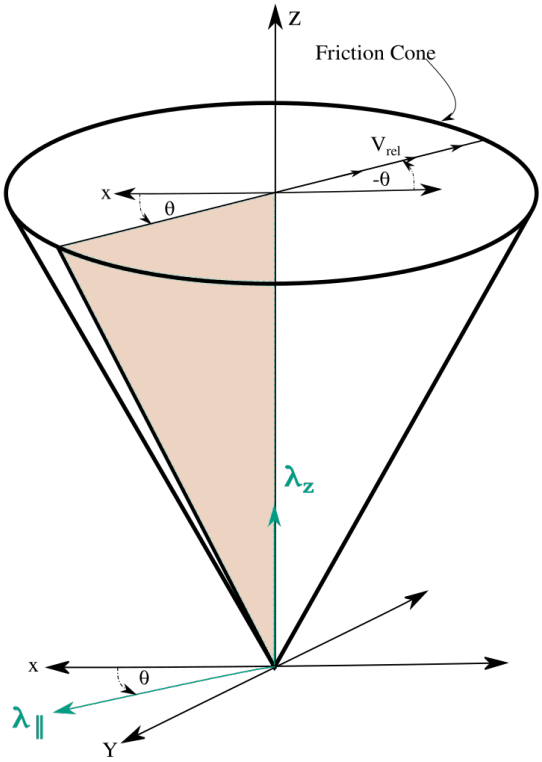

Figure 4.2: This figure displays the proposed method of modeling the 3D friction cone. Here, the friction cone is defined along the direction that satisfies the Maximum Dissipation Principle.

Once (4.1) has determined if a contact event occurred, Coulomb's law is satisfied using the following constraint:

$$|\boldsymbol{v}_{rel}|(\mu\lambda_z - |\lambda_{\|}|) = 0. \tag{4.8}$$

This constrained slip to only occur when the magnitude of the friction force equaled the vertical component of the GRF, scaled by μ. In these events, inverse kinematics allowed feasible slip events to occur while satisfying (3.21). Thereafter, the polar form of $\boldsymbol{\lambda}_{\|}$ is decomposed into its Cartesian elements such that:

$$\lambda_x = |\lambda_{\|}|cos(\Theta), \tag{4.9}$$

$$\lambda_y = |\lambda_{\|}|sin(\Theta). \tag{4.10}$$

Altogether, (4.7) to (4.10) describe a contact model implementing the novel method of accurately modeling non-planar friction.

Stellenbosch University https://scholar.sun.ac.za

4.2. Experiments

The aim of this experiment was to prove the working of the presented method, and to compare it to a contact model implementing the polyhedral approximation of the 3D friction cone. This experiment was conducted under slippery surface conditions, when $\mu = 0.2$, and sticky surface conditions, when $\mu = 1.0$. Additional observations regarding the optimization setup and ϵ-relaxation techniques were made from these trajectories.

The trajectory optimization problem was implemented as described in Chapter 3, with the following specifications, and their respective contact model:

1. Robot: Monopod ($\boldsymbol{q} = \boldsymbol{q}_{Monopod}$),
2. Nodes: $N = 50$,
3. Estimated time of completion: $T = 0.5s$.

Figure 4.3 displays the friction pyramid, as seen from the z-axis. It can be seen that the underestimation of the pyramid approximation is maximized when the direction of motion lies 45° off the x-axis. When this occurs, the magnitude of the approximated coefficient of friction is $\mu_{pyramid} = 0.707\mu_{True}$, where μ_{True} is the real coefficient of friction, and $\mu_{pyramid}$ is the under-approximation thereof.

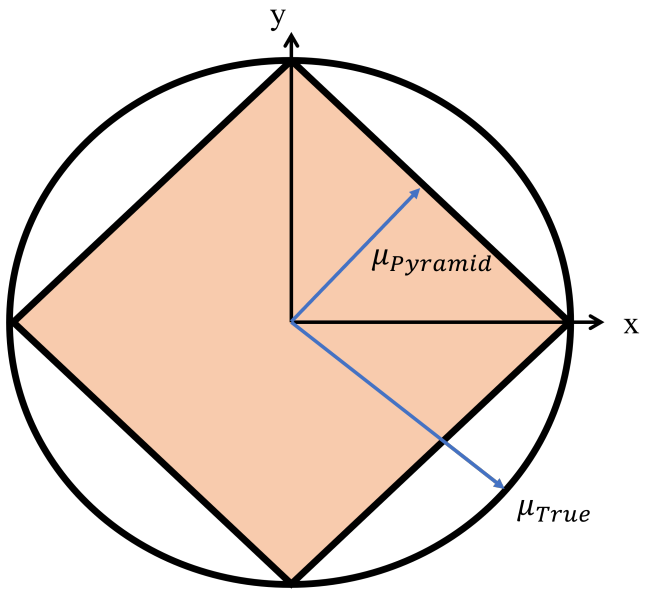

Figure 4.3: This image provides a top-down view of the four-sided friction pyramid, displayed in Figure 4.1, from the z-axis. Additionally, the underestimation of the friction pyramid, $\mu_{Pyramid}$, is highlighted. This occurs when the direction of relative velocity at contact lies between the axes defining the edges of the pyramid.

Stellenbosch University https://scholar.sun.ac.za

To generate trajectories exposing this underestimation, the robot was forced to move off the the Cartesian axis. This was done by setting the initial heading angle of the robot 45° off the x-axis: $\psi_{body}[1] = 45°$. Additionally, the direction of the initial velocity was constrained such that:

$$\dot{x}[1] = \dot{y}[1] \tag{4.11}$$

Periodic motion was constrained by constraining the initial pose of the robot to the final pose of the robot. However, to reduce the complexity of controlling the free-bodied monopod, the periodicity of the velocity state vector was not enforced. The initial value of all elements in $\boldsymbol{q}$ were constrained to equal the final value of $\boldsymbol{q}$, except for x and y. This allowed the robot to start in an optimal pose, and travel a distance along the Cartesian axis.

$$\boldsymbol{q}_{steady-state} = \boldsymbol{q}_0[N] = \boldsymbol{q}_0[1], \text{ except for } x, \text{ and } y. \tag{4.12}$$

A clear contact event was enforced by splitting the optimization into two flight phases with a contact phase in between. During this experiment, contact was enforced between nodes $n = 20$, and $n = 30$, as shown in Figure 4.4. Contact was forced by constraining $\lambda_z \leq \epsilon$ during the flight phases and $\lambda_z \geq$ BW during contact phase, where BW is the Newtonian weight of the robot. This forced contact to occur over a period of discrete elements while giving the optimizer freedom to determine the time duration, and magnitude of contact.

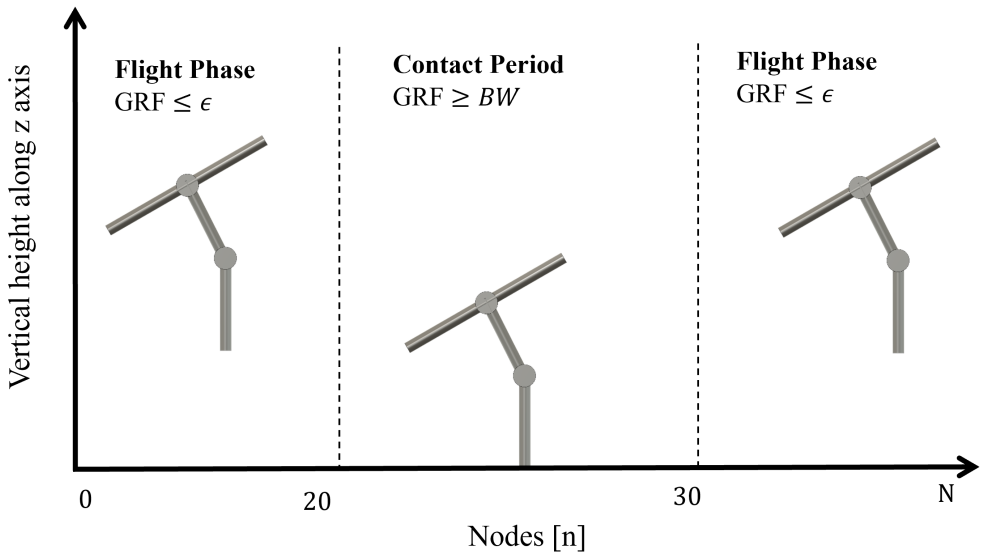

Figure 4.4: This image displays how contact was forced on the monopod robot.

Stellenbosch University https://scholar.sun.ac.za

4.3. Results

4.3.1. Computational Complexity

When starting the IP-OPT solver, the amount of variables and constraints passed to the solver were displayed. This data is displayed in Table 4.1, and used to compare the computational complexity of the respective optimization problem: implementing the novel method, and traditional polyhedral approximation, of modeling the 3D friction cone.

Implementing the novel method resulted in 1200 fewer variables, 600 fewer equality constraints, and 151 fewer constraints. Additionally, the ϵ-relaxation techniques framed the MPCCs as 'upper bound inequality constraints'. The implementation of the novel method passed 200 fewer MPCCs to the optimizer. These results are indicative of a significant reduction in computational complexity when implementing the novel method, compared the a similar implementation of the polyhedral approximation of the the 3D friction cone.

Table 4.1: A tally of equations, variables, and constraints passed to the IPOPT Solver for the trajectory optimization method implementing the respective method

	Novel Method	**Polyhedral Approximation**
Total number of variables	6856	8056
Variables with only lower bounds	459	459
Variables with lower and upper bounds	1800	2700
Variables with only upper bounds	0	0
Total of equality constraints	6400	7000
Total inequality constraints	901	1052
Lower bound inequality constraints	85	36
Upper and lower bound inequality constraints	400	400
Upper bound inequality constraints	416	616

4.3.2. Optimal Results

An optimal set of results from experiments explained above are shown in Figure 4.5a when $\mu = 1.0$, and Figure 4.5b when $\mu = 0.2$. For both experiments, the height of the contact point, ρ, vertical component of the GRF, λ_z, and effective coefficient of friction, $\mu_{effective} = \lambda_z / |\mu \lambda_{\|}|$ is presented. Animations of the trajectories displayed in this section are presented in https://youtu.be/HNU_gzRHLRs.

Stellenbosch University https://scholar.sun.ac.za

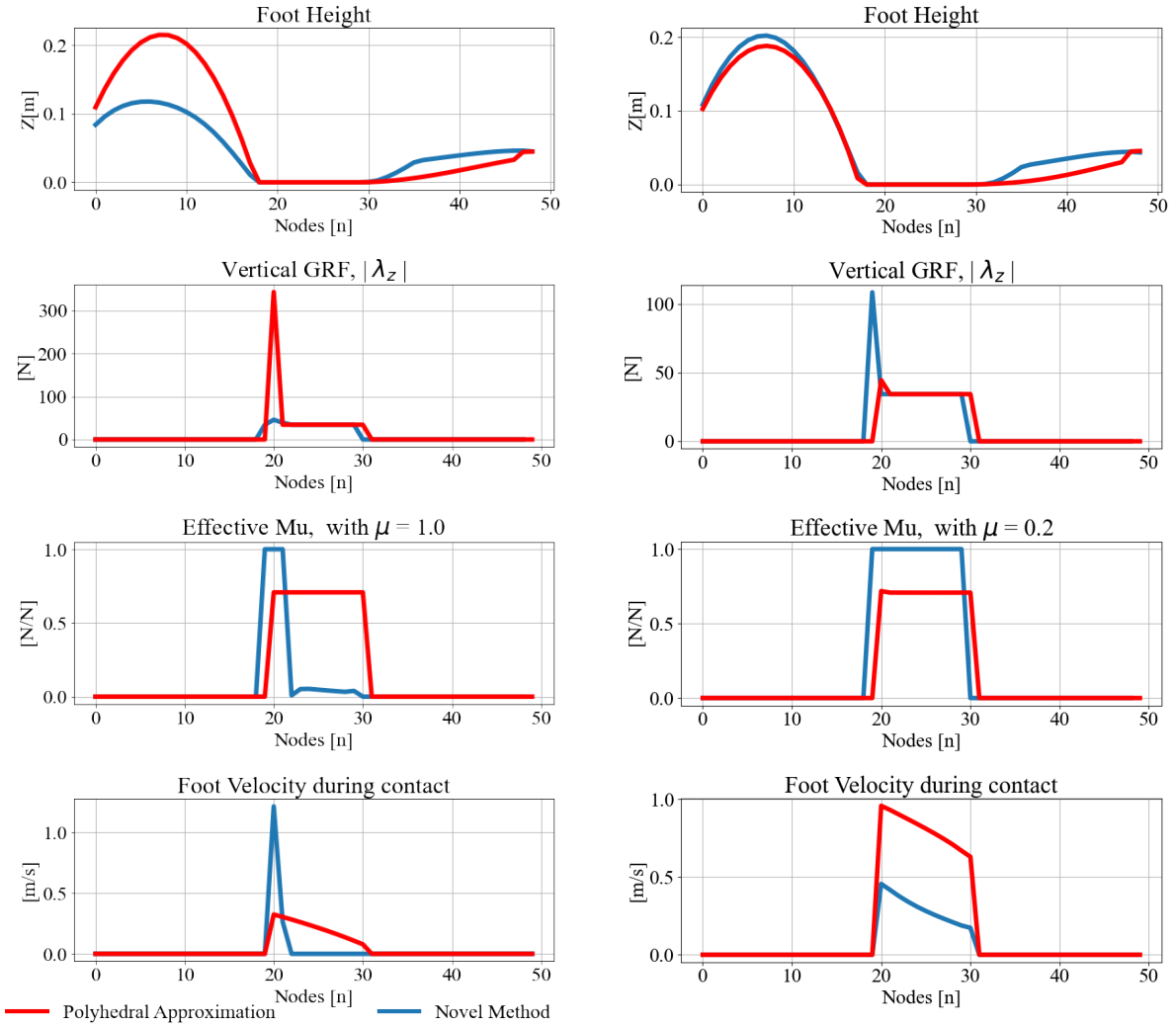

(a) A set of optimal trajectories modeling contact on a non-slippery surface, where $\mu = 1.0$.

(b) A set of optimal trajectories modeling contact on a slippery surface, where $\mu = 0.2$.

Figure 4.5: This image displays optimal trajectories that implement both the novel method (blue), and the polyhedral approximation (red), of modeling the 3D friction cone.

Contact was forced between nodes 20 and 30, and is evident in the satisfaction of the hard contact complimentarity: with $\lambda_z = 0$ during the flight phase of the trajectory, and $\rho = 0$ during the contact phase of the trajectories. Our novel method satisfies the slip MPCC, only allowing slip to occur when the effective coefficient of friction equals the surface coefficient of friction. Slip occured when the effective coefficient of friction clipped at $\mu_{effective} = 1.0$. However, both trajectories implementing the polyhedral approximation of the friction cone allowed slip to occur when $\mu_{effective} = 0.707$. This occurs because the direction of velocity was chosen to maximize the underestimation of the 3D friction cone as seen in Figure 4.3.

Stellenbosch University https://scholar.sun.ac.za

4.3.3. Epsilon Reduction Analysis

Due to the underapproximation exposed when implementing the friction pyramid in non-planar environments, and to maintain reliability of the results presented throughout the rest of the thesis, the novel method of modeling 3D friction will be used. It is worth noting that the tolerance of the IPOPT solver used in this research is set tol=$10E-6$, solving all decision variables within this tolerance. Since the ϵ-relaxation methods were applied on the MPCCs, all MPCCs were solved within a tolerance of ϵ.

In this research, the MPCCs were solved within a tolerance of $\epsilon \leq 1E-4$. However, this tight tolerance increases the scarcity of, and allowed for deep local minima within, the solution space. Therefore, this section will investigate how tight the ϵ-relaxation scheme needs to be to produce feasible and accurate trajectories of non-planar contact events.

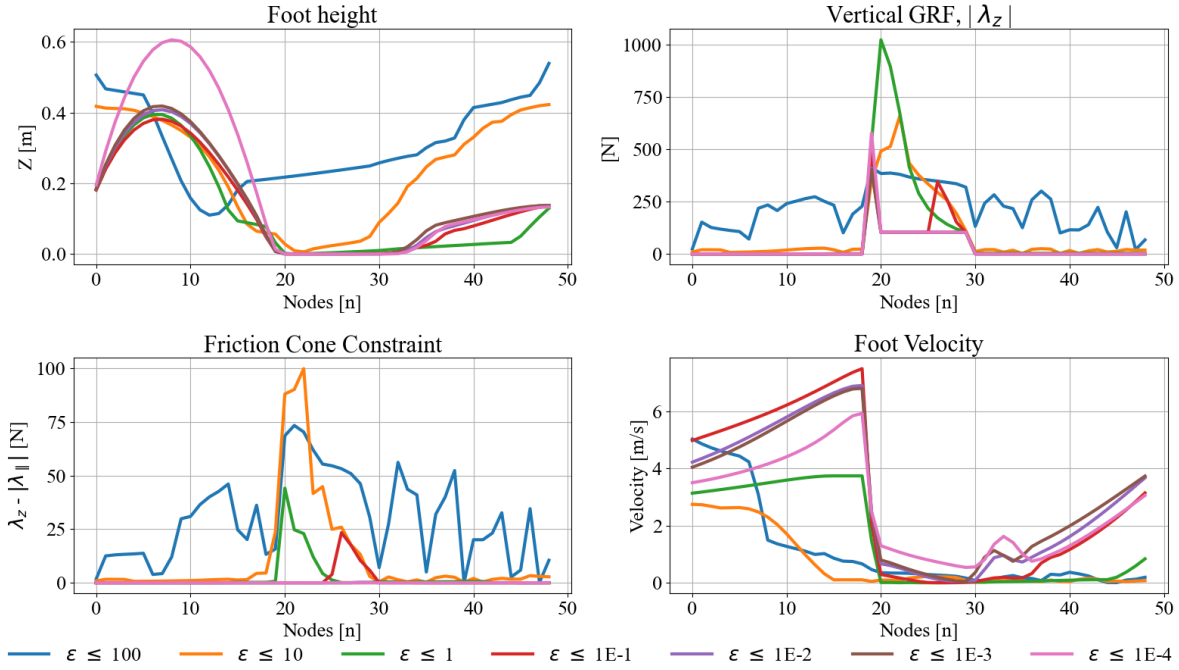

Figure 4.6: This image displays the slack variables from the slip trajectories that implemented the novel method of modeling the friction cone, scaled to base 10. The slack variable trajectories are displayed for different ϵ values.

Figure 4.6 displays the trajectories of the different slack variables used in implementing the novel method of modeling the friction cone, under slippery conditions and at all the different ϵ values. These slack variables were used to solve the trajectory implementing the novel method (the blue line) shown in Figure 4.5b. The graphs on the top row display how the hard contact MPCC was satisfied: the top left graph displaying the height of the contact point and the top right graph displaying the vertical component of the GRF. Whereas the graphs in the bottom row display how the friction cone MPCC was satisfied

Stellenbosch University https://scholar.sun.ac.za

with the bottom left graph displaying how the magnitude of the friction cone was computed, and the bottom right graph displaying the magnitude of the foot velocity. Additionally, the y-axis of these graphs are of a base 10.

From these graphs, it was evident that contact occured between nodes 20, and 30. Additionally, it was noticed that the foot height trajectory, and the GRF profile, converged when $\epsilon \leq 1E-1$ However, to investigate the effects of friction at a smaller scale, Figure 4.7 presents the same graphs with a log scaled y-axis.

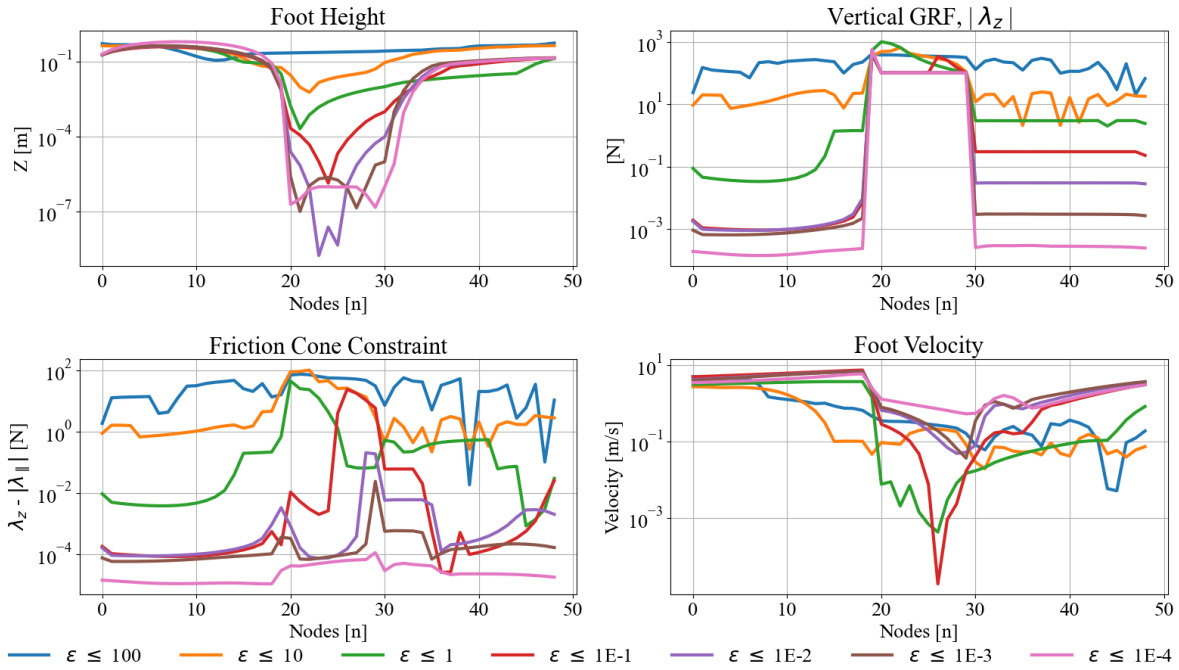

Figure 4.7: This image displays the slack variables from the slip trajectories that implemented the novel method of modeling the friction cone, scaled to a log scale. The slack variable trajectories are displayed for different ϵ values.

Large discontinuous dynamics were noticed when analysing the foot velocity, and friction cone, when log scaled. This highlights how computationally complex modeling friction events are. Additionally, a lot of the discontinuities were noticed when studying the friction cone constraint during the flight phase. However, we are interested in trends noticed during the contact period. It is noticed that the friction cone converged with the vertical GRF, when $\epsilon \leq 1E-1$. And the foot velocity converged when $\epsilon \leq 1E-2$.

Additionally, since the coefficient of friction was within the order of magnitude of 1, finding solution where $\epsilon \leq 1E-2$, satisfied the friction cone within a 1% tolerance. Figure 4.8 displays the trajectory of the effective coefficient of friction, $\mu_{effective} = \frac{\lambda_z}{\mu|\lambda_\parallel|}$, where $\epsilon \leq 1.0$. Confirming that the coefficient of friction converges tightly when $\epsilon \leq 1E-2$. Therefore, all solutions solved to tighter tolerances were redundant.

Stellenbosch University https://scholar.sun.ac.za

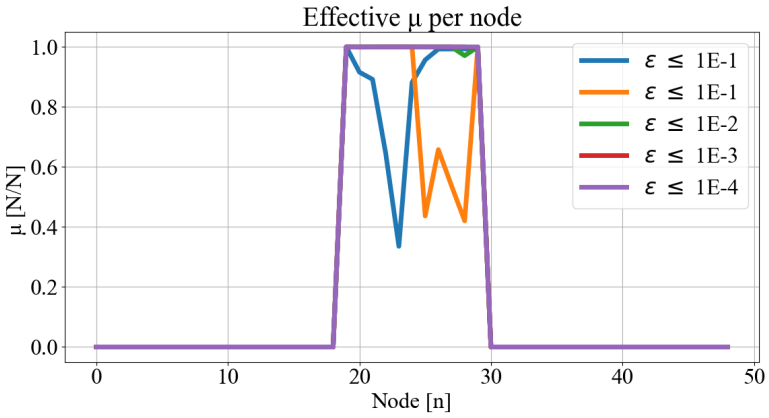

Figure 4.8: This image displays the effective coefficient of friction, $\mu_{effective} = \frac{\lambda_z}{\mu|\lambda_{\|}|}$. Slip occurred with the effective coefficient clipped at 1.0. These trajectories were seen to converge when $\epsilon \leq 1E-2$.

4.4. Discussion

This chapter set out to investigate the effects of contact in locomotion using a single contact. Reducing the investigation into single contact locomotion provided a comprehensive understanding of the effects of contact, friction, and slip.

Research conducted in this chapter contributed to legged robotic literature by presenting a novel method of computing the 3D friction cone using MPCCs which was published and presented at ICRA 2021 [57]. Here, the novel method was implemented in a contact implicit trajectory optimization framework, and compared with a four-sided implementation of the polyhedral approximation of the friction cone.

Results shown in Section 4.3 are significant as they show the benefits of using the novel method of computing the 3D friction cone using MPCCs. It was shown that the novel method is more reliable in satisfying Coulomb's law in non-planar environments, and resulted in a smaller, more computationally tractable the optimization problem being solved. Additionally, further investigations were conducted into the necessary accuracy needed for modeling contact events using ϵ-relaxation schemes. Consequently confirming the hypothesis that contact-implicit trajectory optimizations, solved using ϵ-relaxation schemes, achieve practical accuracy once a solution is found for ϵ less than 0.01.

Stellenbosch University https://scholar.sun.ac.za

Chapter 5

Realizing Dynamic Bipedal Motion

Studying non-planar monopod hopping in Chapter 4 provided the necessary insight into contact dynamics relevant to bipedal motion. First, the contact model used throughout the rest of this thesis was presented in the previous chapter. It highlighted the necessity of an accurate method of modeling the effects of friction using MPCCs. Finally, it drew insight to an appropriate level of computational accuracy needed to model contact events applicable to legged locomotion. However, all trajectories presented in this Chapter solve $\epsilon \leq 1E-4$.

These insights serve as adequate base knowledge into contact events, and can be expanded into studying dynamic bipedal locomotion. The first dynamic motion studied is steady-state running. Once steady-state running is sufficiently explored, we investigate how to achieve these steady-state gaits (accelerate) from a rest position; and how to return back (decelerate) to rest from these steady-state gaits.

Research conducted in this chapter expands on Fisher et. al's investigation into how legged robots should rapidly accelerate and decelerate [1]. The following experiments were conducted:

- Steady-state trajectories were generated for the biped robot.
- Acceleration and deceleration trajectories were generated from the apex of the steady-state gaits.

These separate trajectories were stitched together to generate a non-planar long-time-horizon trajectory (without the rapid turn), as seen in Figure 5.1. The emerging long-time-horizon trajectory was analyzed and compared to Fisher and Hubiki et. al's hypotheses regarding long-time-horizon trajectories [1, 26].

Stellenbosch University https://scholar.sun.ac.za

5.1. Bipedal Motion

Non-planar long-time-horizon bipedal trajectories are complex and computationally intractable. Therefore, they were broken into smaller task-specific trajectories and later stitched together as described in Chapter 3. This chapter describes, and investigates, the following sections of the long-time-horizon trajectories: acceleration, steady-state, and deceleration.

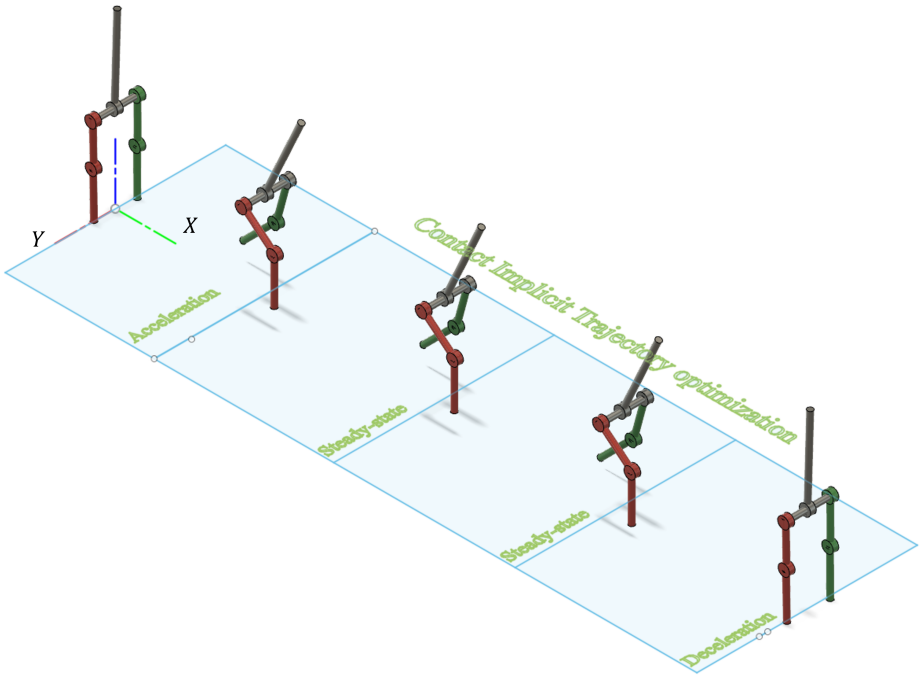

Figure 5.1: The figure displays the expected motion of the non-planar robot conducting a long-time-horizon dynamic trajectory along the x-axis. In the full trajectory, the robot started at rest, accelerated to a steady-state velocity, maintained that trajectory in a periodic gait, and then decelerated back to rest.

5.1.1. Steady-State Motion

Steady-state running refers to a periodic running gait at a specified velocity. Achieving any form of bipedal motion requires all parameters to vary. Therefore, the specified velocity is averaged out along its movement in the lateral plane. Additionally, a steady-state gait requires periodicity across all parameters [5, 65].

Stellenbosch University https://scholar.sun.ac.za

Experiments

In this thesis, steady-state trajectories were generated at multiple velocities, such that $v_{avg} \in \{0.5, 1.0, 2.0, 4.0\} m/s$. This set of optimal trajectories were used to define the starting bounds and final constraints necessary for the acceleration, deceleration, and rapid turn (presented in Chapter 6) trajectories for the respective velocity. Steady-state trajectories were generated from methods described in Chapter 3, with the following specifications:

1. Robot: Biped ($\boldsymbol{q} = \boldsymbol{q}_{Biped}$),
2. Nodes: $N = 100$ ($N = 150$ when $v_{avg} = 4m/s$),
3. Expected time: $T = 1.0$s.

Periodic motion was enforced by constraining the initial pose of the robot to the final pose of the robot for all elements in $\boldsymbol{q}$, except for the x generalized coordinate. A similar constraint was enforced on the full state velocity vector, as seen in (5.1). This allowed the robot to start in an optimal pose, travel a distance along the x axis, before ending in an optimal pose to enforce periodic motion.

$$\begin{aligned} \boldsymbol{q}_{steady-state} &= \boldsymbol{q}_0[\mathrm{N}] = \boldsymbol{q}_0[1] \text{ except } x, \\ \dot{\boldsymbol{q}}_{steady-state} &= \dot{\boldsymbol{q}}_0[\mathrm{N}] = \dot{\boldsymbol{q}}_0[0]. \end{aligned} \tag{5.1}$$

Figure 5.2 displays how a predictable contact order was encouraged by splitting the optimization into six phases: two contact phases, two ascending flight phases, and two descending flight phases. Contact was encouraged by constraining $\lambda_z \leq \epsilon$ during the flight phases, for the respective leg, and removing the constraint during contact phase. This allowed contact to occur over a series of nodes without explicitly enforcing a contact event.

The chosen contact order required the robot to first place its left foot, followed by its right foot. This was implemented by forcing contact of the left foot to *not* occur, by constraining $\lambda_{z,left} \leq \epsilon$, for $n \in \{0, \frac{N}{6}\}$ and $n \in \{\frac{2N}{6}, N\}$. Contact of the left foot was encouraged to occur by removing the constraint when $n \in \{\frac{N}{6}, \frac{2N}{6}\}$. Similarly, contact of the right foot was forced to *not* occur, by constraining $\lambda_{z,right} \leq \epsilon$, for $n \in \{0, \frac{4N}{6}\}$ and $n \in \{\frac{5N}{6}, N\}$. This constraint was removed, allowing right foot contact to occur, for $n \in \{\frac{4N}{6}, \frac{5N}{6}\}$.

Additionally, to ensure that steady-state *running* gaits were generated, the foot height height of the swing foot was constrained to be higher than 5cm above the contact surface. Since the left foot made contact in the first half of the trajectory, the right leg was the

Stellenbosch University https://scholar.sun.ac.za

swing leg for the first half of the trajectory. Similarly, the right foot made contact, and the left contact became the swing leg, during the second half of the trajectory. This was enforced by implementing the following constraint:

$$\begin{aligned} \rho_{right} \geq 0.05, \text{ for } n \in (1, \frac{N}{2}) \\ \text{and } \rho_{left} \geq 0.05, \text{ for } n \in (\frac{N}{2}, N). \end{aligned} \tag{5.2}$$

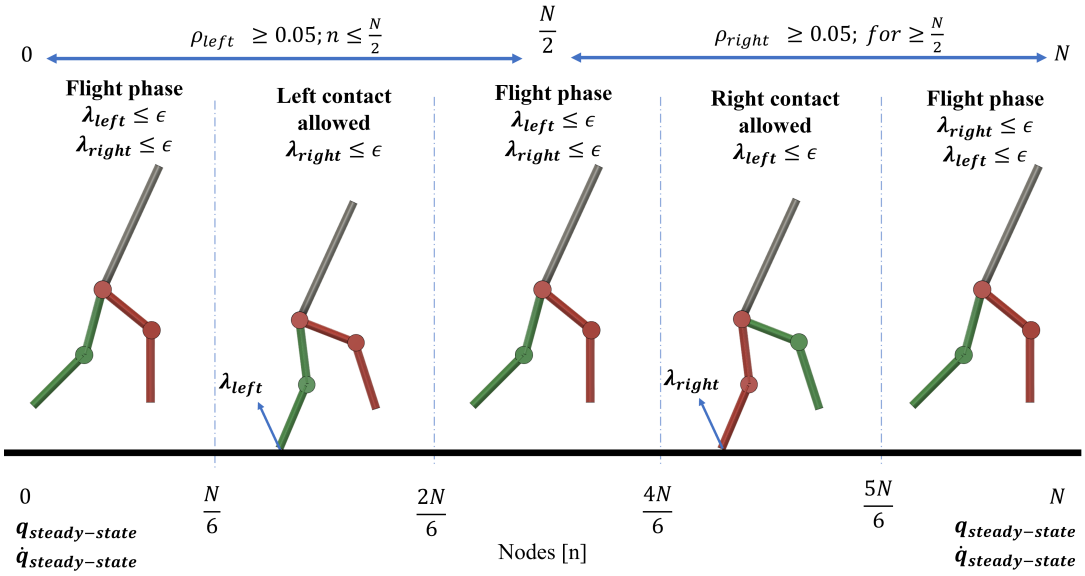

Figure 5.2: This figure displays how a prescribed contact order was encouraged in the steady-state trajectories. The left contact was was constrained to occur in the first half of the optimization. Whereas, the right contact was constrained to occur in the second. Additionally, the right foot was constrained 5cm above ground for the first half of the optimization, and the left foot for the second half.

Average Velocity

An average velocity constraint was enforced for the steady-state gait. This allowed the optimizer to find an optimal set of initial and terminal velocities satisfying this constraint:

$$v_{avg} \leq \frac{x_0[N] - x_0[0]}{tt_0[N] - tt_0[0]}. \tag{5.3}$$

Here, $x_0[N]$ described the distance that the robot moved along the x-axis, and $x_0[0]$ the initial position of the robot on the x-axis ($x_0[0] = 0$m). Similarly, $tt_0[N]$ described the duration of the trajectory, $tt_0[0]$ was the starting time of the trajectory ($tt_0[0] = 0$s), and v_{avg} described the average velocity. When applied as a constraint in the optimization, the initial position, and start time was considered and removed, allowing the constraint to be

Stellenbosch University https://scholar.sun.ac.za

rearranged as:

$$x_0[N] \geq v_{avg} \cdot tt_0[N]. \tag{5.4}$$

Note that this was a constraint on the average velocity of the robot, not on its initial or terminal velocities. Therefore, the optimizer had to find an optimal and kinematically feasible solution that moved the robot far enough along the x-axis at a speed satisfying this constraint.

5.1.2. Acceleration And Deceleration

From these optimal steady-state trajectories, acceleration trajectories were generated to demonstrate the ability of the robot to achieve the apex of the steady-state gait from rest, seen in Figure 5.3a. Similarly, deceleration trajectories were generated to demonstrate the ability of the robot to return back to rest from the apex of the steady-state gait, seen in Figure 5.3b.

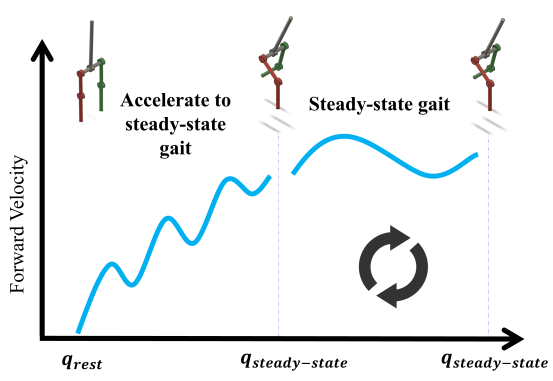

(a) This image displays how the robot accelerates from a rest position to the apex of the steady-state gait.

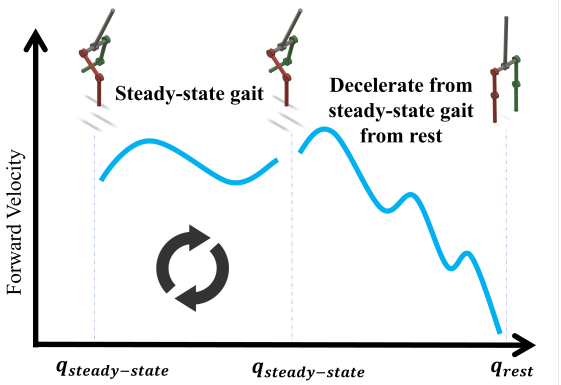

(b) This image displays how the robot decelerates back to the rest position from the apex of the steady-state gait.

Figure 5.3: These images display how the steady-state trajectories are achieved from rest, and how the robot returns back to rest from the apex of the steady-state trajectory.

Both acceleration and deceleration trajectories were generated through the implementation of the trajectory optimization method described in Chapter 3, with additional specifications:

1. Robot: Biped ($\boldsymbol{q} = \boldsymbol{q}_{Biped}$),
2. Nodes: $N = 100$ ($N = 150$ when $v_{avg} = 4m/s$),
3. Expected time: T=1.0s.

Stellenbosch University https://scholar.sun.ac.za

Acceleration trajectories required the robot to start in rest, at the origin of the Cartesian plane, facing the positive x-axis. Its final pose was constrained to the apex of the steady-state gait for each respective velocity. This was implemented by setting the initial, and constraining the final, state position and velocities as follows:

$$\begin{aligned} \boldsymbol{q}_0[0] &= \boldsymbol{q}_{rest}, \text{ with } x = 0.0, \\ \dot{\boldsymbol{q}}_0[0] &= \dot{\boldsymbol{q}}_{rest}, \\ \boldsymbol{q}_0[\mathrm{N}] &= \boldsymbol{q}_{steady-state}, \text{ except } x, \\ \text{and } \dot{\boldsymbol{q}}_0[\mathrm{N}] &= \dot{\boldsymbol{q}}_{steady-state}. \end{aligned} \tag{5.5}$$

Similarly, deceleration trajectories required the robot to start at the apex pose of the steady-state trajectory for each respective velocity, at the origin of the Cartesian Plane. Its final pose was constrained to a rest position, with the x element left unconstrained. This allowed the optimizer to find an optimal x distance needed to decelerate the robot to a rest position. These specifications were achieved setting the initial, and constraining the final, state position and velocities as:

$$\begin{aligned} \boldsymbol{q}_0[0] &= \boldsymbol{q}_{steady-state}, \text{ with } x = 0.0, \\ \dot{\boldsymbol{q}}_0[0] &= \dot{\boldsymbol{q}}_{steady-state}, \\ \boldsymbol{q}_0[\mathrm{N}] &= \boldsymbol{q}_{rest}, \text{ except } x, \\ \text{and } \dot{\boldsymbol{q}}_0[\mathrm{N}] &= \dot{\boldsymbol{q}}_{rest}. \end{aligned} \tag{5.6}$$

5.2. Results

These results aim to show how periodic steady-state gaits were generated. Thereafter, acceleration trajectories are presented to show how the robot achieved these gaits from a rest position. Deceleration trajectories are presented to show how it returned back to rest from these gaits. Additionally, these results were stitched together to form a long-time-horizon trajectory, and heuristics were identified. Animations of the presented trajectories can be found at: https://youtu.be/8kUCbQJLQ2M.

5.2.1. Steady-State Results

Initially, steady-state gaits were generated without (5.2), enforcing a flight period. This was achieved by deactivating the constraint describing (5.2). Therefore, the optimizer was able to find a set of energetically optimal gaits at the specified average velocity. The foot-fall patterns for these trajectories are seen in the right column of Figure 5.4.

Stellenbosch University https://scholar.sun.ac.za

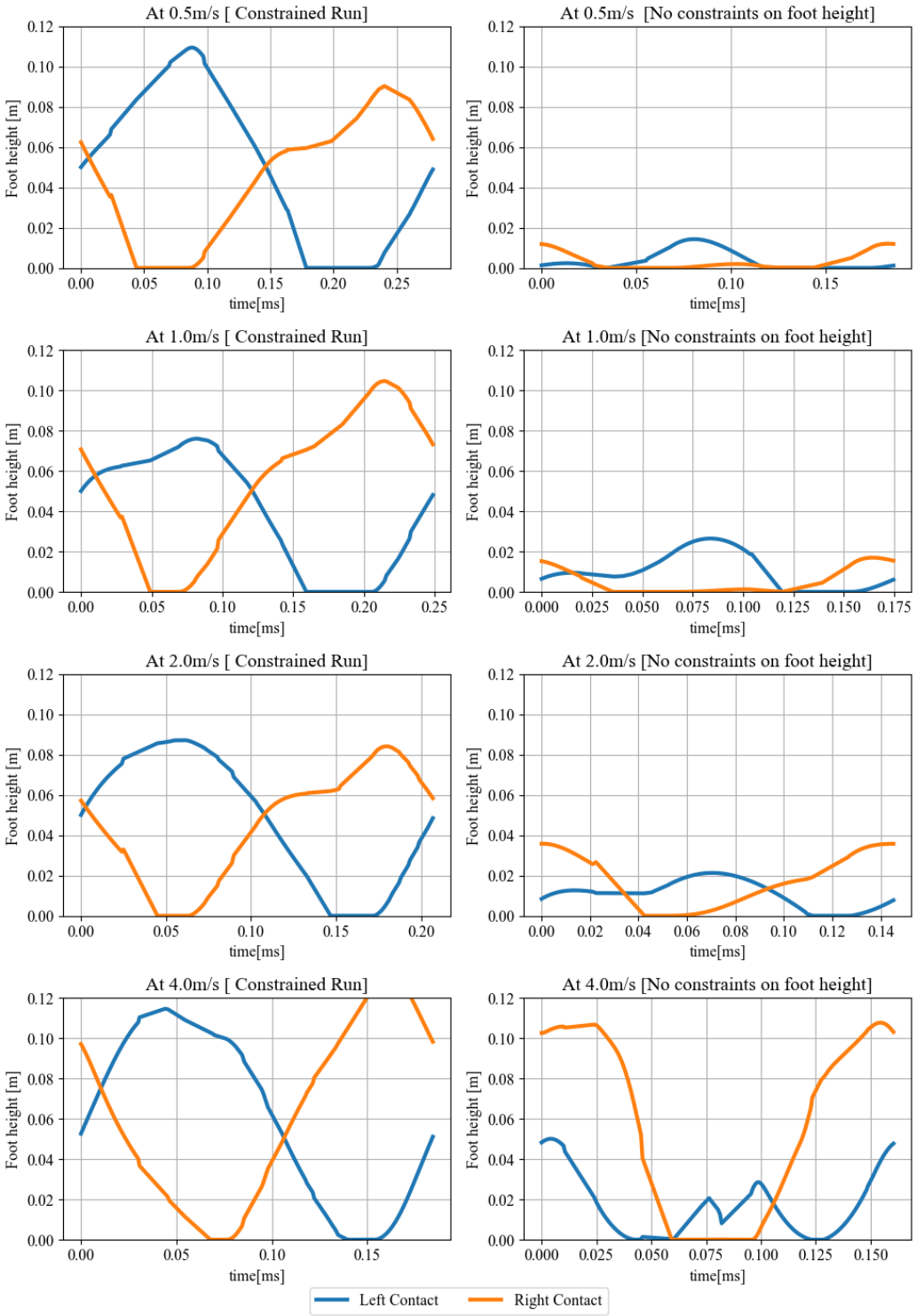

Figure 5.4: This image displays the foot-height seen during steady-state trajectories at different speeds. Graphs displayed in the left column show the foot-height seen during steady-state gaits with with (5.2) enforcing a flight period. Whereas, graphs displayed in the right column show the foot-height seen during steady steady-state gaits without (5.2), enforcing a flight period.

However, since contact was only allowed to occur during the phases shown in Figure 5.2, traditional walking gaits with prolonged periods of contact could not naturally emerge.

Stellenbosch University https://scholar.sun.ac.za

The trajectory was seen to graze the foot above the ground, finding kinematically feasible solutions that didn't exert GRFs while grazing the foot above the ground. Therefore, for the analysis, the foot was deemed to be in contact when the foot height was less than 1cm above the ground, when $\rho \leq 0.01$m. With the absence of an identifiable flight period, the robot was seen to walk at 0.5m/s, and 1.0m/s. Flight periods seen at 2.0m/s, and 4.0m/s, were indicative of running gaits.

These observations are consistent with Alexander et. al.'s [2,3] hypothesis of the optimal walk-run transition speed occurring when $Fr \approx 0.5$, as described in Chapter 2. For the robot used in this research, the optimal speed for transitioning between the walking gait and the running gait occurs when $v \approx 1.42$m/s. Results shown in Figure 5.4 are consistent with this hypothesis, as walking gaits emerged when the average velocity was constrained to 1.0m/s and 0.5m/s, where $v \leq 1.42$m/s. Whereas, running gaits emerged when the average velocity was constrained to run at 2.0m/s, and 4.0m/s, where $v \geq 1.42$m/s.

However, this thesis aimed to study dynamic steady-state running motions. Therefore, steady-state running gaits were generated with (5.2) enforcing a flight period. These foot-fall trajectories are seen in the left column of Figure 5.4. Here, all the gaits generated at all speeds investigated had significant flight periods.

To prove the working of the steady-state running gaits, the periodicity, and the average running velocity, of each trajectory were examined. Identification of limit cycles within a phase plot were used to verify the periodicity of the trajectory . This was done by plotting each state-vector, with respect to its time derivative ($\dot{\boldsymbol{q}}$ vs $\boldsymbol{q}$) [4, 5, 65]. Figure 5.5 displays the phase plot of each element of the state vector, $\boldsymbol{q}$.

Periodicity was enforced for all elements defining $\boldsymbol{q}$, except for the x variable. Whereas, the average velocity constraint was applied to the set of x variables. The top left graph in Figure 5.5 displays how the average velocity constraint was satisfied for each speed of interest. Additionally, clear limit-cycles were evident within the rest of the phase plots, verifying the periodicity of the steady-state trajectories.

Stellenbosch University https://scholar.sun.ac.za

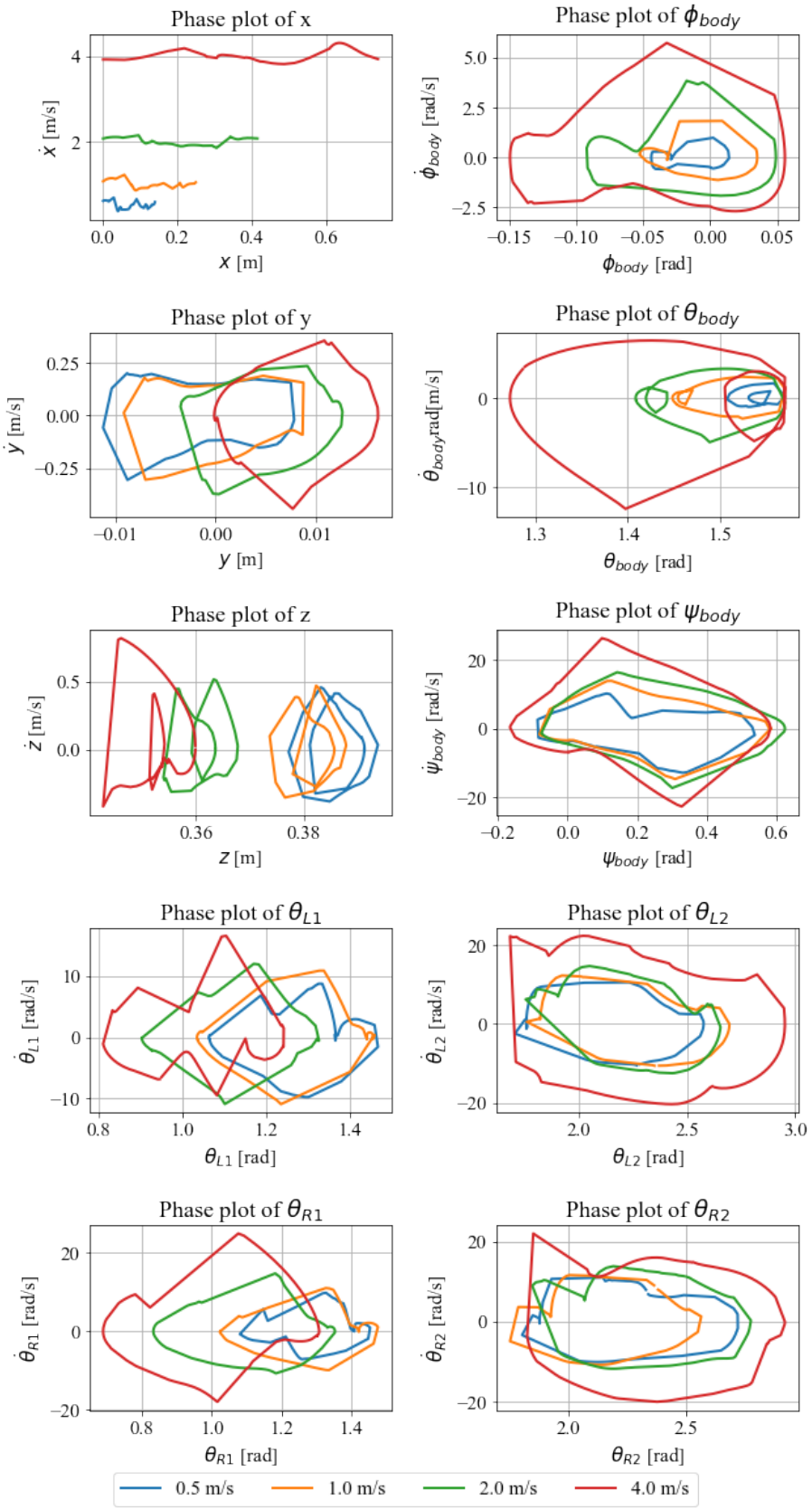

Figure 5.5: This image displays the phase plots of all the state variables during steady-state trajectories at all the speeds investigated. Clear limit cycles are seen in all state-variables except x.

Stellenbosch University https://scholar.sun.ac.za

5.2.2. Acceleration And Deceleration

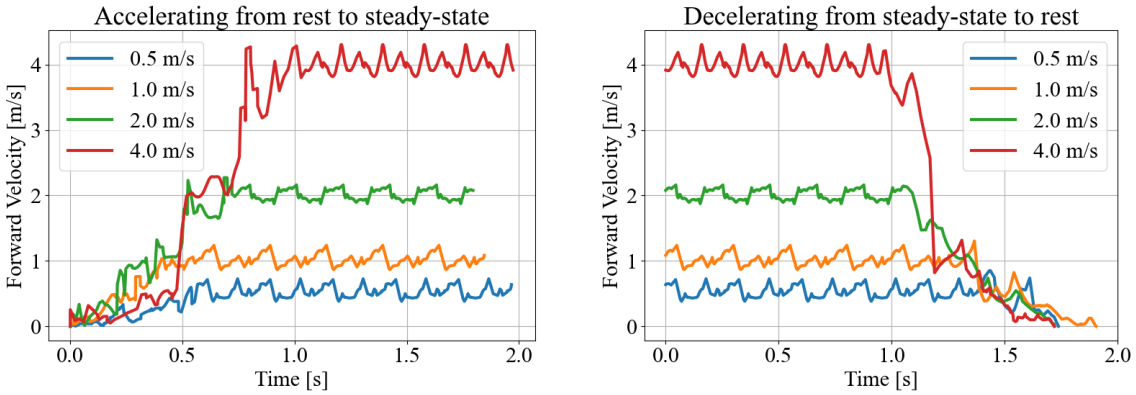

(a) This image displays the forward velocities of the robot accelerating from rest to the apex of steady-state gaits.

(b) This image displays the forward velocities of the robot decelerating too rest from the apex of a steady-state gait.

Figure 5.6: These images display the forward velocity of the robot accelerating too, and decelerating from, the apex of steady-state gaits.

To prove the realizability of the steady-state gaits presented, acceleration gaits were from the rest position to the steady-state pose at each respective velocity. Similarly, deceleration trajectories were generated to prove that the robot can feasibly return back to rest from the steady-state gaits.

These trajectories are presented in Figure 5.6, where the the forward velocities are displayed of the different acceleration and deceleration trajectories. These trajectories were stitched onto the forward velocity profile of their respective steady-state trajectory to maintain its velocity.

Additionally it can be seen that in all trajectories, the robot aims to jump straight into its desired gait. This is seen in the consistency of the rate of acceleration on all the graphs. In all the trajectories, a similar rate of acceleration is seen, ranging from 1.12m/s^2 to 4.12m/s^2. Similarly, deceleration trajectories were seen to jump straight to the rest position. Rapid deceleration occurred, with a rate of deceleration ranging from 2.42m/s^2 to 1.13m/s^2.

5.3. Discussion

A “bang-coast-bang” template was identified in the velocity profile after placing Figure 5.6a and Figure 5.6b side-by-side. This template was confirmed after joining the trajectories to reveal a set of long-time-horizon trajectories shown in Figure 5.7. These long-time-horizon

Stellenbosch University https://scholar.sun.ac.za

trajectories started the robot at rest, accelerated it to a steady-state gait to maintain a desired speed, and then decelerated it back to rest.

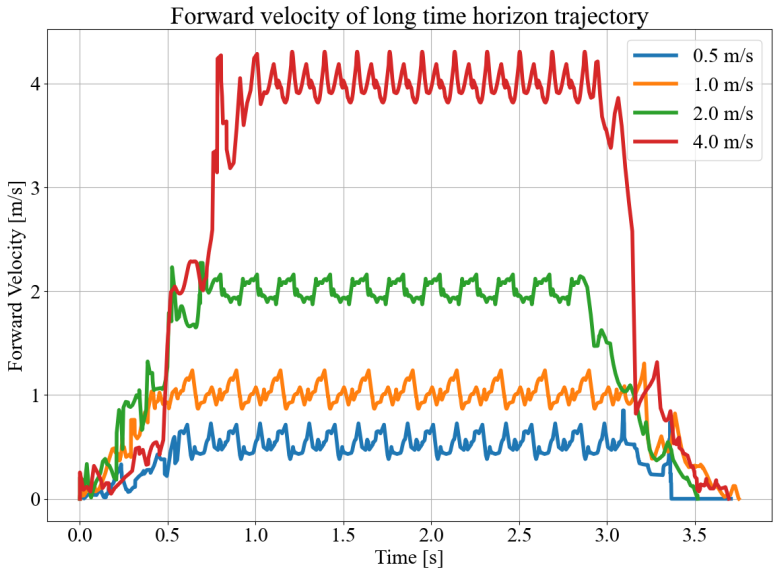

Figure 5.7: This image displays long-time-horizon trajectories at different speeds. Here, the acceleration, and deceleration, trajectories stitched onto periodic steady-state trajectories steady-state trajectories.

Bang-coast-bang control describes the velocity profile of sliding mass subject to friction, and a horizontal applied force. The following dynamics describe this velocity profile:

$$m \cdot \ddot{x}(t) = F(t) - c \cdot \dot{x}(t). \tag{5.7}$$

Here, an applied force, $F(t)$, and a viscous friction, c, actuate on mass, m. Further, 1 DOF is used to describe the position, x, velocity, $\dot{x}$, and, acceleration, $\ddot{x}$, of m [1,4,8,26]. Figure 5.8 displays an accurate correlation between the bang-coast-bang control, and the 2m/s long-time-horizon velocity profile. This serves as an accurate estimation of the velocity profile of a system conducting rapid movements on a bipedal platform.

Hubicki et. al [26] first identified this template when optimizing planar long-time-horizon monopedal trajectories and hypothesized the template holding for more complex models. Thereafter, Fisher et. al. [1] expanded on this and presented a sliding mass profile emerging on planar long-time-horizon trajectories on planar bipedal, and quadrupedal, platforms. Thereby, adding the hypothesis of the sliding mass template holding for more complex models. Results shown display the sliding mass model emerge when optimizing a long-time-horizon trajectory of a non-planar bipedal robot, with splayed hips.

Stellenbosch University https://scholar.sun.ac.za

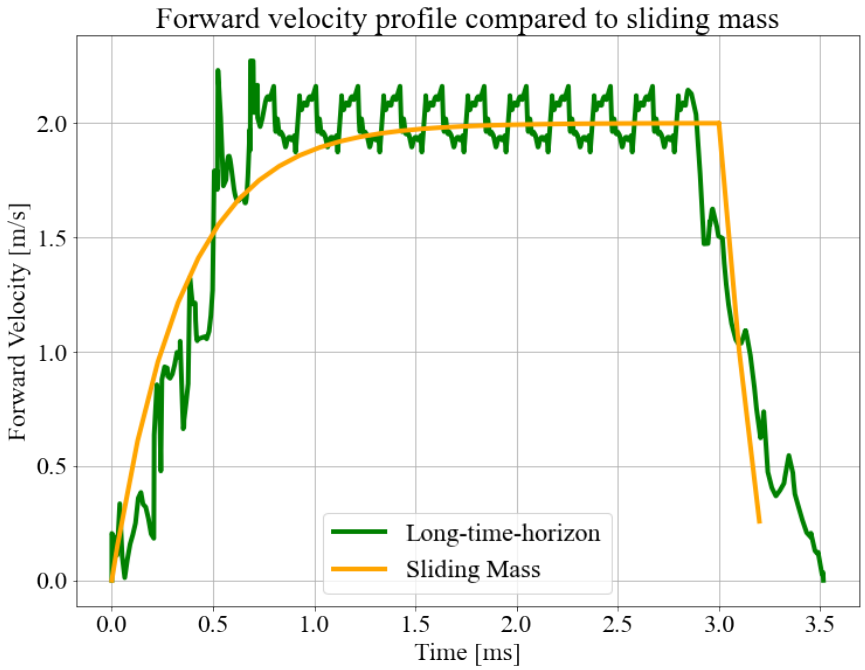

Figure 5.8: This image displays the correlation between the velocity profile of a sliding mass, and the $2.0m/s$ long-time-horizon trajectory.

Stellenbosch University https://scholar.sun.ac.za

Chapter 6

Bipedal Turning: To Slip Or Not To Slip?

The aim of this chapter was to investigate methods of how bipedal robots conduct rapid turns. Due to the transient nature of these turn trajectories, the prevalence of slip events is hypothesized to by significant - motivating the study of friction and slip modelling in Chapter 4. Additionally, we aimed to conduct this study into rapid turning from feasible and optimal starting poses - motivating the study into dynamic bipedal motion presented in Chapter 5. These insights serve as a strong foundation for studying the significance of slip, and kinematic trends, when conducting rapid turns.

Additionally, results shown in this section were submitted for review in the RA-L journal [94]. The research presented in this chapter aimed to answer the following questions:

- How prevalent are the effects of slip while conducting rapid turns?
- Are there any kinematic trends noticed when conducting rapid turns to different degrees and different speeds?

These questions were answered by analyzing trajectories describing turns at different turn angles and different speeds. Additionally, long-time-horizon trajectories, including a rapid turn, were presented as seen in Figure 6.1.

6.1. Turning

In dynamic locomotion, turning is distinct from acceleration, deceleration, or steady-state motion. It is often conducted in the context of running. In nature, humans and animals are seen to conduct rapid turn events from a desired velocity. Therefore, turns conducted

Stellenbosch University https://scholar.sun.ac.za

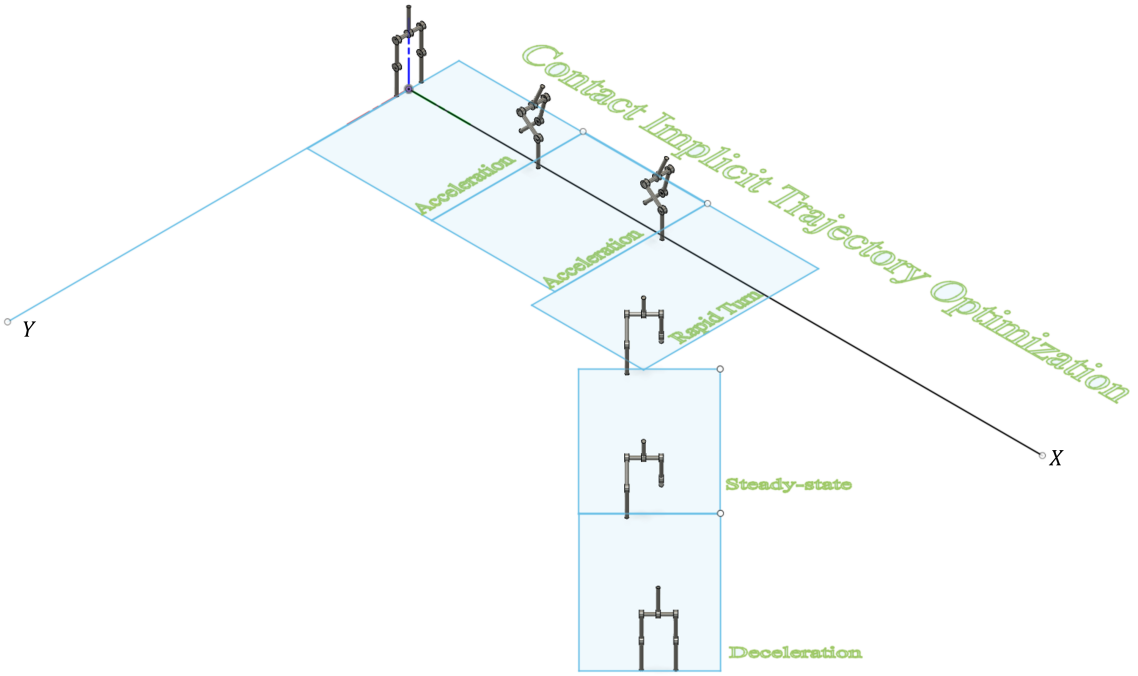

Figure 6.1: This image displays the phases of the long-time-horizon trajectory, including a rapid turn off the sagittal plane. Here, the robot accelerated from a rest position, to the apex of a steady-state gait, maintained the steady-state gait along the x axis, and conducted a rapid turn from the apex of the steady-state gait. The rapid turn ended in the apex of the steady-state gait, offset by the turn angle, maintained the steady-state gait, and decelerated back to rest.

in this chapter start at the apex of optimal steady-state gaits. This is done to ensure kinematic feasibility of the trajectories presented in this research.

Rapid turns are distinct from other phases of motion in that the "heading" of the robot changes during the motion. The heading of the robot refers to the direction of both the velocity of the system, "path heading", and the direction the robot is facing, "system heading". Perkins et. al. [5] defines the system heading as "the orientation of a longitudinal axis projected onto the horizontal plane". In this research, the horizontal plane is aligned with the hip axis, and is projected onto the coronal plane to determine the system heading, shown as ψ_{body} angle in $\boldsymbol{q}$. Additionally, the path heading is described by the Cartesian velocity of the system, such that $\boldsymbol{v} = [\dot{x}\ \dot{y}]^T$, where $\dot{x}$ and $\dot{y}$ are elements of $\dot{\boldsymbol{q}}$. Figure 6.2 provides a graphical representation of the robot heading as shown in a view of the bipedal robot from the z-axis. The distinction between the two allows for sideways running to be described when the heading angles are perpendicular to each other [5].

Rapid turns are conducted once both the path, and system, headings are changed equally. Therefore, the final conditions of both the path heading and the system heading are offset from the initial conditions by the desired turn angle.

Additionally, Perkins et. al. [5] concluded that turn trajectories can be initiated on

Stellenbosch University https://scholar.sun.ac.za

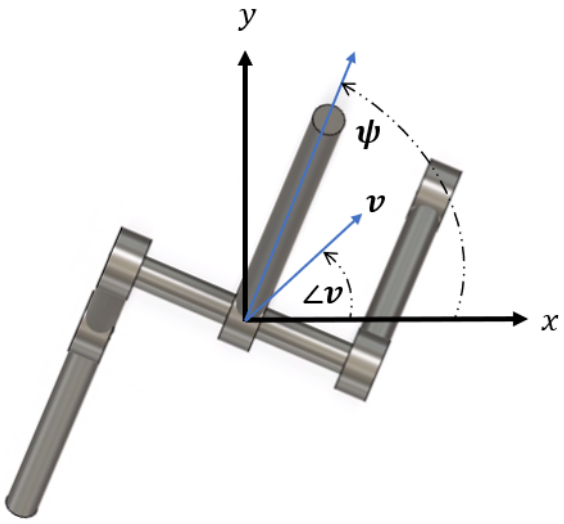

Figure 6.2: A graphical description of the robot heading, shown in view of the bipedal robot z-axis. The system heading is described by ψ_{body} angle in $\boldsymbol{q}$, and the path heading is described by the Cartesian sum of the $\dot{x}$ and $\dot{y}$ elements of $\dot{\boldsymbol{q}}$.

both the inner, and outer, legs. The inner leg refers to the leg closer to, and the outer leg refers to the leg farther from, the center of the turn.

Steady-state trajectories presented in Chapter 5 lifted off the right foot, and positioned itself to place the left contact next to maintain periodicity. This resulted in right turns being initiated off the outer-leg, and left turns being initiated off the inner leg. The bulk of the experiments conducted in this chapter turn to the right, off the outer leg. To prove that the model is agnostic to turning off the inner leg, or outer leg, an additional investigation into turning to the left was also conducted.

6.2. Experiments

A series of experiments into rapid turning were conducted by implementing the trajectory optimization experiment described in Chapter 3 with the following specifications:

1. Robot: Biped ($\boldsymbol{q} = \boldsymbol{q}_{Biped}$),
2. Nodes: $N = 100$ ($N = 150$ when $v_{avg} = 4.0$),
3. Expected Time: $T = 1.0$s.

Start conditions of rapid turns were set at the apex of the steady-state trajectories for the desired velocity presented in Chapter 5. Similarly, end conditions were constrained to the apex of the steady-state trajectory, with the path and system heading offset by the

Stellenbosch University https://scholar.sun.ac.za

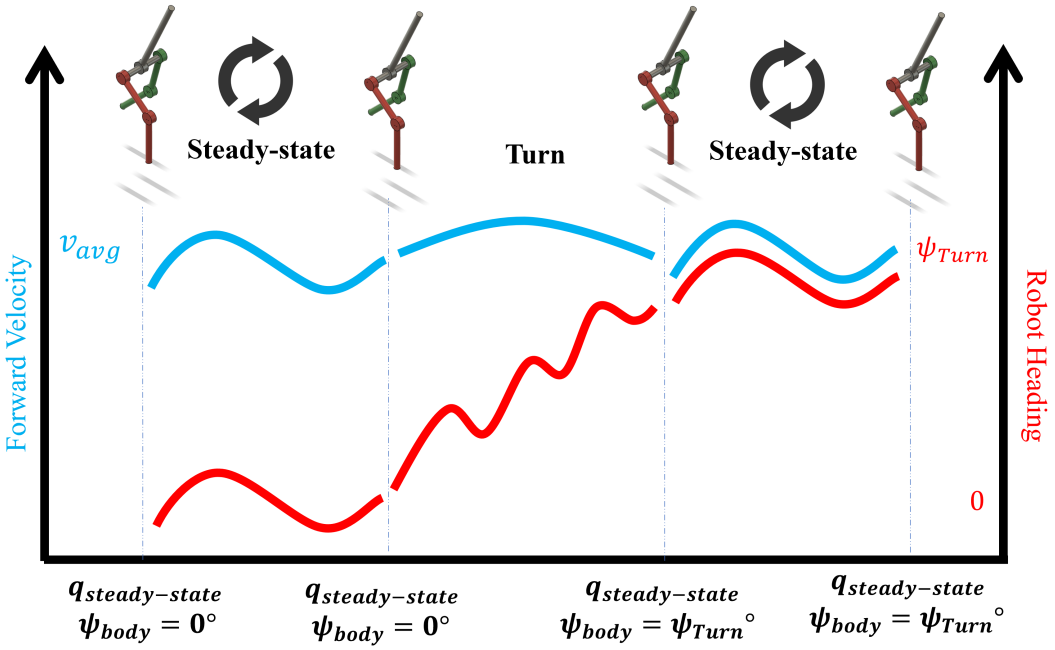

Figure 6.3: This image displays how the rapid turn trajectories started in apex pose of the steady-state trajectories. Similarly, the final pose of the rapid turn trajectories ended in the apex pose of the steady-state gait, with the robot heading offset by the specified turn angle, ψ_{Turn}.

desired turn angle, ψ_{Turn}. These conditions were achieved by setting the initial conditions, and constraining the final conditions, as shown:

$$\begin{aligned} \boldsymbol{q}_0[0] &= \boldsymbol{q}_{steady-state}, \\ \dot{\boldsymbol{q}}_0[0] &= \dot{\boldsymbol{q}}_{steady-state}, \\ \boldsymbol{q}_0[\mathrm{N}] &= \boldsymbol{q}_{steady-state}, \text{ excluding } x, y, \text{ and } \psi_{body}, \\ \dot{\boldsymbol{q}}_0[\mathrm{N}] &= \dot{\boldsymbol{q}}_{steady-state}, \text{ excluding } \dot{x}, \text{ and } \dot{y}. \end{aligned} \tag{6.1}$$

Final x, and y-values were left unconstrained. This allowed the optimizer to find an optimal footfall pattern, and area, necessary to complete a rapid turn. Additionally, the path heading was constrained by decomposing the velocity of the system into the Cartesian elements offset by the desired turn angle, ψ_{Turn}. With the velocity of the steady-state trajectory known, $v_{steady-state}$, the elements of the final velocity vector was offset by the desired turn angle, ψ_{Turn}:

Stellenbosch University https://scholar.sun.ac.za

$$
\begin{aligned}
|v_{steady-state}| &= \sqrt{\dot{x}^2_{steady-state} + \dot{y}^2_{steady-state}}, \\
\dot{x}_0[N] &= |v_{steady-state}| cos(\psi_{Turn}), \\
\dot{y}_0[N] &= |v_{steady-state}| sin(\psi_{Turn}), \\
\text{and } \psi[N] &= \psi_{Turn}.
\end{aligned} \tag{6.2}
$$

6.3. Results

To investigate the effect that the speed of the robot had on the turn trajectory, rapid turning was conducted at multiple velocities with a fixed turn angle, such that $v_{avg} \in \{0.5, 1.0, 2.0, 4.0\}$m/s and $\psi_{Turn} = 45°$.

Similarly, to investigate the effect that the degree of the turn angle has on the turn trajectory, rapid turning was conducted with a fixed velocity and multiple turn angles, such that $v_{avg} = 2.0$m/s and $\psi_{Turn} \in \{22.5°, 30°, 45°, 60°, 90°\}$.

For each degree, and speed, of interest 5 trajectories were generated. These sets of trajectories were used to compute statistical characteristics presented in this section. From these sets, the trajectory with the lowest objective function was identified as the optimal trajectory for that particular speed or turn angle.

All turns presented in the above experiments turned to the right, towards the inside leg. Finally, to prove that the optimization can turn to both directions, a small investigation was conducted. Here, the robot was constrained to turn to the left from a 2.0m/s steady-state gait, at multiple turn angles, $\psi_{Turn} \in \{-30°, -45°, -60°, -90°\}$.

Animations of the turn trajectories presented in this chapter can be found at: https://youtu.be/BdrJcXKk_68.

6.3.1. Turning At Varying Speeds

Table 6.1 displays statistical characters from the sets of trajectories described in the experiment conducting a 45° rapid turns at multiple speeds. These statistical characteristics revealed clear trends.

A decreasing trend was noticed in the average duration of contact compared to the average trajectory duration as the velocity of the robot increased. When the velocity of

Stellenbosch University https://scholar.sun.ac.za

the robot was 0.5m/s, contact occurred 75.24% of the trajectory duration; 61.19% at 1.0 m/s; 34.38% at 2.0 m/s; and 26.02% at 4.0m/s.

The duration of slip relative to the duration of contact was seen to increase proportionally to the velocity of the robot. When the robot speed was 0.5m/s, slip occured 93.32% of the average contact duration; 94.42% at 1.0m/s; 99.65% at 2.0m/s; and 100% at 4.0m/s.

Table 6.1: Statistical characteristics of rapid turns conducted at varying speeds. These characteristics were developed using a sample set of 5 trajectories per speed investigated.

Average Speed [m/s]	0.5	1.0	2.0	4.0
Mean trajectory duration [ms]	493.16	469.75	390.20	495.54
Variance in trajectory duration [ms]	4.04	7.62	0.07	2.8
Mean air time [ms]	122.11	182.29	256.03	366.57
Variance in air time [ms]	2.15	7.52	0.11	1.96
Mean contact time [ms]	371.06	287.46	134.17	128.97
Variance in contact time [ms]	0.45	14.49	0.13	0.82
Mean slip time [ms]	346.29	271.44	133.71	128.97
Variance in time [ms]	0.45	14.49	0.13	0.82

Figure 6.4 displays the change in system heading, ψ_{body}, for a set of optimal trajectories describing the robot conducting 45° turns at multiple speeds. Here, overshoot occurred in all trajectories. The magnitude of overshoot was noticed to increase as the speed of the robot increased. An overshoot of 0.25° was noticed when the robot's speed was 0.5m/s, 10.07° at 1.0m.s, 21.29° at 2.0m.s, and 35.80° at 4.0m/s.

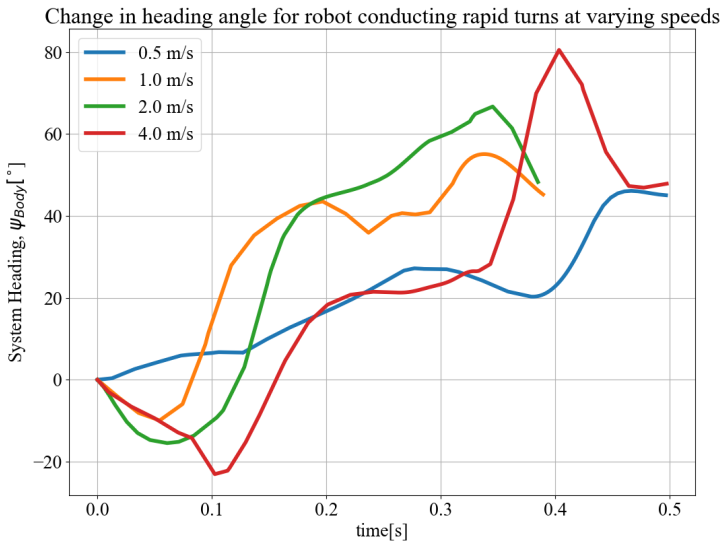

Figure 6.4: The image displays optimal trajectories of the change in heading angle of the robot conducting rapid turns at varying speeds.

Stellenbosch University https://scholar.sun.ac.za

6.3.2. Turning At Varying Degrees

Table 6.2 displays statistical characteristics from the sets of trajectories describing 2.0m/s rapid turns at varying degrees. The characteristics relevant to 45° turns can be found in Table 6.1 in the 2.0m/s column.

A level trend was observed when comparing the average duration of contact to the average trajectory duration, ranging between 31.00% and 41.15%. In addition, a level trend was observed when comparing the average duration of slip with the average duration of contact, varying between between 97.75% and 100.0%. However, the average trajectory duration increased proportionally to the degree of the turn: 331.67ms at 22.5°, 353.46ms at 30°, 390.20ms at 45°, 484.77ms at 60°, and 566.43ms at 90°.

Table 6.2: Statistical characteristics of turns conducted to varying turn angles. These characteristics were developed using a set of 5 trajectories per turn angle investigated.

Turn angle [°]	22.5	30	60	90
Mean trajectory duration [ms]	331.67	353.46	484.77	566.43
Variance in trajectory duration [ms]	3.55	1.86	3.14	5.76
Mean air time [ms]	195.20	220.88	334.46	341.82
Variance air time [ms]	0.59	0.83	3.22	1.27
Mean contact time [ms]	136.47	132.58	150.31	224.61
Variance contact time [ms]	1.64	1.79	0.92	3.16
Mean slip time [ms]	133.39	129.39	150.12	224.61

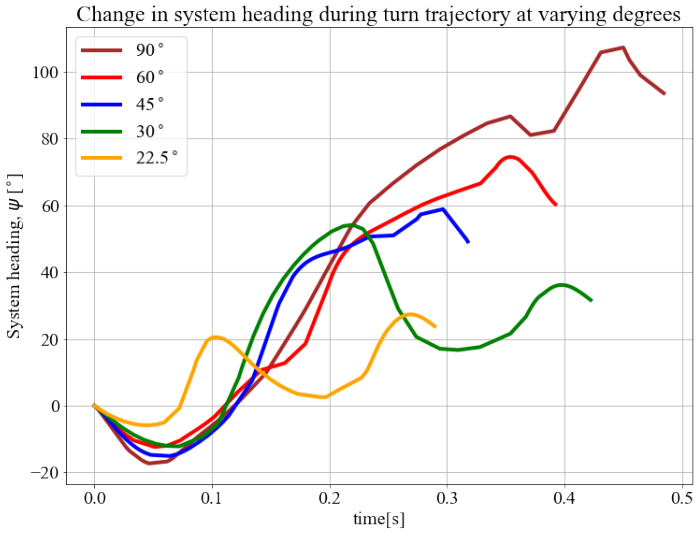

Figure 6.5: This image displays optimal trajectories of the change in heading angle of the robot conducting rapid turns at varying degrees.

Figure 6.5 displays the change in system heading, ψ_{body}, of the set of optimal trajectories describing the robot turning to varying degrees at 2.0m/s. A flat trend was observed in

Stellenbosch University https://scholar.sun.ac.za

the overshoot present, ranging between 16.23°, and 24.65°.

6.3.3. Turning The Other Direction

To display that the optimization was capable of generating turn trajectories towards the inside leg, the left, a set of optimal trajectories are presented. Figure 6.6 displays the change in system heading, ψ_{Turn} while conducting turns of varying degrees, towards the inside leg, at 2.0m/s. Overshoot is present towards the end of the trajectory. Similarly, all trajectories display significant amounts of initial undershoot, ranging from 36.23° to 39.76° for all trajectories.

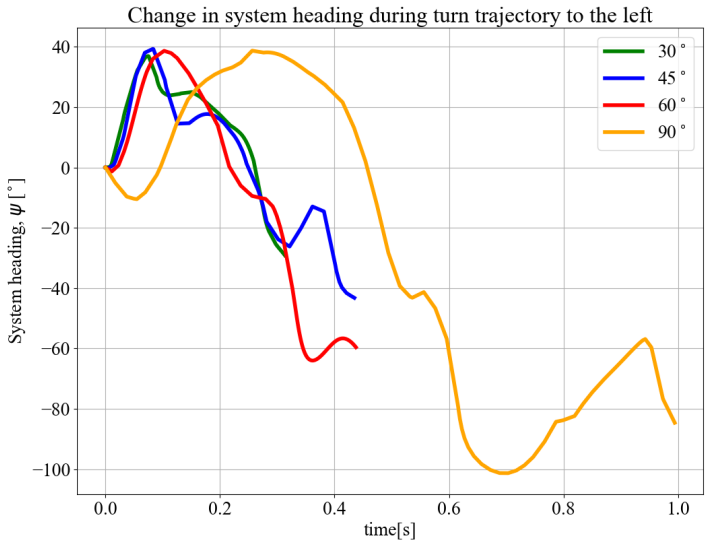

Figure 6.6: This image displays optimal trajectories of the change in heading angle of the robot conducting rapid turns towards the inside leg, the left.

6.4. Discussion

This chapter aimed to determine the significance of slip while conducting rapid turns. Significant amounts of slip during rapid turn trajectories presented were documented in Table 6.1, and Table 6.2. At least 93.32% of the contact duration included slip events while conducting 45° turns at multiple speeds. Similarly, 97.52% of the contact duration included slip events while turning at 2m/s to all turn angles investigated. These results conclude that slip plays a significant role in conducting rapid turn trajectories.

The significance of slip highlights the need for accurate methods of modeling slip and its effects. Trajectories presented in this chapter modeled the friction cone using the

Stellenbosch University https://scholar.sun.ac.za

novel method presented in Chapter 4, and solved for the MPCCs within a tolerance of $\epsilon = 1E - 4$. This ensured that the amount of friction needed to initiate slipping was not underestimated [57].

Figure 6.4, and Figure 6.5, provide evidence of turn overshoot for all optimal results displayed. However, it is noted that for rapid turns conducted at 2.0m/s with varying turn angles, the overshoot is approximately the same magnitude, ranging between 5.26° and 14.12°. Whereas, the overshoot increased proportionally to the speed when conducting 45° degree turns at multiple speeds. Similarly, the magnitude of the initial undershoot for all turns was seen to be proportional to the speed of the turn. This is validated by a comment made by Perkins et. al. [5], that the overshoot is proportional to the speed of the turn, and not the degree of the turn.

Additionally, these rapid turn trajectories were set to start, and end, in the apex pose of of a steady-state gait. Therefore, all turn trajectories could be stitched onto the respective steady-state trajectories presented in Chapter 5. Consequently, the rapid-turn trajectories could be included in a long-time-horizon trajectory. Figure 6.7, displays the speed, and system heading, profile of the a 2m/s long-time-horizon trajectory including a 45° turn off the sagittal plane, confirming the profile hypothesized in Figure 6.3.

The turn started 0.86s into the trajectory, after the acceleration, and two steady-state gaits. The system heading was offset by 45° during the turn phase. Finally, the trajectory ended at rest after two steady-state gaits, and a deceleration trajectory. It is encouraging to note that robot did not have to reduce its speed significantly in conducting the rapid turn. The speed was seen to fluctuate between 1.72m/s, and 2.7m/s.

Stellenbosch University https://scholar.sun.ac.za

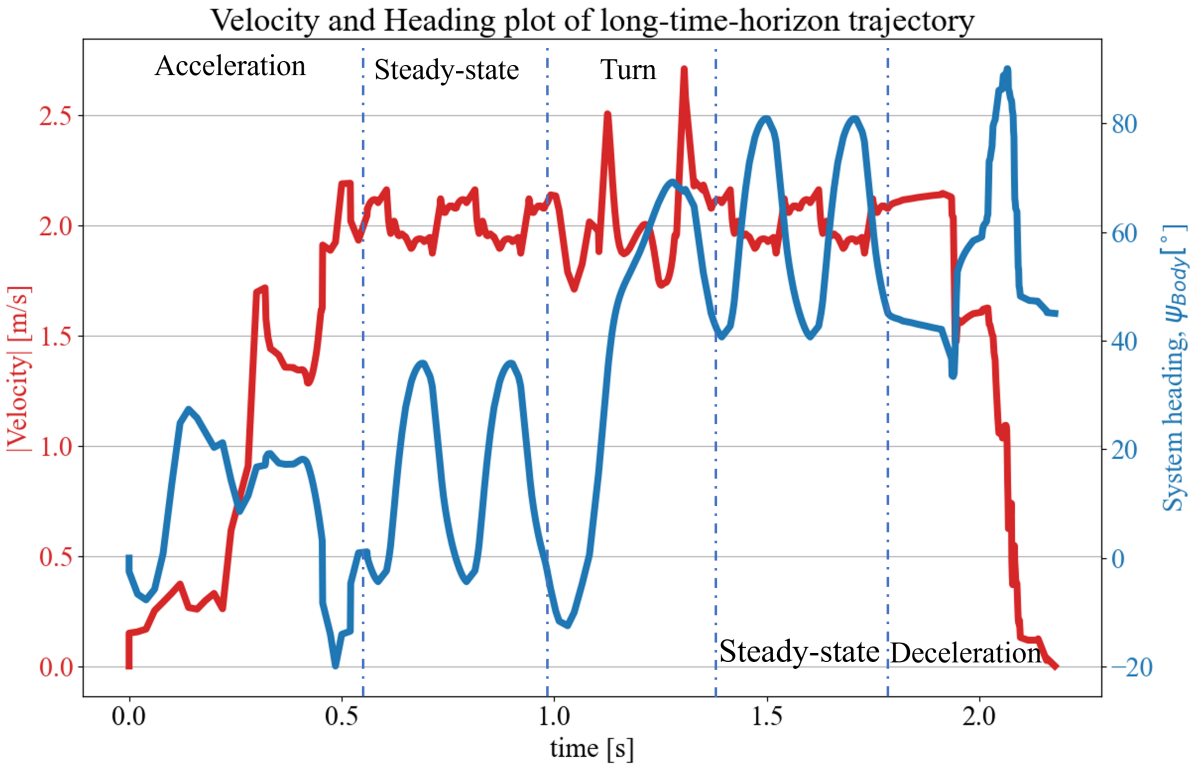

Figure 6.7: This image displays the velocity, and system heading, profile of a 2m/s long-time-horizon trajectory including a 45° rapid turn.

Stellenbosch University https://scholar.sun.ac.za

Chapter 7

Summary, Conclusion and Future Work

This thesis contributed towards legged robotic literature by posing the following 3 questions in Chapter 1, and answering them throughout the thesis document:

1. Is there a better way of modeling the effects of friction in MPCC environments? Chapter 4 adequately answered this question.
2. How to realize dynamic bipedal motion? This was investigated in Chapter 5.
3. How do bipedal robots conduct rapid turns? This was investigated in Chapter 6.

7.1. Summary and Conclusion

These questions arose when perusing relevant robotics literature, presented in Chapter 2. Here, a survey of relevant robotics literature was provided and the theory necessary to understand the research was described.

It was noticed that the bulk of legged robotics literature made use of limiting assumptions to generate periodic steady-state gaits. These assumptions include neglecting the effects of friction, massless legs, and reduced order dynamics inspired by the periodicity of steady-state motions [4–6]. All of which made it possible to generate stable gaits at speed. However, these assumptions were only consistent for studying periodic gaits and were not valid for transient motions [1, 8, 26]. Recent work in contact-implicit trajectory optimization models rigid body contact dynamics without having to specify a contact order. This has been a catalyst for studies into transient legged locomotion. However, much of the contact-implicit optimization research has been limited to planar studies [9–12, 64, 75].

In the literature, it was noted that non-planar implementations of contact-implicit optimization made use of the four-sided polyhedral approximations of the isotropic friction cone. This method is notorious for being computationally intractable, and under-approximates

Stellenbosch University https://scholar.sun.ac.za

the friction forces when the direction of velocity at contact lies between the edges defining the polyhedral [6, 11, 13, 64, 71]. It also inspired the first objective of this thesis.

Chapter 4 aimed to address this limitation, by presenting a novel method of modeling the isotropic friction cone using MPCCs [57]. This novel was compared to the traditional four-faced polyhedral approximation of the friction cone. Here, contact-implicit trajectory optimization problems of a monopedal robot implementing each method of modeling the friction cone were conducted. Additionally, the direction of motion was constrained to expose underestimation of the friction pyramid. These optimizations were conducted under slippery conditions, where $\mu = 0.2$, and non-slippery (sticky) conditions where $\mu = 1.0$.

Results from these experiments confirmed the underestimation of the friction pyramid: the friction pyramid produced trajectories which always slipped. It was shown that the novel method of modeling the friction cone satisfied Coulomb's Law, while providing more accurate, and computationally tractable solutions to non-planar contact implicit trajectory optimization methods.

Further investigations were conducted into the necessary accuracy when implementing ϵ-relaxation schemes to solve the MPCCs in contact implicit trajectory optimizations. It was shown that the slack variables making up the MPCCs during slip events converged when $\epsilon \leq 0.01$.

Therefore, studies conducted in Chapter 4 concluded that there is a better way of modeling the effects of friction using MPCCs. Results from this chapter were published in [57]. This novel method of modeling friction was used to answer the 2 remaining unanswered questions in the objectives.

Next, the second objective question was tackled to realize dynamic bipedal locomotion in Chapter 5. Here, contact implicit trajectory optimization methods were used to model the long-time-horizon trajectories of a non-planar bipedal robot at different velocities. Fisher et. al. [1] suggested that complex long-time-horizon trajectories could be split into smaller, more specific tasks to be solved separately, and later stitched together.

First, Chapter 5 presented steady-state running gaits at speeds ranging from 0.5m/s, to 4.0m/s. Due to its periodic nature the steady-state trajectories were constrained to a run, with contact allowed (not forced) over a specified range of discrete elements. Thereafter, acceleration and deceleration trajectories were generated towards the apex of the steady-state gaits robot accelerating from, and decelerating too, a rest position. No contact constraints were implemented on the rest of the tasks making up dynamic bipedal locomotion. Here, contact-implicit trajectory optimization methods were used to give the optimizer freedom to choose optimal gaits while satisfying Coulomb's Law by allowing the

Stellenbosch University https://scholar.sun.ac.za

contact foot to slip.

Hubicki et. al. [26] first noted the sliding mass velocity profile emerge when studying long-time-horizon trajectories of monopod robots, and hypothesized it holding for more complex models. This allows the forward velocity profile of complex legged robots to be approximated using a 1 DOF sliding mass template. Thereafter, Fisher et. al. [1] confirmed this hypothesis by presenting sliding mass templates on long-time-horizon trajectories of planar bipedal, and quadrupedal, robots. Long-time-horizon trajectories of the robot running along the x-axis were generated by stitching the resultant acceleration, steady-state, and deceleration trajectories together. Research presented in Chapter 5 contributes to this hypothesis by noting a correlation between the forward velocity profile of a sliding mass and the long-time-horizon trajectory of a non-planar bipedal platform with splayed hips.

Dynamic bipedal locomotion was achieved in the long-time-horizon trajectory. This displayed that the presented robot could accelerate from rest to a desired speed, maintain that speed, and then decelerate back to a rest position. Thereby answering the second question posed in the objectives by generating a set of dynamic bipedal trajectories.

Chapter 6 concluded by answering the third question posed in the set of objectives by investigating how bipedal robots conduct rapid turns off the sagittal plane. These rapid turn trajectories were set to start at the apex of the steady-state gait, and constrained to end in the same pose offset by the desired turn angle. It was noticed that slip occured for most of the contact periods for all the rapid turn. On average slip occured 93.32% of the total contact time, indicating the significant role slip plays in rapid motions. The prevalence of slip during these rapid motions further motivated the need of accurate friction modeling presented in Chapter 4. Additionally, Chapter 6 commented on kinematic trends noticed during rapid turns, and presented turns towards both the inside, and outside leg. It was seen that turn overshoot was present for all rapid turn trajectories in this research. This overshoot was proportional to the speed of the turn, and not the degree of the turn, as hypothesized by Perkins et. al. [5].

It is encouraging to note that all complex dynamic trajectories presented in this thesis were initialized using randomized seeds, as described in Chapter 3. This allowed the optimizer to comprehensively search the solution space to find feasible, and non-intuitive solutions to complex transient problems.

Stellenbosch University https://scholar.sun.ac.za

7.2. Future Work

Knowledge gained from this thesis contributed to literature relating to dynamic legged locomotion in 3D. However, this field remains ripe with opportunities for further research.

Contact implicit trajectory optimization methods are notorious for being computationally complex [10]. Consequently, trajectories presented in this thesis were generated using large and intractable optimization problems. Therefore, further research would be to investigate methods of reducing the time needed to find solutions to these optimization problems without limiting non-intuitive gaits for transient motions. Here, the IP-OPT solver was used, with the default configuration. Investigations into using alternative solvers, or solver configurations, with the aim of reducing the time needed to find optimal trajectories could be conducted.

Further investigations could also be conducted into methods of formulating the optimization problem to reduce the computation time. Knemeyer et. al. [14], noted reductions in computation complexity, and time, when modeling the joints of multi-bodied robots using absolute coordinates instead of relative coordinates. A similar investigation could be conducted into different methods of modeling the 3D dynamics in trajectory optimization environments. In this thesis, 3D dynamics were modeled using Euler Angles, as described in Chapter 3. An investigation into the computational complexity of describing 3D robotic systems using Euler Angles could be compared with an implementation modeled using Quaternions [80].

Knowledge gained from this thesis highlights how important it is for roboticists to comprehensively understand the effects of contact, and friction. Friction was seen to play a significant role in the dynamics of the transient motions investigated in this research. Here, contact was modeled on a surface with a uniformed coefficient of friction. This resulted in a isotropic friction cone. Further investigations could be conducted into studying the effects of friction on surfaces with a varying coefficient of friction, resulting in an an-isotropic friction cone [70]. Additionally, investigations could be conducted studying the effects of changing between static and kinetic friction during slip events [63].

Robots modeled in this thesis modeled each foot as a single point contact. Animals are seen using a set of claws and to negotiate the effects of friction [61]. Additionally, shoes aid human locomotion by increasing the surface area of contact, and traction. Therefore, future research involves investigating the effects of friction, and slip across multiple contact points per foot to increase the surface area of contact per foot.

Stellenbosch University https://scholar.sun.ac.za

Bibliography

[1] C. Fisher, C. Hubicki, and A. Patel, "Do intermediate gaits matter when rapidly accelerating?" *IEEE Robotics and Automation Letters*, vol. 4, no. 4, pp. 3418–3424, 2019.

[2] R. M. Alexander, *Optima for animals*. Princeton University Press, 1996.

[3] ——, *Principles of animal locomotion*. Princeton University Press, 2013.

[4] C. M. Hubicki, "From running birds to walking robots: optimization as a unifying framework for dynamic bipedal locomotion," 2014.

[5] A. D. Perkins, *Control of dynamic maneuvers for bipedal robots*. Stanford University, 2010.

[6] P. M. Wensing and D. E. Orin, "Control of humanoid hopping based on a slip model," in *Advances in Mechanisms, Robotics and Design Education and Research*. Springer, 2013, pp. 265–274.

[7] P. M. Wensing, *Optimization and control of dynamic humanoid running and jumping*. The Ohio State University, 2014.

[8] C. Fisher, "Trajectory optimisation inspired design for legged robotics," 2021.

[9] A. Patel, S. L. Shield, S. Kazi, A. M. Johnson, and L. T. Biegler, "Contact-implicit trajectory optimization using orthogonal collocation," *IEEE Robotics and Automation Letters*, vol. 4, no. 2, pp. 2242–2249, 2019.

[10] M. Posa, C. Cantu, and R. Tedrake, "A direct method for trajectory optimization of rigid bodies through contact," *The International Journal of Robotics Research*, vol. 33, no. 1, pp. 69–81, 2014.

[11] D. Stewart and J. C. Trinkle, "An implicit time-stepping scheme for rigid body dynamics with coulomb friction," in *Proceedings 2000 ICRA. Millennium Conference. IEEE International Conference on Robotics and Automation. Symposia Proceedings (Cat. No. 00CH37065)*, vol. 1. IEEE, 2000, pp. 162–169.

[12] Z. Manchester and S. Kuindersma, "Variational contact-implicit trajectory optimization," in *Robotics Research*. Springer, 2020, pp. 985–1000.

Stellenbosch University https://scholar.sun.ac.za

[13] A. Bowling, "Impact forces and agility in legged robot locomotion," *Journal of Vibration and Control*, vol. 17, no. 3, pp. 335–346, 2011.

[14] A. Knemeyer, S. Shield, and A. Patel, "Minor change, major gains: The effect of orientation formulation on solving time for multi-body trajectory optimization," *IEEE Robotics and Automation Letters*, vol. 5, no. 4, pp. 5331–5338, 2020.

[15] A. Patel, "Understanding the motions of the cheetah tail using robotics," 2015.

[16] P. W. Webb, "Maneuverability-general issues," *IEEE Journal of Oceanic Engiineering*, vol. 29, no. 3, 2004.

[17] D. L. Jindrich and M. Qiao, "Maneuvers during legged locomotion," *Chaos: An Interdisciplinary Journal of Nonlinear Science*, vol. 19, no. 2, p. 026105, 2009.

[18] "Locomotor primitives in newborn babies and their development," *Science*, vol. 334, no. 6058, pp. 997–999, 2011.

[19] M. H. Raibert, *Legged robots that balance*. MIT press, 1986.

[20] J. K. Hodgins and M. H. Raibert, "Biped gymnastics," *The International Journal of Robotics Research*, vol. 9, no. 2, pp. 115–128, 1990.

[21] R. R. Playter and M. H. Raibert, "Control of a biped somersault in 3d," in *Proceedings of the IEEE/RSJ international conference on intelligent robots and systems*, vol. 1. IEEE, 1992, pp. 582–589.

[22] N. Banerjee, X. Long, R. Du, F. Polido, S. Feng, C. G. Atkeson, M. Gennert, and T. Padir, "Human-supervised control of the atlas humanoid robot for traversing doors," in *2015 IEEE-RAS 15th International Conference on Humanoid Robots (Humanoids)*. IEEE, 2015, pp. 722–729.

[23] B. Dynamics. Do you love me? [Online]. Available: https://www.youtube.com/watch?v=fn3KWM1kuAw&t=3s&ab_channel=BostonDynamics

[24] ——. Atlas — partners in parkour. [Online]. Available: https://www.youtube.com/watch?v=tF4DML7FIWk&ab_channel=BostonDynamics

[25] J. Read, "10 animals that can walk minutes after they're born," *Downloaded in October*, 2021. [Online]. Available: https://www.rd.com/list/animals-walk-minutes-after-born/

[26] C. Hubicki, M. Jones, M. Daley, and J. Hurst, "Do limit cycles matter in the long run? stable orbits and sliding-mass dynamics emerge in task-optimal locomotion," in *2015 IEEE International Conference on Robotics and Automation (ICRA)*. IEEE, 2015, pp. 5113–5120.

Stellenbosch University https://scholar.sun.ac.za

[27] C. Hubicki, J. Grimes, M. Jones, D. Renjewski, A. Spröwitz, A. Abate, and J. Hurst, "Atrias: Design and validation of a tether-free 3d-capable spring-mass bipedal robot," *The International Journal of Robotics Research*, vol. 35, no. 12, pp. 1497–1521, 2016.

[28] M. Hutter, C. Gehring, D. Jud, A. Lauber, C. D. Bellicoso, V. Tsounis, J. Hwangbo, K. Bodie, P. Fankhauser, M. Bloesch *et al.*, "Anymal-a highly mobile and dynamic quadrupedal robot," in *2016 IEEE/RSJ international conference on intelligent robots and systems (IROS)*. IEEE, 2016, pp. 38–44.

[29] G. Bledt, M. J. Powell, B. Katz, J. Di Carlo, P. M. Wensing, and S. Kim, "Mit cheetah 3: Design and control of a robust, dynamic quadruped robot," in *2018 IEEE/RSJ International Conference on Intelligent Robots and Systems (IROS)*. IEEE, 2018, pp. 2245–2252.

[30] M. Raibert, K. Blankespoor, G. Nelson, and R. Playter, "Bigdog, the rough-terrain quadruped robot," *IFAC Proceedings Volumes*, vol. 41, no. 2, pp. 10 822–10 825, 2008.

[31] D. F. Hoyt and C. R. Taylor, "Gait and the energetics of locomotion in horses," *Nature*, vol. 292, no. 5820, pp. 239–240, 1981.

[32] R. Margaria, *Biomechanics and energetics of muscular exercise*. Oxford University Press, 1976.

[33] P. Wirtz and G. Ries, "The pace of life-reanalysed: why does walking speed of pedestrians correlate with city size?" *Behaviour*, vol. 123, no. 1-2, pp. 77–83, 1992.

[34] G. H. Liu, M. Z. Chen, and Y. Chen, "When joggers meet robots: the past, present, and future of research on humanoid robots," *Bio-Design and Manufacturing*, vol. 2, no. 2, pp. 108–118, 2019.

[35] E. B. Lohman III, K. S. B. Sackiriyas, and R. W. Swen, "A comparison of the spatiotemporal parameters, kinematics, and biomechanics between shod, unshod, and minimally supported running as compared to walking," *Physical Therapy in Sport*, vol. 12, no. 4, pp. 151–163, 2011.

[36] J. Di Carlo, P. M. Wensing, B. Katz, G. Bledt, and S. Kim, "Dynamic locomotion in the mit cheetah 3 through convex model-predictive control," in *2018 IEEE/RSJ international conference on intelligent robots and systems (IROS)*. IEEE, 2018, pp. 1–9.

[37] Y. Gong, R. Hartley, X. Da, A. Hereid, O. Harib, J.-K. Huang, and J. Grizzle, "Feedback control of a cassie bipedal robot: Walking, standing, and riding a segway," in *2019 American Control Conference (ACC)*. IEEE, 2019, pp. 4559–4566.

Stellenbosch University https://scholar.sun.ac.za

[38] G. Garofalo, C. Ott, and A. Albu-Schäffer, "Walking control of fully actuated robots based on the bipedal slip model," in *2012 IEEE International Conference on Robotics and Automation*, 2012, pp. 1456–1463.

[39] J. Park, J. Lee, J. Lee, K.-S. Kim, and S. Kim, "Raptor: Fast bipedal running and active tail stabilization," in *2014 11th International Conference on Ubiquitous Robots and Ambient Intelligence (URAI)*. IEEE, 2014, pp. 215–215.

[40] J. Degrave, M. Burm, T. Waegeman, F. Wyffels, and B. Schrauwen, "Comparing trotting and turning strategies on the quadrupedal oncilla robot," in *2013 IEEE International Conference on Robotics and Biomimetics (ROBIO)*. IEEE, 2013, pp. 228–233.

[41] K. C. Galloway, G. C. Haynes, B. D. Ilhan, A. M. Johnson, R. Knopf, G. A. Lynch, B. N. Plotnick, M. White, and D. E. Koditschek, "X-rhex: A highly mobile hexapedal robot for sensorimotor tasks," 201you0.

[42] M. L. KAIST. Kaist raptor robot runs at 46 km/h, active tail stabilization. [Online]. Available: https://www.youtube.com/watch?v=lPEg83vF_Tw&ab_channel=MSCLab.KAISTd

[43] B. Dynamics. Cheetah robot runs 28.3 mph; a bit faster than usain bolt. [Online]. Available: https://www.youtube.com/watch?v=chPanW0QWhA&ab_channel=BostonDynamics

[44] R. Nayeem, S. Bazzi, N. Hogan, and D. Sternad, "Transient behavior and predictability in manipulating complex objects," in *2020 IEEE International Conference on Robotics and Automation (ICRA)*. IEEE, 2020, pp. 10 155–10 161.

[45] A. M. Wilson, J. Lowe, K. Roskilly, P. E. Hudson, K. Golabek, and J. McNutt, "Locomotion dynamics of hunting in wild cheetahs," *Nature*, vol. 498, no. 7453, pp. 185–189, 2013.

[46] N. Sharp, "Timed running speed of a cheetah (acinonyx jubatus)," *Journal of Zoology*, vol. 241, no. 3, pp. 493–494, 1997.

[47] S. B. Williams, H. Tan, J. R. Usherwood, and A. M. Wilson, "Pitch then power: limitations to acceleration in quadrupeds," *Biology letters*, vol. 5, no. 5, pp. 610–613, 2009.

[48] M. Haberland and S. Kim, "On extracting design principles from biology: Ii. case study—the effect of knee direction on bipedal robot running efficiency," *Bioinspiration & biomimetics*, vol. 10, no. 1, p. 016011, 2015.

Stellenbosch University https://scholar.sun.ac.za

[49] ——, "On extracting design principles from biology: I. method–general answers to high-level design questions for bioinspired robots," *Bioinspiration & biomimetics*, vol. 10, no. 1, p. 016010, 2015.

[50] R. M. Walter and D. R. Carrier, "Effects of fore–aft body mass distribution on acceleration in dogs," *Journal of Experimental Biology*, vol. 214, no. 10, pp. 1763–1772, 2011.

[51] ——, "Rapid acceleration in dogs: ground forces and body posture dynamics," *Journal of Experimental Biology*, vol. 212, no. 12, pp. 1930–1939, 2009.

[52] S. Williams, J. Usherwood, K. Jespers, A. Channon, and A. Wilson, "Exploring the mechanical basis for acceleration: pelvic limb locomotor function during accelerations in racing greyhounds (canis familiaris)," *Journal of Experimental Biology*, vol. 212, no. 4, pp. 550–565, 2009.

[53] C. A. Moreno, *Biomechanics of non-steady locomotion: Bone loading, turning mechanics and maneuvering performance in goats*. Harvard University, 2010.

[54] H. Tan and A. M. Wilson, "Grip and limb force limits to turning performance in competition horses," *Proceedings of the Royal Society B: Biological Sciences*, vol. 278, no. 1715, pp. 2105–2111, 2011.

[55] D. L. Jindrich, N. C. Smith, K. Jespers, and A. M. Wilson, "Mechanics of cutting maneuvers by ostriches (struthio camelus)," *Journal of Experimental Biology*, vol. 210, no. 8, pp. 1378–1390, 2007.

[56] S. Shield and A. Patel, "Waste not, want not: Lessons in rapid quadrupedal gait termination from thousands of suboptimal solutions," in *2020 IEEE/RSJ International Conference on Intelligent Robots and Systems (IROS)*. IEEE, 2020, pp. 4012–4019.

[57] D. Pretorius and C. Fisher, "A novel method for computing the 3d friction cone using complimentary constraints," in *2021 IEEE International Conference on Robotics and Automation (ICRA)*. IEEE, 2021, pp. 5000–5006.

[58] S. Shigemi, A. Goswami, and P. Vadakkepat, "Asimo and humanoid robot research at honda," *Humanoid robotics: A reference*, pp. 55–90, 2019.

[59] K. Miura, F. Kanehiro, K. Kaneko, S. Kajita, and K. Yokoi, "Quick slip-turn of hrp-4c on its toes," in *2012 IEEE International Conference on Robotics and Automation*. IEEE, 2012, pp. 3527–3528.

[60] T. Ishida, Y. Kuroki, and J. Yamaguchi, "Mechanical system of a small biped entertainment robot," in *Proceedings 2003 IEEE/RSJ International Conference on*

Stellenbosch University https://scholar.sun.ac.za

Intelligent Robots and Systems (IROS 2003)(Cat. No. 03CH37453), vol. 2. IEEE, 2003, pp. 1129–1134.

[61] A. Patel and M. Braae, "Rapid turning at high-speed: Inspirations from the cheetah's tail," in *2013 IEEE/RSJ International Conference on Intelligent Robots and Systems*. IEEE, 2013, pp. 5506–5511.

[62] B. E. Unplugged. Cheetah vs greyhound, world's fastest dog in super slow motion. BBC Earth Unplugged. [Online]. Available: https://www.youtube.com/watch?v=jc8Hno4M0Qs&ab_channel=BBCEarthUnplugged

[63] S. Goyal, "Planar sliding of a rigid body with dry friction: limit surfaces and dynamics of motion," Ph.D. dissertation, Cornell University Ithaca, New York, USA, 1989.

[64] D. E. Stewart, "Rigid-body dynamics with friction and impact," *SIAM review*, vol. 42, no. 1, pp. 3–39, 2000.

[65] R. Tedrake, "Underactuated robotics: Algorithms for walking, running, swimming, flying, and manipulation (course notes for mit 6.832)," *Downloaded in May*, 2020. [Online]. Available: http://underactuated.mit.edu/

[66] N. Ratliff, "Controlling floating-based robots."

[67] C. A. Coulomb, *Th 'e orie simple machines by keeping é the friction of their parts and 'a the stiffness of the ropes*. Bachelor, 1821.

[68] D. Dowson, "Tmbology from leonardo to the tmrd millenium;-millimetres to nanometres," *Sarton Chair of the History of Sciences University of Ghent, Belgium*, p. 253.

[69] J. Gao, W. Luedtke, D. Gourdon, M. Ruths, J. Israelachvili, and U. Landman, "Frictional forces and amontons' law: from the molecular to the macroscopic scale," 2004.

[70] S. Walker and R. Leine, "Set-valued anisotropic dry friction laws: formulation, experimental verification and instability phenomenon," *Nonlinear Dynamics*, vol. 96, no. 2, pp. 885–920, 2019.

[71] S. Kuindersma, R. Deits, M. Fallon, A. Valenzuela, H. Dai, F. Permenter, T. Koolen, P. Marion, and R. Tedrake, "Optimization-based locomotion planning, estimation, and control design for the atlas humanoid robot," *Autonomous robots*, vol. 40, no. 3, pp. 429–455, 2016.

[72] M. Kelly, "An introduction to trajectory optimization: How to do your own direct collocation," *SIAM Review*, vol. 59, no. 4, pp. 849–904, 2017.

Stellenbosch University https://scholar.sun.ac.za

[73] C. R. Hargraves and S. W. Paris, "Direct trajectory optimization using nonlinear programming and collocation," *Journal of guidance, control, and dynamics*, vol. 10, no. 4, pp. 338–342, 1987.

[74] P. M. Wensing and D. E. Orin, "3d-slip steering for high-speed humanoid turns," in *2014 IEEE/RSJ International Conference on Intelligent Robots and Systems*, 2014, pp. 4008–4013.

[75] M. M. A. Posa, "Optimization for control and planning of multi-contact dynamic motion," Ph.D. dissertation, Massachusetts Institute of Technology, 2017.

[76] S. M. Safdarnejad, J. D. Hedengren, N. R. Lewis, and E. L. Haseltine, "Initialization strategies for optimization of dynamic systems," *Computers & Chemical Engineering*, vol. 78, pp. 39–50, 2015.

[77] D. Ralph* and S. J. Wright, "Some properties of regularization and penalization schemes for mpecs," *Optimization Methods and Software*, vol. 19, no. 5, pp. 527–556, 2004.

[78] R. Fletcher* and S. Leyffer, "Solving mathematical programs with complementarity constraints as nonlinear programs," *Optimization Methods and Software*, vol. 19, no. 1, pp. 15–40, 2004.

[79] J. Diebel, "Representing attitude: Euler angles, unit quaternions, and rotation vectors," *Matrix*, vol. 58, no. 15-16, pp. 1–35, 2006.

[80] C. Fisher, "State estimation of a cheetah spine and tail using an inertial sensor network," Master's thesis, University of Cape Town, 2015.

[81] A. Meurer, C. P. Smith, M. Paprocki, O. Čertík, S. B. Kirpichev, M. Rocklin, A. Kumar, S. Ivanov, J. K. Moore, S. Singh, T. Rathnayake, S. Vig, B. E. Granger, R. P. Muller, F. Bonazzi, H. Gupta, S. Vats, F. Johansson, F. Pedregosa, M. J. Curry, A. R. Terrel, v. Roučka, A. Saboo, I. Fernando, S. Kulal, R. Cimrman, and A. Scopatz, "Sympy: symbolic computing in python," *PeerJ Computer Science*, vol. 3, p. e103, Jan. 2017. [Online]. Available: https://doi.org/10.7717/peerj-cs.103

[82] W. E. Hart, J.-P. Watson, and D. L. Woodruff, "Pyomo: modeling and solving mathematical programs in python," *Mathematical Programming Computation*, vol. 3, no. 3, pp. 219–260, 2011.

[83] W. E. Hart, C. D. Laird, J.-P. Watson, D. L. Woodruff, G. A. Hackebeil, B. L. Nicholson, and J. D. Siirola, *Pyomo–optimization modeling in python*, 2nd ed. Springer Science & Business Media, 2017, vol. 67.

Stellenbosch University https://scholar.sun.ac.za

[84] G. Van Rossum and F. L. Drake, *Python 3 Reference Manual*. Scotts Valley, CA: CreateSpace, 2009.

[85] A. Wächter and L. T. Biegler, "On the implementation of an interior-point filter line-search algorithm for large-scale nonlinear programming," *Mathematical programming*, vol. 106, no. 1, pp. 25–57, 2006.

[86] L. T. Biegler, *Nonlinear programming: concepts, algorithms, and applications to chemical processes*. SIAM, 2010.

[87] B. Baumrucker and L. Biegler, "Mpec strategies for optimization of a class of hybrid dynamic systems," *Journal of Process Control*, vol. 19, no. 8, pp. 1248–1256, 2009.

[88] T-Motor, "Ak10," *Downloaded in October 2021*, 2021. [Online]. Available: https://store.tmotor.com/goods.php?id=1030

[89] T. Hoheisel, C. Kanzow, and A. Schwartz, "Theoretical and numerical comparison of relaxation methods for mathematical programs with complementarity constraints," *Mathematical Programming*, vol. 137, no. 1-2, pp. 257–288, 2013.

[90] W. Chen and L. T. Biegler, "Nested direct transcription optimization for singular optimal control problems," *AIChE Journal*, vol. 62, no. 10, pp. 3611–3627, 2016.

[91] "Ipopt documentation," https://coin-or.github.io/Ipopt/, accessed: October 2021.

[92] N. S. Pollard and P. S. Reitsma, "Animation of humanlike characters: Dynamic motion filtering with a physically plausible contact model," in *Yale workshop on adaptive and learning systems*, vol. 2. New Haven, CT, USA, 2001.

[93] S. Pabst, B. Thomaszewski, and W. Strasser, "Anisotropic friction for deformable surfaces and solids," in *Proceedings of the 2009 ACM SIGGRAPH/Eurographics Symposium on Computer Animation*, 2009, pp. 149–154.

[94] D. Pretorius and C. Fisher, "Bipedal turning: To slip or not," *IEEE Robotics and Automation Letters, Under Review*, 2022.